USE OF UNMANNED AERIAL VEHICLES COMPARED TO TERRESTRIAL LASER SCANNING FOR CHARACTERIZING DISCONTINUITIES ON ROCK EXPOSURES

HABTAMU ESHETU GUTA
May, 2017

SUPERVISORS:
Associate Professor, Dr. Robert Hack,
Professor, Dr. Freek Van der Meer

ADVISOR:
Professor, Dr. Norman Kerle

USE OF UNMANNED AERIAL VEHICLES COMPARED TO TERRESTRIAL LASER SCANNING FOR CHARACTERIZING DISCONTINUITIES ON ROCK EXPOSURES

HABTAMU ESHETU GUTA
Enschede, The Netherlands, May, 2017

Thesis submitted to the Faculty of Geo-Information Science and Earth Observation of the University of Twente in partial fulfilment of the requirements for the degree of Master of Science in Geo-information Science and Earth Observation.
Specialization: Applied Earth Sciences- Natural Hazards, Risk, and Engineering

SUPERVISORS:
Associate Prof, Dr. Robert Hack,
Prof, Dr. Freek, Van der Meer

ADVISOR:
Prof, Dr. Norman, Kerle

THESIS ASSESSMENT BOARD:
Prof, Dr. Victor Jetten (Chair)
Dr, Marco Huisman (External Examiner, HMC)

ABSTRACT

Generation of detailed and systematic geo-mechanical information of exposed rock faces and determination and analysis of discontinuity properties in the rock mass is a fundamental part of assessment of rock slope stability because discontinuities govern, to a large extent, the geomechanical behaviour of a rock mass.

Discontinuity properties can be measured or estimated traditionally in the field, in a structured way by using hand held compass and measuring tape. Characterization of rock mass discontinuities by using traditional field techniques such as Scanline and SSPC methods presents several disadvantages. Data derived by traditional field techniques may be erroneous due to human bias, sampling method used, and instrument error and thus generate inaccurate data. As a result, it is often difficult to make spherical statistical calculations and analysis of the discontinuities. Therefore, it is worthwhile to use remote sensing as a complementary or standalone technique for discontinuity characterization of a rock mass.

Remote sensing techniques such as Terrestrial laser scanning (TLS) offer an alternative means of rock mass characterization. Nonetheless, rock mass surveys by TLS may also be constrained by occlusion. Recently, the use of Unmanned Aerial Vehicles (UAVs) as data acquisition platform, and associated image matching advancement has shown a great potential for rock mass characterization and mapping of discontinuities. The use of UAVs do not only overcome the limitations of traditional field surveys, but also serve as data acquisition platform that can acquire large set of measurements with less effort and cost. Therefore, the main objective of the research is to derive, compare and validate rock mass discontinuity geometric properties generated from point cloud data sets using Unmanned Aerial Vehicles (UAVs) equipped with a digital optical camera versus point clouds derived from Terrestrial Laser scanners (TLS) through computer-based segmentation method (based on Hough transformation and Least squares).

In this research discontinuity geometric properties mainly orientation, plane geometry, discontinuity set statistics and equivalent normal set spacing were derived from two point cloud data sets (UAV-based photogrammetry and Terrestrial Laser scanners) via segmentation method based on Hough transformation and Least Squares. The derived geometric properties of discontinuities were compared to discontinuity properties measured by field-based methods (scanline and the SSPC methods). Segmentation of the UAV based point clouds generated the highest number individual discontinuity planes and sets (five sets) including the exposed bedding planes. A quantitative plane by plane comparison in terms of pole-vector difference or dihedral angle between the discontinuity planes derived from the two point cloud segmentation versus selected discontinuity planes showed a small angular differences (5 to 6 degrees), which verifies a reasonable correlation. Furthermore, a comparison between the mean equivalent normal set spacing of corresponding discontinuity sets derived from both UAV-based and TLS point cloud segmentation shows comparable results indicating a good degree of correlation.

Therefore, this research has showed UAV-based point cloud segmentation can generate discontinuity orientations within a comparable accuracy to both the TLS point cloud segmentation and the SSPC methods. Thus, the use of UAVs can offer a reasonable alternative to both the conventional and TLS methods for rock mass discontinuity characterization.

ACKNOWLEDGEMENTS

Most of all, I would like to express my deepest and warmest gratitude to almighty God and my Lord Jesus Christ for helping and sustaining me complete my study successfully.
I would like to express my gratitude to Kingdom of the Netherlands for granting me the opportunity to pursue my Masters study through the Netherlands Fellowship Programme (NFP). I am also indebted to the Geological Survey of Ethiopia, especially Mr. Hunde Melka, for offering me the necessary support and nomination to study abroad.
I am indebted to my supervisors Dr. Robert Hack, Professor Vander Meer (Freek), and Prof Dr. Norman Kerle for valuable feedback and guidance. I am very grateful to Bart Krol for providing me with every necessary support, understanding, and cooperation during my study in ITC particularly during my MSc research.
I am thankful for prof.dr.ir. Vosselman (George) for providing me Point Cloud Mapper software for segmenting point clouds.I am thankful to Dr. Francesco Nex for giving me short training on how to operate Terrestrial Laser Scanning. I am deeply grateful to Dr. Siefko Slob for valuable discussion and suggestions and for providing me the Matlab scripts. I like to also thank Zhang (Zhenchao) for helping me with running Matlab scripts.

My heartfelt gratitude also goes to Mr. Moulder, computer help desk, for offering me with necessary IT assistance whenever called upon. I would like to thank Miranda Bonke for facilitating my study period extension. I would like to thank Tadesse Agafari for his cooperation and contribution towards extending my study period. My heartfelt gratitude also goes to Marie Chantal and Theressa May for the encouragement during my hard times in ITC.

I am indebted to Mr. Sideraus Watse for unconditionally facilitating UAV imagery acquisition and TLS survey in cold winter weather and assistance in the field. I thank Mulat Teshome and Solomon for assisting me with TLS survey in the field. My gratitude also goes to Dr. Mila Koeva, Mrs. Julia Leventi, Dr. Mavrouli (Olga) and Brian Adams.
I would like to thank all members of my family for their relentless inspiration, encouragement, and motivation. You were all my spur to my success.
Last but not least, my heartfelt gratitude goes to my relatives and friends all over the globe, and my master classmates.

TABLE OF CONTENTS

LIST OF FIGURES

LIST OF TABLES

1. INTRODUCTION

1.1. Background

Large excavation works of rock and soil masses (more generally groundmasses) for civil engineering projects and mining activities necessitates comprehensive site investigation and characterization of the stability of geologic slopes prior to and after excavation (Bieniawski, 1989; Pantelidis, 2009). This is because unstable slopes are hazardous to people, property, infrastructure, and environment and may result in large economic losses as well as injuries or fatalities (Hoek & Bray, 1981; Goodman, 1976; Pantelidis, 2009).

Generation of detailed and systematic geo-mechanical information of exposed rock faces and determination and analysis of discontinuity properties in the rock mass is a fundamental part of the assessment of rock slope stability because discontinuities govern, to a large extent, the geomechanical behaviour of a rock mass (Bieniawski, 1989). A rock mass comprises intact rocks plus the system of discontinuities. Discontinuities are planes of weakness in rock masses and they include bedding planes, joints, faults, lineaments, foliations and schistosity and other mechanical defects (Priest, 1993). These discontinuities primarily make the rock masses heterogeneous and anisotropic. Discontinuities render a rock mass weaker as their presence reduces the shear and tensile strengths of the rock mass. The geometric discontinuity properties normally measured in the field include number of sets, orientation, spacing, persistence, roughness, infill material, and features such as solution or karst. Further is established whether the discontinuity is fitting or not, i.e. whether the two sides of the discontinuity have moved before.

Several internationally accepted and well-established standard techniques and methods have been developed over the years for a manual survey of a rock face including International Society for Rock Mechanics (ISRM, 1978), British standard (BS 5930, 1999), standards of the International Standard Organization (ISO 14689-1, 2003). These standards offer methods to establish detailed qualitative and minimum quantitative properties of discontinuities (Slob et al., 2010). Discontinuity properties can be measured or estimated in the field, in a structured way, using hand held compass and measuring tape via scan line mapping (Priest & Hudson, 1981; Priest, 1993), cell mapping and rapid face mapping methods (Hack et al., 2003). The scan line mapping technique comprises measuring discontinuities along a single line. Cell mapping, on the other hand, is two-dimensional discontinuity mapping technique in which a square window on the rock exposure is selected to measure discontinuities that fall within the window. The rapid face mapping technique deals with more general rock mass discontinuity characterization by identifying the major discontinuity sets in a rock mass and measuring their representative orientation and spacing (Hack et al., 2003). In this method, rock mass characterization and classification is generally executed by dividing the rock masses into so-called "geotechnical units". A geotechnical unit is defined as the portion of the rock mass that possess more-or-less similar mass properties and thus a similar mechanical behaviour. The division is normally based on the material characteristics or lithology, degree of and susceptibility to weathering, characteristics of discontinuity sets such as spacing and orientation, etc. Groundwater presence and pressure are also of importance for ground mass behaviour, but as these are local features and normally variable in time these are not included in the geotechnical unit but taken into account in subsequent analyses and calculations.

1.2. Remote sensing techniqeus for rock mass and discontinuity mapping

Nowadays, remote sensing techniques such as Terrestrial laser scanning (TLS), and close-range terrestrial photogrammetry and associated image processing advances are offering an alternative means of rock mass characterization. They can be deployed to inaccessible rock exposure areas and where a rock mass is dangerous to access (Birch, 2006; Slob et al., 2010; Liu, 2013; Gigli et al., 2014). Besides, remote sensing may have an added value as it is less sensitive to human bias, and characterize the groundmass with features not available in traditional visual assessment (Assali, Grussenmeyer, Villemin, Pollet, & Viguier, 2014). Moreover, remote sensing techniques allow increased characterization of the rock mass both in terms of areal extent and volume of data generated, thus full 3D model of the rock exposure can be reconstructed and sufficient data can also be generated that can be utilized for statistical analysis.

1.2.1. Terrestrial remote sensing for rock mass characterization

The use of close range terrestrial digital photogrammetry is growing as a useful and efficient remote sensing technique for ground mass characterization particularly in situations where manual field measurement is impossible or dangerous (Haneberg, 2008; Sturzenegger & Stead, 2009). This technique can serve as safer and faster alternative measuring tool for characterizing steep slopes and open pit quarry areas and generate data comparable to laser-based survey equipment (Nex & Remondino, 2014; Haneberg, 2008). Tannant, (2015) identified main discontinuity sets in a rock face by using a digital terrain model with the use of Structure from Motion (SfM) image processing of two stereo photographs captured during short field survey. Digital photogrammetry and subsequent image processing deliver more advantages than conventional exposure characterization or surveying with terrestrial laser scanners because field work is done rapidly with less cost providing more time for processing, interpretation, and digital mapping (Haneberg, 2008; Nex & Remondino, 2014; Tannant, 2015). However, terrestrial photogrammetry is constrained by difficulty in the determination of best camera position relative to the rock mass exposure when taking photos from the ground. The presence of vegetation in front of a rock face can also limit visibility of the rock face. Moreover, horizontal steps or benches at higher parts of the rock face may also be occluded since images are often captured from the base level of the rock face. These limitations are overcome when photos are captured using Unmanned Aerial Vehicles (UAVs) above ground though it might be difficult to plan perfect flight that eliminates all occlusions on the rock face (Haneberg, 2008; Tannant, 2015).

1.2.2. Terrestrial laser scanning (TLS) for rock mass characterization

Terrestrial laser scanning (TLS) is one the most promising RS techniques for characterizing ground mass exposures as it produces dense point clouds that provide 3D models of exposures (Slob et al., 2005; Sturzenegger & Stead, 2009). It has been increasingly used for ground mass characterization allowing detailed data acquisition in a short time and accurate 3-D representation of the exposures (Slob et al., 2007; Gigli et al., 2014). TLS point clouds consist of 3D coordinates and reflected intensity of exposures in groundmass, hence geometry of exposures can be represented in 3D digital model (Slob et al., 2007). Modern TLS systems allow more than 6km long measurement range and high-speed data acquisition. They are combined with built-in calibrated digital camera that allows 3D actual scene visualization of point clouds including textural and color properties of rock faces (Riegl, n.d.). The use of TLS is more suited to rock mass exposures covered by vegetation since it is less impacted by vegetation cover on the ground mass. In addition, the operational set up of TLS is becoming simpler with the latest models. However, the study of rock exposures by TLS may also be constrained by occlusion (Slob et al., 2007). Another drawback of TLS is a large amount of output data is generated, thus computers with large RAM size are required for fast processing otherwise it may be difficult to handle or process in short period (Kisztner, Jelínek, Daněk, & Růžička, 2016).

1.2.3. Application of Unmanned Aerial Vehicles (UAVs)

Unmanned Aerial Vehicles (UAVs) (also known as drones) were first developed for military use. However, their use for civil applications for data acquisition platform has shown a great potential for geotechnical surveying, geo-hazard investigation, mapping and environmental applications compared to traditional aerial surveys or ground-based photogrammetry (Bemis et al., 2014; Jordan, 2015; Fakunle, 2016). UAVs provide cost effective, flexible, very high spatial and temporal resolution and accurate data acquisition platforms in a quicker and safer manner. Using UAVs vertical and unstable rock faces can be easily surveyed. In addition, it is possible to fly UAVs close to objects under study to acquire highly detailed imageries. UAVs can be operated manually, semi-automated, and in autonomous modes. Moreover, they can be equipped with a digital camera or a multispectral scanner. Bigger and stable UAVs, which have a long endurance, can even carry bigger payloads such as LIDAR sensors or SAR instruments (Nex & Remondino, 2014; rapidlasso, n.d.).

A UAV system comprises the aircraft component, sensor payloads, navigation system, and a ground control station (Colomina & Molina, 2014) as shown in figure 1-1 below. UAVs are categorized based on platform as fixed wing and multi-rotary wing. Fixed wing UAVs are more stable, fly longer and usually used for surveying large areas. Nonetheless, they require a larger free area for takeoff and landing (McEvoy, Hall, & McDonald, 2016). They are preferred for vertical/nadir imaging. On the other hand, multi-rotary wing UAVs can take off and land vertically without the need for a runway. They are flexible allowing multiple configurations of camera orientation. Thus, they are suitable for surveying steep to vertical/sub-vertical rock exposures minimizing or precluding the problem of occlusion (Watts, Ambrosia, & Hinkley, 2012).

Figure 1-1: DJI Phantom 4 quadcopter UAV system (source: http://www.pcadvisor.co.uk/review/drones/dji-phantom-4-review)

The rapid advancement in UAV technology has brought new and improved features in terms of camera lens, propulsion and navigation systems. A UAV yields different quality images for the same size DSLR camera mounted on it depending on payload and camera stability. For instance, bigger size UAVs like Aibot allow low vibration to camera resulting in blur-free photos. Larger size cameras mounted on UAVs deliver more quality photos than smaller cameras (fstoplounge, n.d.). The quality of the camera lens also impacts the quality of the images captured. For instance, lens distortion in Phantom 4, which is a small sized but widely used multi-copter UAV, is reduced by 36% compared to phantom 3 professional, thus improved the quality of images by reducing lens distortion (dji, n.d.). The operation of UAVs in the field can be affected by wind speed during image acquisition. Lack of consistent regulation requirements for operating the UAVs is presenting a barrier for their wider use attributed to safety reasons and security against the misuse of UAVs (Watts et al., 2012).

1.3. Image processing techniques

Images captured by UAV platforms are processed via photogrammetric image processing techniques such as Structure from Motion (SfM) and Patch-Based Multi-view Stereo (PMVS2) algorithms (Westoby, Brasington, Glasser, Hambrey, & Reynolds, 2012). The processing delivers dense point clouds[1]. The point clouds are then reconstructed to generate coloured and textured 3D models such as DSM. By further analyzing and interpreting the point clouds or the derived 3D models, it is possible to generate geotechnical data required to characterize a rock face and perform stability assessment (Mancini et al., 2013; Tannant, 2015; Spreafico, 2015).

1.4. Point cloud analyzing techniques

In general, point cloud analyzing techniques can be divided into two methods, namely surface reconstruction and direct segmentation (Vosselman & Mass, 2010). Both methods can be used to derive rock mass discontinuity properties. In surface reconstruction methods, point clouds are structured via point interpolation that generates surface meshes. The surface meshes can be reconstructed as 2D or 3D. Direct segmentations involves structuring of the point clouds via a tree-structuring procedure ensued by segmentation or classification the points into subsets that belong to the same geometric shape (Rabbani, Van der Hueuvel, & Vosselman, 2006). In the case of discontinuity characterization of a rock mass, the geometric shape is a plane. Evaluation of planarity in the point clouds can be defined by using either a Hough transform (Vosselman, Gorte, Sithole, & Rabbani, 2004), (Total) Least Squares Analysis (Feng, Sjögren, Stephansson, & Jing, 2001), Random Sample Consensus (RANSAC) and Principal Component Analysis (Slob et al., 2005).

In recap, remote sensing techniques such as Terrestrial laser scanning (TLS), and close-range terrestrial photogrammetry offer an alternative means of rock mass characterization. Advances in image processing techniques, state of the art methods of point cloud analysis and computer programs allow faster, detailed and more complete data acquisition and analysis that enable to accurately generate 3-D representation of a rock face. However, there are still limitations associated with each remote sensing method. For instance, terrestrial photogrammetry is constrained by the distance between the camera position and the rock face, the presence of vegetation, etc. On the other hand, rock mass surveys by TLS may also be constrained by occlusion. However, the use of UAVs as data acquisition platform, and associated image matching advancement has shown a great potential for rock mass characterization and mapping of discontinuities.

[1] Point clouds are unorganized and noisy 3-dimentional data generated by laser scanners or photogrammetric image processing techniques.

Their flexibility, cost effectiveness, high spatial and temporal data acquisition ability, etc. makes the UAVs more suitable remote sensing platform for rock mass and discontinuity characterization.

Therefore, this research aims to determine the strength and limitations of using Unmanned Aerial Vehicles (UAVs) equipped with a digital camera, Terrestrial Laser Scanner technique (TLS) and traditional geo-mechanical field survey for characterizing discontinuities in Romberg quarry sandstone rock exposure. The pros and cons of each of the three techniques will be assessed with regard to identifying discontinuity sets, their orientation (dip direction and dip angle), and spacing/frequency. Afterward, the discontinuity data will be organized, statistically analyzed and compared to data generated from a traditional survey. The comparison of RS techniques to a traditional field survey will allow validation of the data generated from RS techniques.

1.5. Problem statement

Characterization of rock mass discontinuities by using traditional field techniques presents several disadvantages. Data derived by traditional field techniques may be erroneous due to human bias, sampling method used, and instrument error and thus generate inaccurate data (Slob et al., 2005; Giovanni Gigli, Morelli, Fornera, & Casagli, 2014). In addition, use of traditional field methods may be constrained by lack of accessibility to the exposure under study (Turner, Kemeny, Slob, & Hack, 2006). Moreover, these techniques produce a limited number of discontinuity data since measurements are often taken on the lower section of a slope and a large portion of exposures is often inaccessible or covered with vegetation, slope deposits, etc. As a result, the use of rock climbing equipment or scaffoldings is required to access the higher parts of a rock face. Consequently, these methods are time-consuming, expensive and labor intensive (Turner et al., 2006). Furthermore, manual field surveys may be hazardous to field geologists since physical contact with exposure is required. Generally, limited data are generated using traditional field techniques, as a result, it is often difficult to make spherical statistical calculations and analysis of the discontinuities. Therefore, it is worthwhile to use remote sensing as a complementary or standalone technique for discontinuity characterization of a rock mass.

The use of TLS and UAV does not only overcome the limitations of traditional field surveys, but also serve as data acquisition platform that can acquire large set of measurements with less effort and cost. Therefore, by using automated point cloud segmentation method (based on Hough transformation and Least squares), this research will attempt to extract sufficient discontinuity data from point clouds that can be used to create a complete model of rock mass discontinuity system/fabric within short period whilst reducing the degree of uncertainty.

1.6. Objectives and research questions

1.6.1. Main objective

The main objective of the research is to derive, compare and validate rock mass discontinuity geometric properties generated from point cloud data sets using Unmanned Aerial Vehicles (UAVs) equipped with a digital optical camera versus point clouds derived from Terrestrial Laser scanners (TLS) through computer-based segmentation method (based on Hough transformation and Least squares). The principal geometric properties this research aims to derive from point cloud datasets include orientation (dip direction and dip angle) of discontinuity planes, their sets, and spacing.
In this regard, the following specific objectives are formulated to address the overall objective.

1.6.2. Specific objectives

- To derive discontinuity planes from UAV and TLS datasets, and cluster them into different sets and derive their respective orientations (dip direction and angle of dip) and spacing.
- To statistically analyze and compare orientations and spacing of discontinuity planes derived from both UAV datasets and TLS datasets.
- To validate orientation and spacing of discontinuity planes derived from point clouds with respect to discontinuity geometric information generated by traditional methods.

1.6.3. Research Questions

- Can the orientation and spacing of cemented discontinuities (mainly bedding planes) be measured from both UAV-based and TLS datasets?
- How the orientation and spacing of discontinuity planes derived from UAV-based photogrammetry and TLS datasets statistically compared?
- How consistent are the orientations and spacing derived from UAV and TLS datasets with respect to traditional methods?
- Which technique (UAV or TLS) offers more comprehensive 3D structure of the rock face compared to the traditional field methods?

2. LITERATURE REVIEW

2.1. Discontinuities in a rock mass

A rock mass or a ground mass contains fractures of one type or another that makes its structure discontinuous. Therefore, a rock mass consists of an assemblage of rock material and discontinuities (figure 2-1). Discontinuities are planes or surfaces, which indicate or introduce a change in physical or chemical properties of rock material. Discontinuities are generally categorized into two, namely mechanical and integral discontinuities. Mechanical discontinuities are well-developed plane of weakness in the rock mass. They represent planar breaks in the continuity of the intact rock blocks. Joints, bedding planes, fractures, faults, folds etc. belong to mechanical discontinuities. Integral discontinuities, on the other hand, represent an inherent discontinuity in the rock fabric that shows insignificant mechanical properties compared to the surrounding intact rock blocks. This means that integral discontinuities possess strength comparable to the surrounding rock material (ISRM, 1978). They are formed by bands of various mineral assemblages or due to the alignment of minerals in a certain direction. Foliation of gneiss and banding of rhyolite are a good example of integral discontinuities. Integral discontinuities can be developed into mechanical discontinuities due to weathering and change in stress regime. Throughout this thesis, discontinuities denote mechanical discontinuities unless mentioned otherwise.

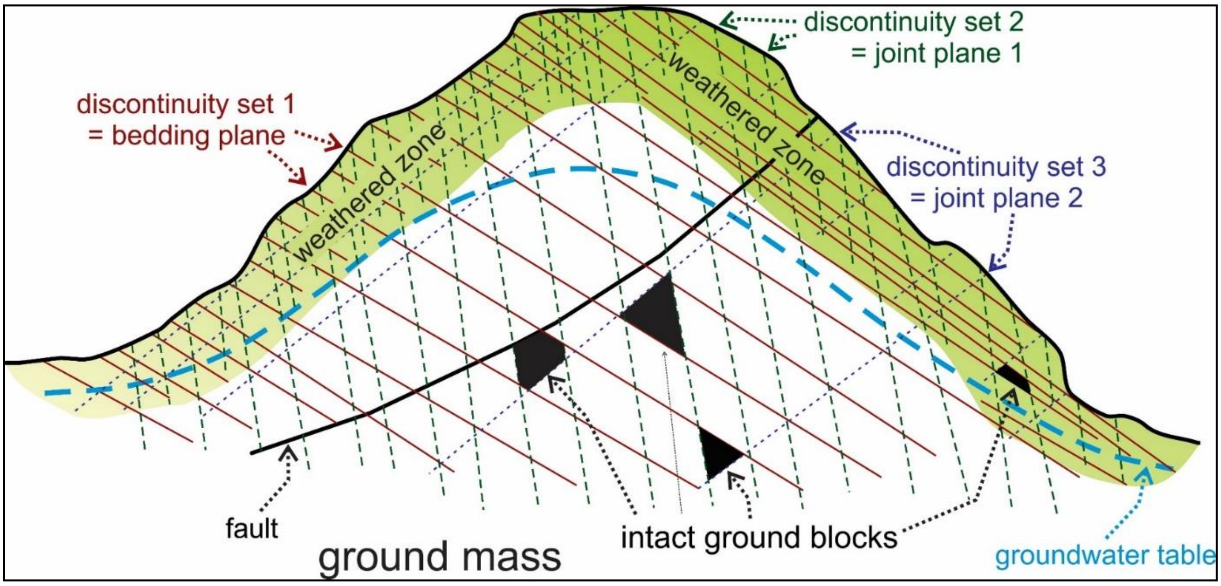

Figure 2-1: intact rock blocks and rock mass rendered discontinuous by discontinuities (Source: (Hack, 2016)).

The discontinuities often render the rock mass to exhibit heterogeneous and anisotropic engineering behaviours. Rock mass that possesses discontinuities is more deformable and weaker because the shear strength along and tensile strength perpendicular to the discontinuity surface becomes lower than the intact rock blocks (ISRM, 1981; Hack, Price, & Rengers, 2003). On the other hand, an intact rock material or block is free of discontinuities and possess tensile strength.

The most common discontinuities include bedding plane, joints, faults, shear zones, and dykes and veins. Brief definition and characteristics of discontinuity are as follows:

Bedding planes: it common characteristics of sedimentary rocks. It separates sedimentary rocks into successive beds or strata. Bedding planes are usually oriented horizontally. Due to tectonics, they may later get tilted, folded or faulted. Bedding planes mark a change in sedimentary material or interruption in the process of deposition. They usually exhibit high lateral persistence.

Folds: are discontinuities in which the beds are changed by flexure due to post-depositional tectonic effects. Other structural features may be associated with the formation of folds particularly well-defined set of joints.

Faults: faults are fractures on which recognizable movement or displacement has taken place. Faults are further classified depending on the style of movement as normal faults, thrust (reverse) faults, and strike-slip faults. Faults are usually exposed as echelon or in groups (Brady & Brown, 2006), and represent zones of low shear strength on which movement or slip has taken place.

Shear zones: form zones of stress relief, in which parallel layers of rocks are sheared. Slickensides and coating with low-friction material represent shear zones. Similar to faults, shear zones also possess low shear strength. They usually show more wide thickness than joints or bedding planes.

Joints: are the most geotechnically important discontinuity features in a rock mass. Joints are planes of weakness along which no or insignificant movement has occurred. They are formed when the inherent weakness of rock material fails to resist tensile stress. They often form in a direction of stress fields as clusters. Commonly, the stress regime that creates joints results from regional deformations of the earth crust. The main geological processes that have a role in the formation of joints include cooling of igneous rocks, unloading or removal of compressive load due to erosion or excavation, and tectonic deformation episodes.

Joints usually occur in a group or a cluster along a certain direction. A cluster of parallel joints is known as a joint set and often exhibit a regular spacing. The intersection of joint sets constitutes a joint system. Joints are either open, filled or healed.

Fractures: fractures are manmade discontinuities created by blasting, mechanical hammering or any other form of mechanical excavation. They often exhibit little persistence and occur in a random fashion.

Foliation: are usually found in metamorphic rocks in the form of cleavage or schistosity and sometimes in igneous rocks as banding. They constitute integral discontinuity. They are the product of preferred growth and orientation of rock constituent minerals under the impact of increased stress and temperature.

2.1.1. Discontinuity sets

Discontinuities occur as a single isolated feature (fault, single joint or fracture, etc.) or as a group or a family or usually termed as sets or clusters (bedding planes, joints, etc.). A set or a cluster represent a series of discontinuities in which the geologic origin, orientation, spacing, other mechanical properties are homogenous or the same.

2.1.2. Significance of discontinuities

Discontinuities are planes of weakness in a rock mass, and govern, to large extent, the behavior of the rock mass (Bieniawski, 1989). A good understanding of discontinuities in a rock mass is imperative in most civil and mining engineering projects that deal with rock mass because they serve as input data for rock mechanics analysis, rock engineering design, and numerical modeling (Slob et al., 2007). Generally, discontinuities

- Divide rocks into slabs, blocks, wedges, etc.
- Act as shear plane for sliding and moving, and
- Serve as a channel for transport of fluids and gasses.
- Influence local stress orientation and magnitude.

2.1.3. Prominent geomechanical properties of discontinuities

There are ten important parameters of discontinuities that impact the engineering characteristics of rock masses as outlined by ISRM (1978). Evaluation of the behaviour of the rock mass is performed via assessing these properties. These properties of discontinuities are broadly categorized into two as geometrical properties and non-geometrical properties. Geometrical properties of discontinuities have prominent significance for rock mass modeling and include orientation, spacing, roughness, and persistence. The non-geometrical properties are wall strength, aperture, nature of infill material, seepage, the number of sets, and block size. The non-geometrical properties are not suited to be measured or quantified. The geometrical properties of discontinuities are discussed briefly as follows:

Discontinuity orientation is the most pertinent geometric property of discontinuities since it controls the anisotropy of the rock mass. It represents the attitude of a discontinuity plane in space. Orientation is often described in terms of dip direction (azimuth) and dips angle (plunge). Dip angle is the maximum declination of the discontinuity plane measured with regard to the horizontal. Its value ranges from 0^0 (horizontal) to 90^0 (vertical). The dip direction is the line perpendicular to the strike direction, and it is measured clockwise from the true north. Its value ranges from 0^0 to 360^0. Orientation data are often recorded in the form of dip direction (three digits)/dip (two digits), as $035^0/70^0$ or $290^0/20^0$. Orientations of the joint system determine the shape of blocks in the rock mass (Brady & Brown, 2006). Orientations are measured by Compass or clinometer.

Discontinuity spacing is the perpendicular distance between adjacent discontinuities in the same set and often represented by the mean spacing of a particular set of joints. The spacing of joints in the rock mass, to large extent, determines the size of blocks, and hence impact the overall mechanical properties of the rock mass. The spacing of discontinuities can be accurately measured in the field by measuring tape. Priest, (1993) identified three type of discontinuity spacing measurements in the field in order to avoid ambiguity since all planes that belong to the same set are not always parallel to each other, and thus corrections must be applied to obtain the normal set spacing (figure 2-2).

-Total spacing: is the distance between two adjacent discontinuities measured along a scan line. Since the measured pair of adjacent discontinuity planes may not belong in the same set, the total spacing is not related to individual discontinuity sets. However, total spacing can offer an indication of the amount of fracturing in the rock mass.

-Set spacing: is the distance between two discontinuities that belong to the same set measured along a scanline. The disadvantage of the set spacing is that the set spacing of discontinuities that run parallel to the scanline is greatly overestimated.

-Normal set spacing: is the distance between two discontinuities that belong to the same set, perpendicular to the mean orientation of the set. Often, the normal spacing is not measured along a scanline, but generated from the set spacing via correction of the scanline orientation with respect to the normal vector of a set. The average of normal spacing gives the mean normal set spacing. Both normal set spacing and the mean normal spacing serve as a good index of block shape and size distribution in a rock mass and thus can be utilized in rock classification systems and numerical modeling programs.

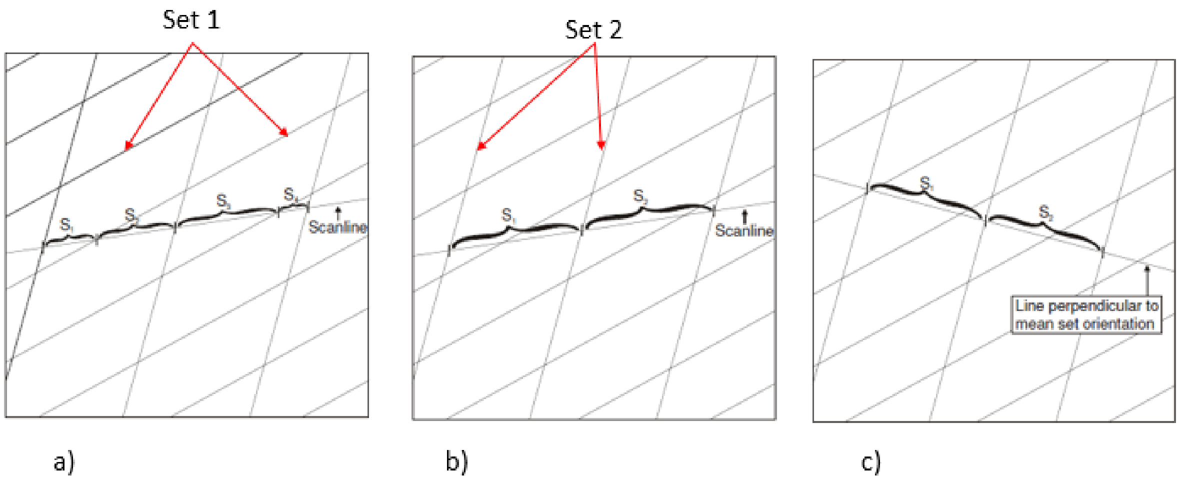

Figure 2-2: a) illustration of total spacing along a scanline; b)illustration of set spacing along scanline; c) normal set spacing along a line that trends parallel to the mean normal vector of a set (source: adopted from (Slob, et al., 2010)).

Roughness: surface roughness greatly impacts the shear strength of discontinuities. It is formed by inherent surface irregularities or unevenness or waviness on discontinuity planes. It is generally classified as large scale (on plane size in the order of meters) and small scale roughness (on plane size in the order of centimeters).
Persistence: is the continuation of discontinuities in a given direction. It is a measure of areal extent or size of a discontinuity plane. It can be roughly quantified from the trace length of discontinuities on exposed rock mass. Persistent discontinuities greatly influence the mechanical behaviour of rock masses. Persistence impacts the shear strength of discontinuity plane and fragmentation characteristics and permeability of the rock mass. It is measured or estimated both along strike and dip direction of discontinuity plane. Non-persistent discontinuities generally do not influence the mechanical behaviour of a rock mass.

2.2. Conventional methods of field discontinuity data acquisition

There are two most widely used conventional methods of acquiring discontinuity data from exposed rock mass in the field. These techniques include scanline mapping and cell mapping (Priest & Hudson, 1981; Priest, 1993). Their main difference is that the scanline technique is one-dimensional discontinuity survey method, but the cell mapping method is two-dimensional discontinuity mapping technique. However, both mapping methods enable to reconstruct the three-dimensional fabric of the discontinuities as they both provide a structured way of mapping and recording of discontinuities in the field. Furthermore, both techniques employ simple field equipment such as a geological compass for measuring discontinuity orientation and inclination, clinometer and a measuring tape for measuring the spacing and aperture of discontinuities.

2.2.1. Scanline discontinuity mapping method

Scanline mapping or line sampling method comprises an imaginary line or physical line (this is the reason scanline is termed one-dimensional mapping method) placed on rock exposure. It is a technique applied to determine the characteristics of discontinuity properties in a rock face by averaging of the properties of all individual discontinuities intersecting the scanline. The line is usually measuring tape stretched across the discontinuity planes. Therefore, planes or traces of discontinuities that cross or intersect the line are mapped. During scanline survey, detailed information about important properties of an individual discontinuity or sets such as intersection distance, orientation, and inclination, semi-trace length, termination, and roughness are acquired. The information later can be used in a probabilistic design (ISRM, 1978; Priest, 1993; Kulatilake, Wathugala, & Stephansson, 1993). Besides, the scanline orientation should also be recorded in the field as it will be used for data correction later in the lab. The advantage of scanline survey is that discontinuity spacing data and orientation are collected systematically.

During scanline survey, a measuring tape of 2 to 30m is stretched at different orientations along the rock exposure. The orientation of the scanline should be selected in such a way that as many discontinuities as possible can be intersected. However, scanlines are usually placed at easily accessible locations on the rock face. This means that only part of a rock face or exposure is mapped depending on the height and accessibility of the slope. In addition, discontinuity sets that have large spacing might be missed or discontinuity planes that run parallel or at low angles (<100) to the scanline are usually missed or under-sampled and thus sampling bias is introduced. Terzaghi (1965) devised compensation for directional bias during scanline survey, though the corrections cannot be applied for discontinuities that intersect the scanline at a low angle. Consequently, In order to reduce discontinuity orientation sampling bias or associated spacing error, the scanlines should be preferably oriented orthogonal to the representative discontinuity sets. Priest (1993) recommended employing at least three scanline surveys. For instance, one horizontal scanline and two or more vertical scanlines so that discontinuity set missed by one scanline can be possibly intersected by the other scanline.

2.2.2. Cell mapping

Cell mapping or window sampling discontinuity mapping techniques are two-dimensional and comprise the selection and outlining of a square window on the rock exposure. Properties of the discontinuities or traces thereof that fall within the window are measured and mapped. In order to minimize sampling bias, Priest (1993) recommended outlining a window as large as possible, so that 30 to 100 discontinuities would be intersected. Similar to the scanline method, it is preferable to execute two mutually orthogonal cell maps or map two mutually orthogonal rock exposures in order to reduce or avoid sampling bias. Compared to scanline, the linear orientation sampling bias is avoided in cell mapping as all discontinuity orientations are equally mapped within the sampling window. However, cell mapping provides a poor network of the geometry of individual discontinuities (Clayton, Matthews, & Simons, 1995). Generally, cell mapping method involves more labor intensive task than scanline when similar precise sampling schemes are applied.

2.2.3. Rapid face mapping

For a preliminary assessment of a rock exposure, scanline or cell mapping methods are not required since both methods could miss very important discontinuities or even the entire discontinuity set as the survey is spatially restricted. Hack et al. (2003) developed, based on rapid face mapping, a new method of slope stability probability classification (SSPC). He asserted that for most engineering geological applications, it is adequate to identify the main discontinuity sets in a rock mass exposure, and then characterize discontinuity properties of each set such as a representative orientation and spacing. However, in large rock mass exposures, it is imperative to first classify or separate the rock mass into homogenous rock mass units, or geotechnical units in order to perform discontinuity assessment. Then, discontinuity assessment is executed for each geotechnical unit separately. This method allows rapid acquisition of a reasonably accurate engineering geological data and assessment of the whole rock exposure. However, this system doesn't allow statistical analysis of the discontinuity data because huge data or a minimum of 150 discontinuity measurement is required for statistical analysis as suggested by ISRM (1978). Furthermore, the SSPC is not systematic and may present human bias, as it requires a reasonable field experience to classify rock mass exposure into different geotechnical units and recognize the most prominent discontinuity sets. In order to minimize the human bias, Hack et al. (2003) developed a field format that contains a checklist that helps to characterize the rock mass based on the most prominent properties and parameters of geotechnical units and discontinuity sets.

2.3. Principles of Terrestrial Laser Scanning (TLS)

Since the year 2000, TLS has become revolutionary geo-data surveying technology for fast acquisition of three-dimensional (3D) information of different topographic and industrial objects (Lemmens, 2011). It has been successfully applied to accurately model and document cultural heritages, bridges, plants, cars, coastal cliffs, highways, etc. TLS is non-contact measurement instrument that generates a 3D digital representation of surface of a target object (Vosselman & Mass, 2010). It acquires and records the geometry and textural information of target object in the form of point clouds. Broadly, there are two basic measurement principles that are used in terrestrial surveying: time-of-flight (time-based) and phase-based techniques. Time-based system measures emitted and reflected laser pulses, while phase-based lasers measure phase difference and frequency modulation. The former can hit longer ranges of up to 1000m, while the latter measures with short range up to 25m, but with more accuracy (<10mm) and faster acquisition rate. Most of the scanners used for surveying are time-based once due to their long range capability. There are numerous models of laser scanners in the market that are manufactured by different companies. For instance, Leica-Cyrax and Riegl are common scanner providers. Though the basic principle behind the scanner is the same (for example in all time-based scanners), their difference lies in the accuracy, precision, resolution, angular field of view, scanning speed, and laser beam divergence.

Fundamentally, all Lidar or Terrestrial laser scanners measure range and intensity of terrain points struck by the laser beam (Lemmens, 2011). A laser is a narrow, intense, monochromatic coherent beam of light generated by a laser device, such as TLS. Thus, TLS is an active optical 3D measurement sensor, and most of them are categorized under time- based measurement technique. The time-based lasers, (also known as ranging scanners) emit pulses of electromagnetic radiation, and their travel time to and back from scanned object is precisely measured using the known speed of light. Thus, using reflected beam of light from the surface of the scanned object the distance from the laser to the object, both the azimuth and zenith angle of the beams, and the relative position of each point where the beam is reflected can be computed to generate the XYZ Cartesian coordinates. The product of the survey is the acquisition of 3D dense point clouds that accurately represent the geometry of the scanned object. Each point represents x, y, and z coordinates of the scanned object relative to the scanner. The spatial resolution of the point clouds is in the order of 5 to 10mm depending on the range (distance to the target object) and type of the scanner (Slob & Hack, 2004). In addition, the intensity of the reflected signal from the object is also recorded along with colour information from the digital camera mounted on the top of the scanner.

2.3.1. Sampling bias and influence of vegetation in TLS survey

Sampling bias in laser scanning survey occurs due to occlusion (shadowing) of the scanned rock outcrop. It is caused when the laser beam is blocked from reaching the target rock face. Parts of the rock face that are semi-parallel to the incoming laser beam and benched slopes are usually affected. This results in overrepresentation of discontinuity surfaces parallel to the general strike of the rock face, while those discontinuity surfaces that are orthogonal to the general strike of the rock face are underrepresented (Slob & Hack, 2004).

Furthermore, Slob & Hack (2004) stated that during scanning of the vertical or steep rock face, the upper part of the slope is prone to occlusion due to the large incidence angle of the laser beam hitting the slope. This results in under-sampling of discontinuity surfaces that dips out of the slope. This problem is termed vertical sampling bias. In order to minimize the effect of occlusion, it is recommended to scan the rock face from different positions. This allows scanning the areas obscured during the previous scan survey. However, multi-scan surveys require co-registration or merging of the point clouds. Besides, vertical sampling bias remains difficult to minimize though merging of the different scans can minimize the effect of horizontal sampling bias.

Dense vegetation with broad leaves grown on the rock face can obstruct the incoming laser beams and results in occlusion. If vegetation is present in front of the rock face, it can cause noise in the point clouds but can be later filtered manually. However, the impact of vegetation on the rock face can be reduced if subsequent data analysis entails segmentation of the point clouds (Slob & Hack, 2004).

2.3.2. Application of TLS for rock face discontinuity characterization

A number of researches carried out have shown that discontinuity information can be accurately derived from TLS dataset via automatic techniques (Slob & Hack, 2004; 2007; Sturzenegger & Stead, 2009; Ferrero, Forlani, Roncella, & Voyat, 2009; Gigli & Casagli, 2011; Riquelme, Abellán, & Tomás, 2015; Salvini et al., 2015). Slob & Hack (2004) is one the most prominent work in the field of rock mass characterization using 3D TLS. They used both surface reconstruction and segmentation techniques to assess which approach yield more accurate discontinuity data in an automated way, and thus concluded that segmentation technique is more preferred to characterize rock mass since it doesn't require prior surface reconstruction. The advantage of TLS is that it allows fast acquisition of dense point clouds that accurately represent the 3D geometry of rock face. With TLS, data can be acquired from several hundreds of meters safely within short time though the accuracy and precision of the output data are affected by the range. Via different semi-automatic/automatic techniques, different properties of discontinuities can be extracted. Margherita et al. (2015) studied the structural features driving slope instability in the San Leo Village, Italy, using integrated

TLS, close range photogrammetry, and scanline survey. They were able to extract discontinuity features and defined fractured areas from DSM generated from images, and TLS point clouds. The result was utilized as input data to define kinematic analysis, in order to assess joints sets that predisposed slope instability. They emphasized that remote sensing and traditional methods of discontinuity mapping should be carried out in an integrated manner to get a more complete representation of rock mass 3D geometry since they complement each other. They further suggested that the use of UAV would even offer more accurate data covering a wider area. Nonetheless, the use of TLS as appropriate remote sensing tool for characterizing rock face is often constrained by high equipment cost and associated training (Chesley, Leier, White, & Torres, 2017). Therefore, nowadays, the emphasis is being offered to UAV photogrammetry since the technique is easier-to-use, more flexible and cheaper alternative remote sensing tool for rock mass characterization.

2.4. Principle of Photogrammetry

Photogrammetry is a technique that extracts 3D information of features from two or more 2D photographs of the same object, captured from different positions (Haneberg, 2008). Associated with UAV is the structure from motion (SfM) photogrammetric technique, in which camera positions and orientation are determined automatically, unlike traditional photogrammetry where a prior knowledge of these parameters is required (Westoby et al., 2012; Colomina & Molina, 2014). SfM uses overlapping photos to generate 3D point clouds, from which it is relatively, straightforward to compute surface models such as triangular meshes, digital elevation models (DEMs) and finally derive orthorectified photomosaic or textured surfaces. However, point clouds generated by SfM process can further be densified using Patch based multi view stereo (PMVS2) method (Furukawa & Ponce, 2010). The general workflow of SfM consists of a) identification and extraction of key points in each image, b) matching of key points among images, c) automatic aerial triangulation and bundle block adjustment to estimate and refine camera pose, d) processing of the oriented and refined photos to generate point clouds, and finally e) generating DSM and Orthomosaic. The SfM and PMVS2 processes are automatically computed in commercial software such as Pix4DMapper and Agisoft Photoscan.

2.4.1. Application of UAV for discontinuity characterization

The UAVs are nowadays being utilized in various applications in the close range aerial domain, providing cheaper and flexible alternative to the classical manned aerial and terrestrial photogrammetry for both large scale and detailed 3D representation of topography (Nex & Remondino, 2014; Chesley et al., 2017). The UAVs can offer reliable information about the shape of the rock surface, volume, and their stability, and thus, a powerful, fast, inexpensive and reliable alternative to terrestrial laser scanners for monitoring excavation activities in mine and quarry areas. Mancini et al. (2013) evaluated the use of UAVs and TLS for high-resolution topographic modeling of coastal environments. Using SfM approach, they managed to generate dense point clouds and subsequent DSM of beach dune system from imageries captured by a UAV. The result showed point clouds and subsequent DSM generated from the UAVs data set were comparable and showed a good correspondence with TLS dataset. Furthermore, Bemis et al. (2014) compared the use of ground-based and UAV-based photogrammetry as multi-scale and high-resolution mapping of geologic structures on rock exposures. Both methods were able to generate high-resolution point clouds and textured DEMs. Nonetheless, surveying with UAV showed added advantage of offering access to vertical or unstable rock faces with reduced occlusion.

Moreover, Vasuki et al. (2014) mapped geological structures of a layered meta-sedimentary sequence cross-cut by a series of dikes from 3D surface models generated using UAV-based photogrammetry. They calculated the dip direction and dip of the structures using RANSAC algorithm to determine the best-fit plane, and the results showed orientations of faults computed using the automated method matches well with the data obtained by traditional mapping. Fakunle, (2016) did a research on detection of weathering of

Romberg sandstone quarry using UAV data set in comparison to TLS dataset and found out that UAV-based point clouds were more optimal than TLS point clouds in detecting rock mass weathering signatures. Besides, she attempted to map discontinuities from the two point cloud datasets using RANSAC automatic shape detection plug-in tool in cloud compare software and claimed to have identified the general orientations of two joints sets and a bedding plane. However, relevant discontinuity parameters such as orientation and depth were not derived and quantified from the datasets. Therefore, from literature review it can be noticed that the application of UAV for geomechanical characterization of a rock face is gaining momentum due to the advancement in image matching algorithms, widely growing of both open source and commercial software and ever increasing computer processing capabilities.

2.5. Point cloud direct segmentation techniques

Two basic approaches can be applied to automatically extract discontinuity properties of a rock mass from point clouds derived either from laser scanning or photogrammetry: These include segmentation of point clouds and reconstructing a 3D surface from point clouds. However, point cloud segmentation approaches are more advantageous in that they utilize the original point cloud, thus no data loss, which is inevitable in surface reconstruction approaches. In addition, segmentation techniques are not strongly impacted by the presence of vegetation on the slope and other artifacts in the data (Slob & Hack, 2004; Knapen & Slob, 2006; Gigli & Casagli, 2011). However, segmentation techniques are disadvantaged by big size of input data, which may take longer computation time. Besides, prior to segmentation, the unorganized point cloud data need to be structured via a tree-based or TIN-based structuring procedures to efficiently execute the segmentation process.

Point cloud segmentation is a technique that deals with segmenting or classifying point clouds (both derived from Lidar or photogrammetry) into subsets that contain the same geometric shape through a tree-structuring procedure. This method is based on the assumption that certain pre-defined geometric shapes (namely, cylinders, spheres, planes, etc.) are contained in the point cloud data. Analysis of the point clouds via segmentation techniques recognize and define the geometric shapes. Planar shapes are appropriate geometric shape for representing discontinuity planes in the point cloud data. In order to recognize and define the desired planar geometry, point cloud segmentation applies region- growing strategy, in which small sub-sample sets of the point cloud data are continuously and recursively evaluated if they belong to the same planar object. The process starts with selection of a random seed point having a certain pre-defined number of points or choosing points within a predetermined search area around a seed point. Via repetitive spatial searches, the neighboring points of the seed point are evaluated whether they belong to a particular shape, in this case a plane. Thus, points that belong to the same surface or plane are uniquely labeled (Rabbani et al., 2006). The products of segmentation process are classified or labeled point clouds, in which, point clouds with the same label are grouped into same discontinuity plane. The classified and labeled point clouds are then processed further to derive geometric discontinuity properties.
In summary, the direct segmentation technique primarily entails three steps: structuring of the point cloud data using a tree-structuring strategy before segmentation, region growing to segment the point cloud data into set of independent planes, and evaluation of planarity using either Hough transform (Vosselman, Gorte, Sithole, & Rabbani, 2004), (Total) Least Squares Analysis (Feng et al., 2001), Random Sample Consensus (RANSAC) and Principal Component Analysis (Slob et al., 2005). 3-D Hough transformation and Total Least Squares Analysis were applied in this research.

3. STUDY AREA

3.1. Location and climate of the research area

The study area is located in Romberg quarry, near the town of Gildehaus (Bad Bentheim), in the state of lower Saxony, northwest Germany. It is situated 20km north east of Enschede, close to the border of the Netherlands and Germany (figure 1). The quarry site is located at geographic locations of 52030’24” North and 07010’25” East. The climate of Bad Bentheim area is characterized by warm and temperate maritime climate impacted by warm Gulf Stream which flows of the coasts of Netherlands and Belgium. During hot summers the monthly temperature ranges from 11 to 22^{0}C, and during moderate winters the temperature ranges from -1 to 4^{0}C. The mean monthly precipitation during long rainy periods from September to January ranges 61 to 100mm. Snow fall is common in the area during winter periods.

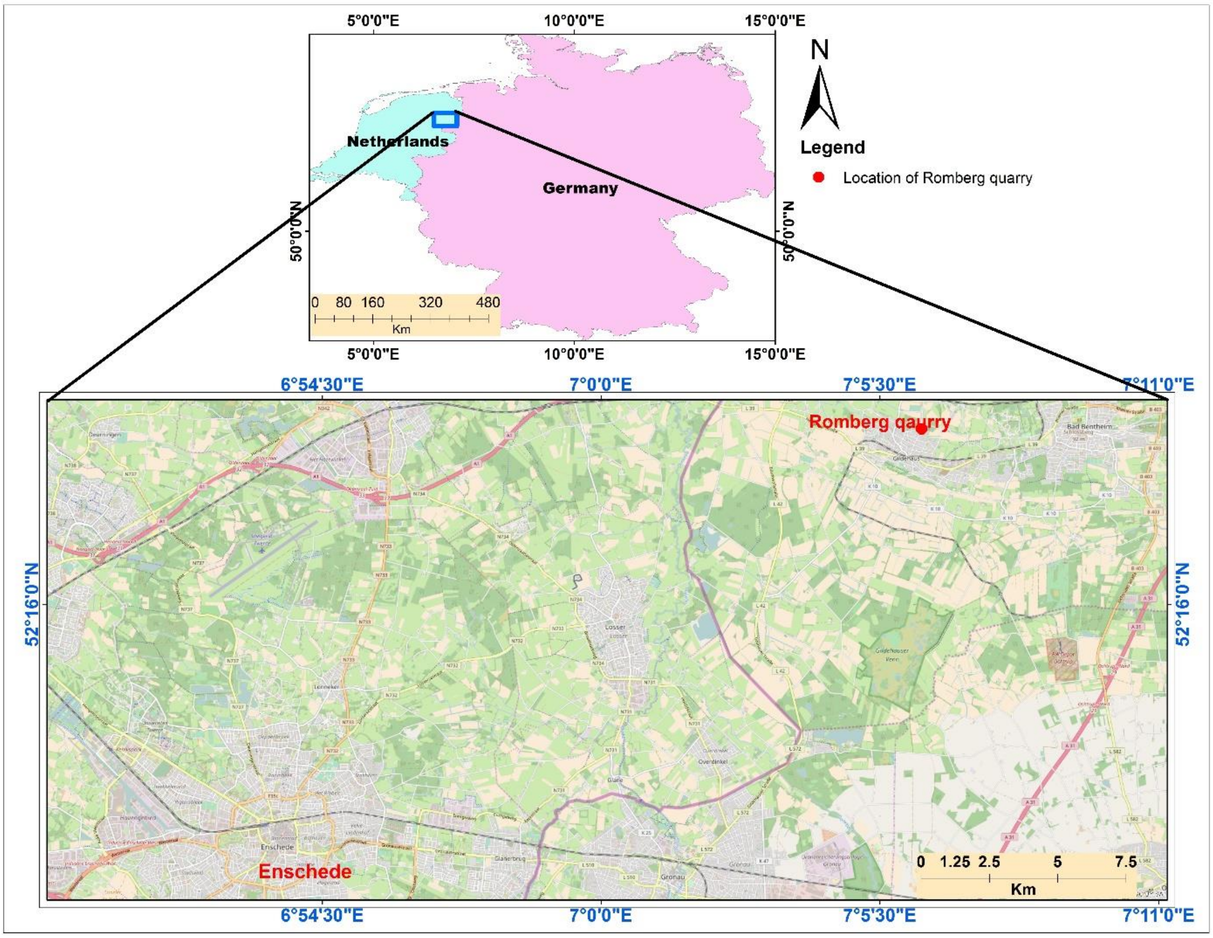

Figure 3-1: Location map of the research area. Source: Esri file geodatabase and Open streetMap

3.2. Regional geological setting and structures

A number of prominent basins were present in the northwest Europe during the Early Cretaceous. One of the basin was the Lower Saxony Basin (LSB) located in the North West Germany, which is roughly 400km long and 100km wide and oriented in northwest-southeast direction extending from east of the Netherlands to the north of Harz Mountains in Germany. The LSB is bounded by Rhenish Massif from the south, Pompeckj Basin from the North, East Netherlands High from the west and East Brandenburg High from the east (figure 2a). The evolution of the LSB occurred during late Jurassic to Early Cretaceous, and controlled by divergent dextral shear movements, which were related to the contemporaneous rifting in the

North Sea Central Graben (Ziegler, 1990) as cited in (Wonham, Johnson, Mutterlose, Stadtler, & Ruffell, 1997). Differential subsidence of the LSB began in the Late Jurassic and persisted throughout the Early Cretaceous. During these periods a marine transgression in the LSB initiated deposition of fossiliferous Claystone and quarzitic sandstone. Marine conditions persisted and deposition of Shales and carbonates, evaporitic deposits, and continental and lacustrine sediments took place across the LSB over a topography of horst and graben (Betz et al, 1987) as cited in (Wonham et al., 1997). Reduction of tectonic activity commenced to occur at the beginning of Late cretaceous ensued by inversion, which began in Early Coniacian and lasted until Early Tertiary. The cumulative inversion resulted in the uplift of the basin floor by 1000 to 2000m and erosion of much of the central part of LSB. The structural setting of the LSB is currently characterized by open folds, thrust faults and other wrench induced structures.

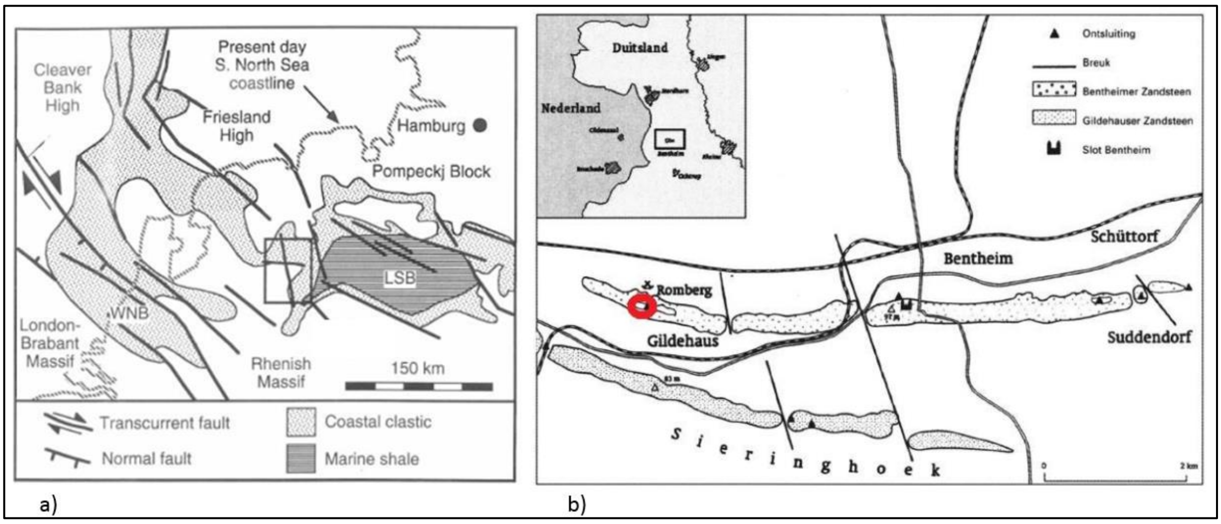

Figure 3-2: a) Paleogeography and structural framework of the Lower Saxony Basin during Berriasian-Valanginian. Source: (Ziegler, 190) as cited in (Wonham, et al., 1997); b) East-west aligning ridges of Bentheim sandstone. The red circle denotes the location of Romberg quarry. Source: (Nijland, et al., 2003) as cited in (Traska, 2014).

3.3. Geological and engineering geological characteristics of Bentheim Sandstone

The Bentheim sandstone forms the western part of the Lower Saxony Basin and extends continuously for over 10km with an average width of some 400m. It forms a ridge that is part of a limb of an east-west running anticline, dipping 10-20^0. It had been massively mined from the ridges between the Gildehaus and Bad Bentheim. Presently, it is exploited at Romberg quarry in Gildehaus (figure 2b). It was deposited in shallow-marine environment. It has been the host rock or reservoir for numerous oil and gas fields in the northwest Germany and the Netherlands (Fuchtbauer, 1955) as cited in (Dubelaar & Nijland, 2016). The depositional environment of the Bentheim sandstones forms facies patterns that show domination of tidal or current processes throughout the deposition.

The Bentheim sandstone is a quartz arenite sandstone containing locally extensive marine claystone or siltstone units at intervals. It attains the maximum thickness of up to 125m in the Bad Bentheim area. In Romberg quarry, where the location of this research is based, the Bad Bentheim sandstone is divided into three main lithostratigraphic units based on measurement of sections taken from the quarry (Dubelaar & Nijland, 2015). These sections comprise the lower Bentheim sandstone, which has over 27m thickness, the Romberg Claystone which is about 3.5m thick and the Upper Bentheim sandstone with a thickness of over 6m (Wonham et al., 1997). The lower Bentheim sandstone dominantly consists of thickly bedded to massive layers, and exhibits clastic texture. At places it is intercalated with cross-bedded sandstone with thin clay drapes. Most of dimension stone or building blocks have been mined from the lower Bentheim sandstone characterized by medium grained, and massive beds.

Mineralogical and petrophysics studies conducted in the past showed that the Bad Bentheim sandstone consists of well-sorted, medium grained sand. It has quartz as main constituent mineral (up to 97%) with accessory minerals such as feldspars, zircon, tourmaline and heavy minerals. The Bentheim sandstone has a porosity as high as 26% and permeability in the range of 0.97 to 2.14Darcy from rock samples examined from Romberg quarry. The size of the pores ranges from 0.025 to 0.1mm. There are also the occurrence of oversized pores in the rock attributed to the dissolution of feldspars. The primary porosity of the rock has been preserved due to quartz cementation. The silica cement also helped to resist the effect of overburden pressure and thus lowered the mechanical compaction of the sandstone in Romberg quarry (Malmborg, 2002). The Bentheim sandstone has an apparent density of in the range of 2.04 to 2.12g/cm^3, and compressive strength of 48 to 77N/mm^2 (Dubelaar & Nijland, 2015).

3.4. Historic use of Bentheim Sandstone as building stone

Historically, the Bentheim sandstone has been quarried since the 10th century for the purpose of dimension stone and industrial use (Dubelaar & Nijland, 2015). Numerous historical monuments, castles and cathedrals in the east Netherlands and Northwest Germany were made out of dimension stones mined from Bentheim sandstone. For instance, the Royal palace in Amsterdam, the St. Lawrence Tower in Rotterdam, the Dom located in Utrecht are some of the known buildings made with Bentheim Sandstone (Traska, 2014). The compactness, homogeneity, high quartz content and small amount of clay and carbonate, and durability has made the Bentheim sandstone a suitable and workable dimension stone for various purposes (Klein, Baud, Reuschlé, & Wong, 2001; Dubelaar & Nijland, 2016). The absence or limited development of lamination within the massive beds of the Bentheim sandstone precludes it from easily splitting apart. Flaking and blistering of the rock is uncommon. The most typical Bentheim sandstone presently mined for building stones in Romberg quarry are off-white (cream or a pale yellow) colour. However, darker, ochre to red sandstones are commonly outcropped in Bad Bentheim area, typically in the former quarries Amkathagen and freilichtbuhne. Its reddish appearance is attributed to the coating of the quartz grains by iron oxide hematite (Dubelaar & Nijland, 2015). The red sandstones of Bentheim area are characterized by high clay mineral content than the pale yellow sandstones, though the origin and nature of the clay minerals that fill the pores is not completely understood.

A preliminary field survey of the Bentheim sandstone at Romberg quarry site showed that the sandstone consists of light reddish-brown to whitish, medium to coarse grained, bedded, jointed and is tilted toward the south by 20 to 30^0. The rock mass has been classified into different geotechnical units representing different degrees of weathering and joint spacing. Detailed characterization of the slope is shown in result and discussion chapter of the thesis.

In this chapter, the location of the research area was explained, regional geological setting and structures has been reviewed, and overview of the geological and engineering geological characteristics of the Bentheim sandstone was given. Furthermore, the historic use of Bentheim sandstone as building stone was shortly described.

4. METHODOLOGY

4.1. Rock mass characterization using the SSPC method

Field geological data acquisition from accessible part of the Romberg quarry slope was carried out in March 2017. Characterization of rock mass exposure was performed using the SSPC method, which is based on rapid face mapping technique, proposed by Hack et al. (2003) pursuant to established standards such as BS 5930 (1999), ISRM (1978), and ISO 14689-1 (2003). Based on SSPC system, the rock mass was first delineated, visually and with the help field geological instruments, into five major geotechnical units. The criteria used to classify the rock mass into the geotechnical units are joint spacing and bedding plane thickness, the degree of weathering, intact rock strength, and lithological types exposed.

Subsequently, discontinuity properties, the degree of weathering, and intact rock strength of each geotechnical unit was characterized either visually from a distance where the slope was inaccessible or with a geologic hammer, tactile or hand contact, taste, geologic compass, handheld lens, and measuring tape where the slope was accessible.

characterization of the degree of weathering or weathering grade of each geotechnical unit was also made following BS 5930 (1981) as attached in the appendix A. Furthermore, Intact rock strength of each geotechnical unit measured as compressive strength, where accessible, was estimated based on "simple means" method by using a geological hammer as outlined in BS 5930 (1999), and ISO 14689-1 (2003) as attached in appendix A.

4.1.1. Measurement of discontinuity properties using the SSPC

The discontinuity properties characterized in the field include orientation and inclination, spacing, and the condition of the discontinuity, i.e. surface roughness both in large and small scale, persistence along dip and strike, and infill material. Representative discontinuity sets are visually selected and several measurements are taken with geologic compass to determine their mean orientation (dip direction) and inclination (dip angle). Hack & Price, 1996 that this method provided equal or better results than extensive measurements of discontinuities for statistical analysis using other methods. The spacing of the discontinuities was measured with a measuring tape. The orthogonal distance between discontinuities in each set was measured to obtain normal set spacing without the need for further correction. The mean set spacing was calculated by taking the average spacing of each discontinuity belonging to the particular set. The spacing of joints and bedding planes were qualitatively and quantitatively described following BS 5930 (1999) and Hack et al. (2003) as outlined in table 4-1 below.

Table 4-1: Qualitative and quantitative characterization of discontinuity spacing following (BS 5930, 1999).

Discontinuities (Joints)		**Bedding planes**	
Term	Mean spacing in mm	Term	Mean thickness, mm
Very widely	Over 2000	Very thickly bedded	Over 2000
Widely	2000 to 600	Thickly bedded	2000 to 600
Medium	600 to 200	Medium-bedded	600 to 200
Closely	200 to 60	Thinly bedded	200 to 60
Very closely	60 to 20	Very thinly bedded	60 to 20
Extremely closely	Under 20	Thickly laminated	20 to 6

The condition of discontinuities in large scale for each plane was characterized either as wavy, slightly wavy, curved, slightly curved, or straight based on visual assessment and tactile. Characterization of surface roughness of discontinuities on large scale is carried out on an area between 0.2 x 0.2 and 1 x 1m2 on the rock face. On the other hand, the small-scale roughness of each discontinuity plane is described on an area of 0.2 x0.2m2. Main qualitative description of small scale roughness includes stepped, undulating or planar. Each scale may further classified into rough, smooth or polished. For instance, rough stepped or polished planar. Discontinuity persistence along dip and strike of each discontinuity plane was also measured by measuring tape and recorded. Infill materials were described as either cemented infill, non-softening and sheared material or soft sheared material or gouges for each aperture between two discontinuities as outlined in the SSPC format.

4.2. Field discontinuity data acquisition using scanline method

Four scanline surveys were carried out on the lower section of Geotechnical unit 5 in accordance with the method suggested by Hoek & Bray (1981a). These include one vertical scanline across the bedding planes, one horizontal scanline along bedding planes and two scanlines at an inclined angle to intersect both bedding planes and joint systems. The orientations of the scanlines were chosen in order to minimize sampling bias and map all possible discontinuity sets. A measuring tape was stretched along the rock face and discontinuities that intersect the line were measured. Subsequently, statistical analysis of measured discontinuity properties particularly orientation and spacing obtained by scanline method.

4.2.1. Analysis of discontinuity orientation

Discontinuity data collected from the field must be evaluated and analyzed to appropriately present the result irrespective of the data acquisition method. The evaluation and analysis of discontinuity data in this research entail mainly the assessment of orientation and spacing. Statistical analysis and visualization of discontinuity data, particularly orientation, allows resolving difficulties of recognizing discontinuity sets in the field and assess their orientation. 3D discontinuity orientation data is graphically presented in a hemispherical projection, whereas discontinuity spacing is statistically presented in the form of histograms (Goodman, 1976; Hoek & Bray, 1981b; Priest, 1985). Representation of discontinuity orientation is discussed in detail in appendix B.

4.2.2. Determination of discontinuity normal spacing

The normal set spacing distribution and mean normal set spacing of discontinuities are the two prominent parameters derived from scanline survey. However, during scanline survey in the field, apparent joint spacing are usually measured and recorded as the intersection distances of the discontinuities on the scanline. Therefore, the apparent spacing of discontinuities has to be converted to the normal spacing or orientation sampling bias due to linear sampling must be corrected. The relationship between the apparent spacing (S_α) and normal spacing (S_n) is mathematically defined by:

$$S_n = S_\alpha \cos\delta \qquad [13]$$

Where, δ is the acute angle between the normal of each discontinuity plane and scanline bearing (figure 4-2). The inclination angle, δ can be calculated by equation [14]:

$$\cos\delta = |\cos(\alpha_n - \alpha_s)\cos\beta_n\cos\beta_s + \sin\beta_n\sin\beta_s| \qquad [14]$$

Where, α_n and β_n are dip direction and dip angle of the normal of the discontinuity plane respectively and α_s and β_s are the bearing and plunge of the scanline respectively.

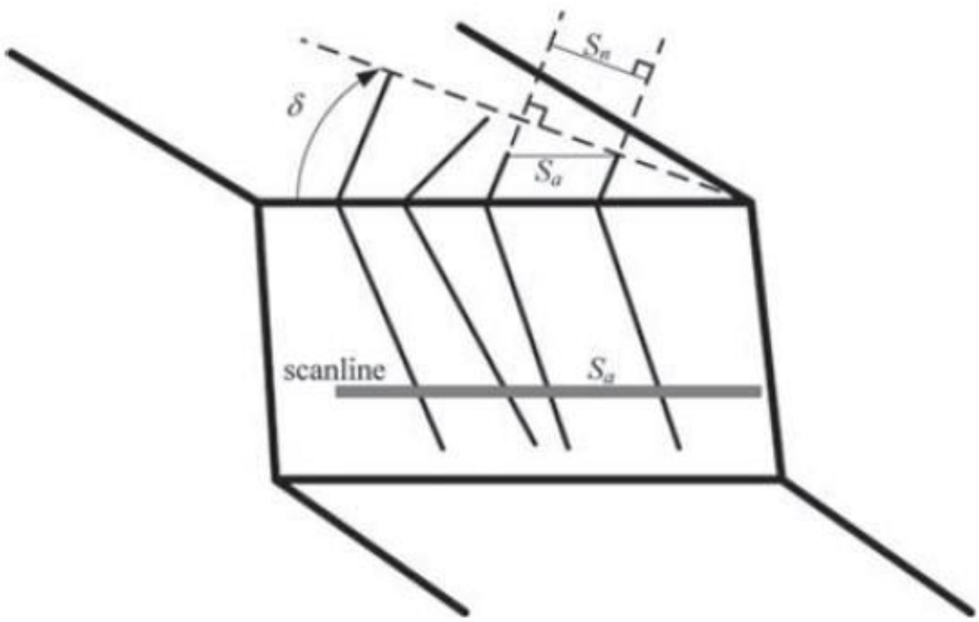

Figure 4-1: Relationship between apparent discontinuity spacing(S_{α}) and normal spacing (S_n) on a rock face (modified from ISRM (1978) and Giani (1992) as cited in Wong, (2013)).

The equation [13] can be expressed as [14] by defining the reciprocal of $\cos\delta$ as w.

$$S_n = S_a/w \qquad [15]$$

Where, w represent the correction factor for correcting the orientation sampling bias introduced by linear sampling of scanline survey (Terzaghi, 1965; Priest, 1993).
The following steps show the procedure to calculate normal spacing from apparent spacing as adopted from Slob et al., (2010).

1. Categorize the discontinuities that belong to the same set. This can be done by either plotting of all the discontinuity orientations in the stereonet (Appendix C) or the use of spherical directional statistics (section 4.4) or the application of fuzzy k-means clustering (section 4.9.1).
2. Sort the intersection distances of each discontinuity that belong to the same set.
3. Subtract each subsequent intersection distances to obtain the apparent set spacing.
4. Compute the acute angle between each discontinuity normal in the set and the scanline bearing.
5. Compute the average of all the cosine of acute angles obtained in step 4.
6. Multiply each set apparent spacing with the average of the all the cosine acute angle obtained in step 4 to obtain the normal set spacing.
7. Plot the normal spacing in a histogram if sufficient data is available otherwise computation of the mean normal set spacing is sufficient.

4.3. Computation of discontinuity orientation

For point cloud data a minimum of three coordinate measurements per discontinuity plane would suffice computation of orientation of smooth and flat discontinuity plane. The basic algebra of plane equation is given by the equation:

$$ax + by + cz + d = 0 \qquad [1]$$

Where d is the perpendicular distance from the plane to the origin. The plane parameters a, b, and c make up the normal vector n to the plane, which is given by the equation:

$$\bar{n} = \begin{pmatrix} a \\ b \\ c \end{pmatrix} \quad [2]$$

The plane equation can be rewritten with respect to its dip direction and angle of dip as:

$$\sin(\theta)\sin(\Upsilon)x + \cos(\theta)\sin(\Upsilon)y + \cos(\Upsilon)z + d = 0 \quad [3]$$

Where, θ is dip direction of the plane, ranging from 0 to 360^0 and ϒ is the angle of dip of the plane ranging from 0 to 90^0.

4.4. Analysis of clustering of poles and spherical directional statistics

Clusters of discontinuity poles plotted on a stereographic projection display specific distribution pattern or shape. The shapes or distribution patterns of poles on stereographic projection is called orientation model (Kulatilake et al., 1993). Several statistical methods are available that are used to analyzing discontinuity orientation in 3D. The most prominent once are Fisher distribution and Bingham distribution (figure 4-2).

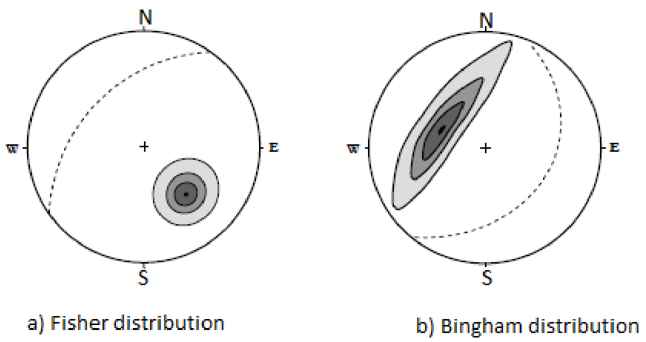

Figure 4-2: a) Fisher spherical data distribution representing a circular-symmetrical orientation of a single discontinuity set after Fisher, (1953) b) Bingham distribution representing an elliptical spherical data distribution after Bingham, (1964).

Fisher distribution is one of the most widely applied statistical models that provides measures of dispersion of orientations about the mean (Fisher, 1953). It defines the symmetric dispersion of discontinuity orientations around the mean by two parameters, namely a mean vector direction, θ, and a parameter characterizing the dispersion, K. K is known as the Fisher constant. The larger the value of K, the less the dispersion of values around the mean orientation. A random distribution of poles results in a K value of zero. In the Fisher distribution, clusters of poles are plotted as a circular pattern or shape because the dispersion, K, is assumed to be symmetric around the mean direction.

In contrast, the Bingham distribution statistical model is used to represent the orientation of curved or wavy discontinuity planes (Bingham, 1964). It makes up asymmetrical elliptical patterns on a stereographic projection.

Normal statistics cannot be used for the analysis of directional discontinuity data. Thus, either direction cosines or eigenvalues or Eigen vectors of the pole of discontinuity plane can be used to compute spherical statistics such as mean vector orientation, and the Fisher K, dispersion about the mean orientation. In order to compute directional statistics of discontinuity planes, their dip directions and dip angles in degrees must be converted to the three-dimensional Cartesian coordinate system (Goodman, 1976). The conversion equations and spherical calculations involved are shown below in equation 4.

$$\begin{aligned} x_i &= cosD_i sinA_i \\ y_i &= cosD_i sinA_i \qquad [4] \\ z_i &= sinD_i \end{aligned}$$

Where,
-D_i is the dip angle of the pole of a plane i
-A_i is dip direction of the pole of a plane i
-x_i, y_i, z_i, are direction cosines of the pole of (normal vector to) i-th plane.

Since the pole of a discontinuity plane is a unit vector, formula [5] is always valid.

$$x_i^2 + y_i^2 + z_i^2 = 1 \qquad [5]$$

However, the dip direction and dip angle of a pole of a discontinuity plane are computed as:
Dip direction or trend of the normal =dip direction of the discontinuity plane ±180. This means that, if the dip direction is greater than 180^0, subtraction is applied, otherwise addition should be applied.
Dip angle (Plunge) of the normal = 90- dip angle of discontinuity plane.

4.4.1. Computation of resultant vector (R)

The resultant vector represents the mean direction of a sample N-unit vectors. The magnitude of the resultant vector, R is computed as the sum of all poles of discontinuities (normalized vectors) in the data set or a discontinuity cluster. The equation is given by:

$$R = \sqrt{\left(\sum_{i=1}^{N} x_i\right)^2 + \left(\sum_{i=1}^{N} y_i\right)^2 + \left(\sum_{i=1}^{N} z_i\right)^2} \qquad [6]$$

The normalized form of the resultant vector, R, is denoted by $\bar{R}$ and is given by equation [7]:

$$\bar{R} = \frac{R}{N} \qquad [7]$$

The projection of the resultant vector R to the horizontal XY-plane is denoted r and is given by equation [8]. Note that it is assumed that in the Cartesian coordinate system, the positive Y-axis represent the North, and the positive X-axis corresponds to East, and the Z-axis, represent the pole of the unit vector to a plane, is directed upward.

$$r = \sqrt{\left(\sum_{i=1}^{N} x_i\right)^2 + \left(\sum_{i=1}^{N} y_i\right)^2} \qquad [8]$$

Therefore, dip angle of the resultant vector, R, represent the dip angles of the N samples, and can be computed by equation [9]:

$$D_R = arccos \frac{\left|\sum_{i=1}^{N} z_i\right|}{R} \qquad [9]$$

The dip direction of the resultant R represents the mean dip directions of the N samples, and is defined by equation [10]:

$$A_{R'} = arccos \frac{\left|\sum_{i=1}^{N} y_i\right|}{r} \qquad [10]$$

However, the values of dip direction,$A_{R'}$ do not represent the actual dip direction, because the $A_{R'}$ values range from 0 to 90^0, but the actual dip direction of discontinuity planes falls between 0 and 360^0. Therefore, corrections must be made to obtain the actual dip direction, A_R of resultant vector R. To, determine the actual A_R, correction criteria can be applied depending on which quadrant $A_{R'}$ falls, and criteria is shown table 4-2 below as adopted from Priest (1993), Knapen & Slob (2006) and Slob et al. (2010).

Table 4-2: Criteria for determining the actual dip direction, A_R of the resultant vector R

Criteria 1	Criteria 2	Quadrant	Actual dip direction, A_R
$\sum_{i=1}^{N} x_i \geq 0$	$\sum_{i=1}^{N} y_i \geq 0$	I (between 0 and 90^0)	A_R=$A_{R'}$
	$\sum_{i=1}^{N} y_i < 0$	II (between 90^0 and 180^0)	A_R=180-$A_{R'}$
$\sum_{i=1}^{N} x_i < 0$	$\sum_{i=1}^{N} y_i < 0$	III (between 180^0 and 270^0)	A_R=180+$A_{R'}$
	$\sum_{i=1}^{N} y_i \geq 0$	IV (between 270^0 and 360^0)	A_R=360-$A_{R'}$

Nonetheless, the conversion from actual dip direction, A_R of resultant vector R to mean discontinuity plane orientation can be executed by:
Mean dip direction of a set of discontinuity planes = $A_R \pm 180$
Mean dip angle of a set of discontinuity planes= 90- D_R

4.4.2. Computation of Spherical variance

Spherical variance depicts the variance of 3D orientation data, in this case, discontinuity orientation. For closely clustered discontinuity poles (vectors) having a similar orientation, the spherical variance is close to zero, but for clusters showing high variability, the spherical variance gets close to 1. The concept of spherical variance was put forward by Davis (2002), and can be computed by equation [11] below:

$$S_s^2 = \frac{N-R}{N} = 1 - \bar{R} \qquad [11]$$

4.4.3. Computation of Fisher's constant K

The Fisher constant, K is a measure of how well a sampled set of a discontinuity cluster values represent a certain discontinuity set. Small values of K within the data represents large variation, whereas large values indicate a small variability. The Fisher's K, can also be computed according to equation [12]:

$$K=(N-2)/(N-R) \qquad [12]$$

Where K is the Fisher constant,
N is the number of sampled poles (vectors), and N≥10. For N less than 10, K value is not valid.
According to Davis (2002) cited in Slob et al. (2010), the K value is meaningful and more accurate if it is larger than 10. From equation [12], it can be deduced that pole vectors that show large dispersion generate a small resultant vector, R, thus the K value gets close to zero. In the contrary, pole vectors that have similar direction, and show small dispersion produce a large magnitude of R value resulting in very large K value.

4.5. UAV FLIGHT PLANNING AND DATA ACQUISITION

DJI Phantom 4 quadro-copter UAV equipped with built-in camera model FC330_3.6_4000x3000 is deployed to the field to capture images of the sub-vertical/vertical cliff of the rock face, outcropped in Romberg quarry, Gildehaus, Germany. Manual planning of image acquisition was executed to minimize occlusion, and avoid vegetation cover. The manual flight planning allows capturing of images with a very high overlap, which increased the visual content and reduced the effect of thin snow cover on the lower section of the slope. Basically, significant snow cover on the slope would have resulted in less texture and low visual content of the acquired images. It would result in low image contrast, and hence less key points would have been possible to extract for the image matching process. However, in this research project, the snow cover was very thin, and it was possible to washing away with rock salt, or removed it manually by shovel particularly from the lower section of the slope.

Prior to the image capturing with the UAV, ground control points were placed in the accessible part of the slope and away from the vertical rock face to reduce the effect of multipath from vertical rock face. The ground control points are measured to georeference the images captured by the UAV. They were placed well spread to reduce the error of propagation, which occurs due to the placement of ground control points either too close to each other or in a straight line. Eight ground control points, made of laminated paper of size 0.3 x 0.4 m^2, were measured using a Leica RTK differential GPS, of which the base station is located in Hengelo city. The tolerable accuracy of the GPS was set to be 5 cm. However, due to the effect of the multipath from the vertical rock face, it was difficult to obtain an accuracy of 5cm. The measured accuracy of the ground control points ranges from 5cm to 100cm. After setting up the ground control points, images acquisition followed using manual flight planning. In manual flight planning the person operating the UAV selects the interval of the image capturing, and determine the height and location of the UAV platform while flying the UAV to ensure maximum frontal and side overlaps between the images. The other advantage of the manual flight is that the operator can assess visually the quality of the images being captured on the screen. The optimal camera perspective selected for this project was the oblique view of 45 degrees that enabled to fully capture the images of the (sub-) vertical exposure face. Five hundred images were captured in about an hour by flying close to the rock face. The images were manually captured every 10 to 20 seconds. Subsequently, the images were downloaded from UAV memory, and a visual quality assessment was carried out in the lab. Highly blurred images were removed, thus 468 images were selected for the image processing.

4.6. UAV image processing

Version 3.1 of Pix4Dmapper (2017) desktop trial version was used to process the UAV images to generate the target point clouds. Pix4Dmapper is commercial photogrammetry software that uses images to generate point clouds, digital surface and terrain models, Orthomosaic, textural models, etc. It automatically converts images acquired by UAV, hand, or by plane and delivers highly precise, georeferenced 2D maps and 3D models. The software uses SfM and advanced dense image matching techniques (PMVS2), and it is quite reliable in generating dense point cloud generation (Gerke, 2014). It is has been used in numerous industries such as Surveying and mapping, construction, agriculture and real estate.

Three advanced processing options are available in Pix4Dmapper namely initial processing, point cloud and mesh generation, and Digital Surface Model, Orthomosaic and Index generation for mapping purposes. The initial processing of images entails image calibration and determining exterior orientation. That means, key points are extracted and then matched, and geolocations are optimized with ground control points.

Initial processing

Prior to starting the initial image processing, image properties were configured (Appendix D). These included selecting image coordinate system, setting image geolocation, and geolocation accuracy and camera model followed by setting up initial processing parameters. The initial processing option was set to 3D models incorporating the following parameters. Key points image scale was set to full, matching image pairs to free flight or terrestrial, and image matching strategy set to use geometrically verified matching, calibration method set to Standard, and rematch set to automatic.

Subsequently, the initial processing of the 468 images was performed and resulted in ray clouds of the rock face. Ray clouds are sets of rays that connect a particular 3D point to the center of the camera at each position the camera has taken an image. They allow annotating 3D points. They are used as tie points or ground control points. They mainly serve to refine the positions of camera centers or internal parameters of the camera. This refinement task is generally termed as bundle block adjustment (Pix4D, n.d.). The initial processing was carried out without ground control point information.

Ground control points for georeferencing

The ground control points (GCP) were imported to georeference the images. The georeferencing of images allow to make accurate measurements, provide scale and orientation to the project, reduce error accumulation, and enable faster processing during point cloud generation. The GCPs were registered with Netherland local coordinate system RD New and datum Amersfoort after the initial processing had been executed. That means they were added to the ray clouds to allow fast and precise point marking. Each GCP was marked on multiple images.

The imported GCPs were displayed on screen shifted by few meters from the target area. This is because of the low accuracy of the consumer grade camera on board of the UAV. By selecting the centers of each GCP markers located on the images containing particular GCP, it was possible to accurately locate all the GCP coordinate points on the center of markers on the image and ray clouds. This resulted in a reduced reprojection error (Kung, 2014). The reprojection error is the error between the consumers grade GPS onboard of the UAV and triangulated tie points using the accurate GCPs. However, the target area is a small rock exposure and using a clustered GCP collected from the small area may lead to more error propagation (Kung, 2014). Thus, to increase or improve the accuracy, five GCP were used for georeferencing. Optimization of the initial processing was done to accurately locate the ground control points and consequently reduce the reprojection error. Rough quality assessment of the initial processing based on quality report showed root mean square (RMS) error of 0.45m (Appendix C). The initial processing step was then followed by point cloud and mesh generation.

Point cloud and mesh generation

Point cloud densification parameters were configured prior to executing point cloud and mesh generation. The image scale was set to half image size and multiscale as the quality of the camera on board of UAV would suffice optimum point density generation. Full image scales are used if the camera onboard of the UAV are very sharp and high quality. In addition, using full image scale has no significant benefit when normal cameras are used to capture images, and it usually doesn't significantly improve results (Pix4D, n.d.). Furthermore, setting full image scale requires more RAM storage and takes high processing time. On the other hand, other parameters set include optimal point density, 3 minimum number of matches, and matching window size of 7x7 pixels were set up for point cloud densification.

Accordingly, 23.8 million dense point clouds were generated from the 468 calibrated UAV images (figure 4-3). The average ground sampling distance (GSD) of the project was 0.44cm/inch. The average density of the point clouds per one m^3 is 110813. The white colour on the ground in figure 4-3 and on some part of the rock face represent thin snow cover as the data was acquired during the winter season.

Figure 4-3: Visualization of dense 3D point clouds generated from UAV imageries and positions of five ground control points (GCPs). The inset is overview photo of the Romberg Quarry.

4.6.1. UAV point cloud filtering, subsampling, and cropping

Since the generated point clouds are big in memory size (and thus need more processing time and memory space) have areas covered with vegetation, and thin snow it is important to clip out (filter) the vegetation and other artifacts. To do this, the entire point cloud was imported and loaded to CloudCompare software (Girardeau-Montaut, 2017) for manual editing and subsampling. The point clouds that cover well-developed planar areas on the rock face (including the areas where sampling of traditional scanline and SSPC surveys were conducted), areas with minimum vegetation, and were selected manually. Later the point clouds were subsampled based on "spatial" method in the same platform by setting a minimum distance threshold of 5cm. The software then picks points from the original clouds such that no point in the subset cloud is closer to another point than the threshold distance. Subsampling reduces the number of point clouds to a manageable size and creates a subset of the original point clouds (figure 4-4). However, the original positions and color features of the points in the subsample remain the same, unlike resampling where the created cloud is not a subset of the original point cloud. Subsequently, the subsampled point clouds are cropped based on area of interest. Finally, a total of 439,560 point cloud data were exported as ASCII file for the segmentation process (figure 4-4). Slob & Hack, (2004) and Knapen & Slob, (2006) highly recommended crop selection of laser point clouds that cover areas on the rock face sampled by traditional techniques as it allows more reliable evaluation of the post processing results of the point clouds for the purpose of validation.

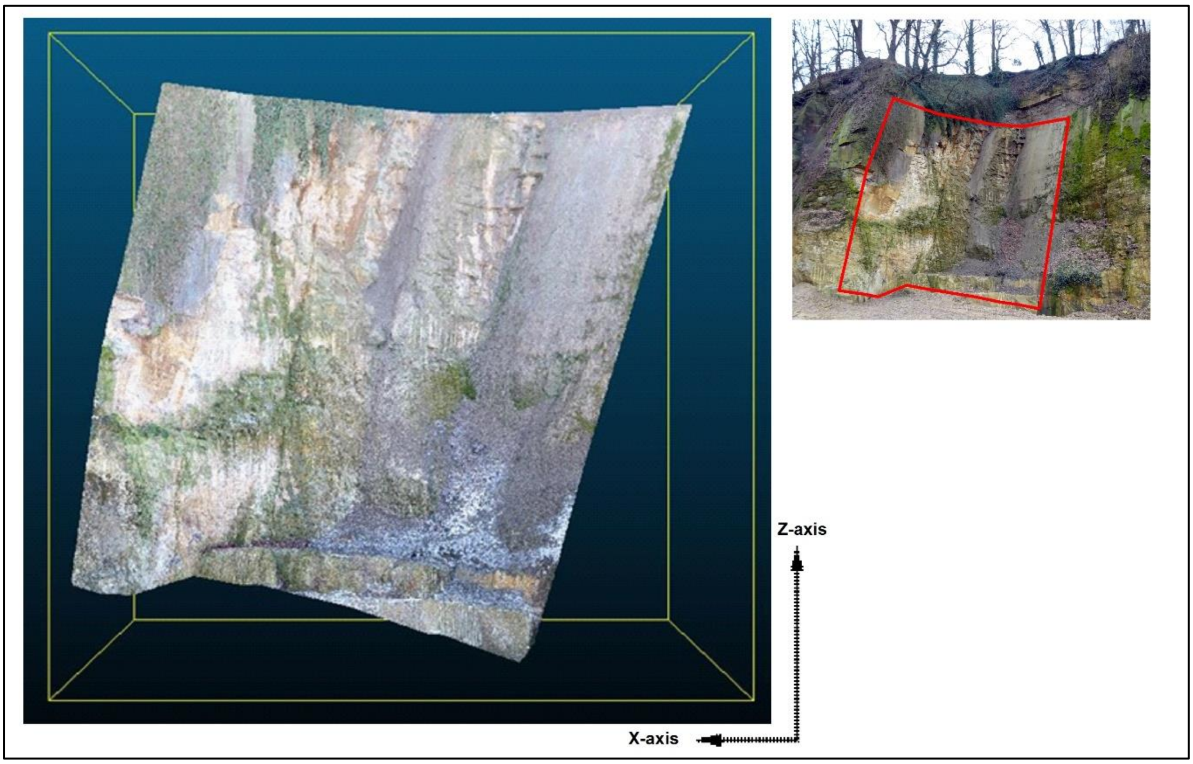

Figure 4-4: 3D view of subsampled and cropped UAV based point clouds prepared for segmentation. The inset photo illustrates the overview of the Romberg Quarry. The red rectangle is an approximate area where the main figure (cropped point cloud) is positioned.

4.7. Terrestrial Laser Scanner (TLS) data acquisition and Preprocessing

RIEGL VZ-400 Terrestrial Laser Scanner, which is a time-based scanner, was deployed to the field to acquire point cloud data sets. The instrument is V-line 3D scanner, a very compact and lightweight device with a 360^0 horizontal and 080^0 vertical field of view (Riegl, n.d.). It provides a fast scanning mechanism and non-contact data acquisition platform using a narrow infrared laser beam. The line scanning mechanism is based on a fast rotating multi-facet polygonal mirror that delivers fully linear, unidirectional and parallel scan lines. This allows acquisition of high accuracy and precision point clouds. It has integrated digital NIKON D600 camera that allows generation of colored and textured 3D point clouds.

Prior to the TLS survey, 3 optimum scan positions were selected with the aim to obtain maximum coverage of the target rock face to minimize blind spots and occlusion. Nine cylindrical tie points (reflectors) were placed evenly distributed both in vertical and horizontal directions. Tie points are retro-reflective targets that can be clearly seen in the amplitude of the scan data and used for tying or registering multiple scans. The tie points were set up visible to the scanner from the three scan standpoints. The operation started with creating a new project and scan position for data collection. The scanner's scanning pattern or resolution was configured to 4cm to ensure acquisition of optimum point cloud density. Accordingly, the first scanning survey was conducted from the left side (when facing the slope) and took 2 hours. The instrument automatically extracts the tie points and captures panorama images of the surrounding after the scan has finished. After completion of the first scan, the scanner was moved to the second standpoint to the right side of the target slope and a new scan position, the second, was created within the same project. Similarly, the third scan survey was conducted from the elevated location between the two previous scan positions. The project was finished and finally, the data were transferred to USB.

4.7.1. Data pre-processing

TLS data preprocessing was carried out using RISCAN PRO, which is an accompanying software package for the RIEGL LD Laser imaging scanners. It allows to perform various operations and tasks including sensor configuration, data acquisition, data visualization and manipulation and archiving. It is project oriented, which stores a project data in a folder containing subfolders of scan data, calibrated photographs, registration information, and processing deliverables (Riegl, n.d.).

RISCAN PRO version 2.1 was used to preprocess the TLS data set. A new project was created in RISCAN PRO and the TLS datasets acquired from the field were imported and converted using 'download and convert' wizard for registration. The first scan position was selected as reference scan as all the nine tie-points used were extracted from this scan position. The remaining two scans were registered to the first scan by finding corresponding tie-points. The second scan was registered or tied to the first scan by seven corresponding tie-points. The third scan was tied to the first and the second scans with nine corresponding points. This registration of scan positions was used to convert each Scanner's Own Coordinate System (SOCS) to Project Coordinate System (PRCS). In the field, each scan is collected with SOCS. So, is important to convert SOCS to PRCS to tie together multiple scans to obtain a coherent scene that can show multiple scanner data. The PRCS was later converted to Global Coordinate system (GLCS) using control points for the purpose of georeferencing the point clouds. The registration of multiple scan positions involves the conversion of SOCS to PRCS and is done by determining the respective Scanner's Orientation and Position (SOP) matrix. Therefore, the standard deviation of residuals, which shows the quality of registration, calculated for the second and third scan positions from SOP matrix are 0.0127m and 0.0097 respectively. Both values are acceptable as they are smaller than the 2cm standard set by RIEGL (Riegl, n.d.).

Later all the data from the three scans were displayed on the screen for visualization. Colour from images was applied to each scan to link the true color of each point cloud. The quality of the tie points, which serve as common points to tie each scan data into a project reference frame (PRCS), was evaluated by opening each scans Tie Point List (TPL) in 3D and visual assessment. Thus, one wrong tie point from the first scan and another from the third scan were found to have less superimposition and fit with the point clouds, and thus deleted from the TPL.

4.7.2. Georeferencing of point clouds and coarse registration

To link the point cloud data to the global coordinate system (GLCS), it is important to georeference the data. Georeferencing of the data converts the PRCS assigned when scan positions were registered to GLCS. The positions of six tie points and the three scan positions were measured by using Leica RTK differential GPS with an accuracy of less than 5cm. The positions of the remaining three tie-points were not measured due to the effect of multipath from the vertical rock face. Dutch RD New local coordinate system was used to collect the GPS data. Using RISCAN PRO, the GPS data were imported to TPL GLCS with the aforementioned coordinate system. Then, to georeference the point clouds, the control points and scan positions with GLCS were selected and copied to PRCS. Opening the TPL PRCS, and using 'find corresponding points' at each scan position, the scan positions were registered to the PRCS. Once the scan positions are registered to PRCS, they are linked to the registered GLCS, and therefore the data is tied to world coordinate system (Riegl, n.d.). Hereafter, the control points define the tie points. The process of geo-referencing the scan data using control points is also termed coarse registration of the scans. In addition, to calculate the orientation and position of each scan position and include it in the coarse registration, backsight coarse registration method was also executed on the three scans surveyed. Backsighting is a tool used to register multiple scan positions using well-defined coordinates of scanner positions and a remote object or a backsight for each scan, in this case, cylindrical tie point, measured by accurate DGPS. The control points and coordinates of each scan position used for georeferencing were also employed for backsighting.

4.7.3. Multi Station Adjustment (MSA)

Multi station adjustment is the final stage of scan registration process. The registration process merges all separate scans into a single point cloud. The coarse registration of the three scan datasets is performed using control points as tie points and backsighting techniques as discussed above. However, coarse registration of multiple scans doesn't finely or accurately merge the point clouds (figure 4-5a). Though tie points align very well, it is possible that other planar surfaces in the point cloud might show alignment errors. This is attributed to an unstable reflector set up or non-optimal reflector placement or measurement errors (Riegl, n.d.). Therefore, to minimize these errors and improve the alignment of the point cloud data fine registration of multiple scan positions is indispensable.

RISCAN PRO has a plugin function termed ''Multi Station Adjustment'' (MSA), which serve to automatically modify the orientation and position of each scan in several iterations in order to determine the best overall fit plane. This is done by automatic searching and determining the corresponding points using iterative closest points algorithm (ICP). The ICP detects iteratively the correspondence between different point clouds from different scans on a point-to-point basis using the minimum Euclidean distance (Besl & Mckay, 1992). The MSA employs filtered versions of each scan to execute surface matching registration process. A plane filter is used to distinguish and triangulate planar surfaces in each scan, followed by identifying common planar surfaces from each scan and shifts each scan data until the best match is obtained. To carry out the MSA, sample polydata was created from each scan by reducing the point clouds to speed up the processing. To do so, the target area was selected from the combined point clouds of the three scans and prepared for adjustment. Plane patch filter was selected and used in the setting during the creation of polydata. The plane patch filter searches for planar areas or patches in the point cloud based on the following steps:

- Divide the point clouds into equal sized cubes of some size.
- For each cube created it estimates the best-fit plane within the points inside the cube based on least-squares method.
- If the standard deviation of the normal distances between the plane and the points is found to be less than the maximum plane error, then the plane is fit to be added to the resulting list of plane patches,
- Otherwise, the points in the cube are further divided into eight smaller cubes, each having the size of the half edge length of the main cube, and for each smaller cube the plane estimation steps above are applied. This procedure is repeated with again dividing the new cube in smaller cubes again with the half-edge length of the forgoing step.
- The iteration is stopped either when a best-fit plane is found or the number of point clouds inside the cube is less than the minimum number of points per plane or the cube size falls below the minimum search cube size.

The plane patch filter settings that were used to create planes from overlapping scans include maximum plane error, which was set to 0.006m, minimum number of points per plane was 10 as the point clouds were dense, a minimum search cube size of 0.256m, and maximum search cube size of 20.048m as recommended by Kennedy (2013). After determining the settings, the three scan positions were locked, and the measured scan positions with GLCS and the polydata objects previously created were used as input data for adjustment. Finally, based on the nearest point search and adjustment parameters outlined in table 4-3 below, three iterations were executed to run the MSA.

Table 4-3: adjustment parameters of each iteration used to run the MSA

Parameter	First iteration	Second iteration	Third iteration
Search radius (m)	5	2	2
Min. change of error 1(m)	0.1	0.02	0.008
Min. change of error 2(m)	0.002	0.006	0.003
Outlier threshold	2	2	1
Statistics			
Standard deviation (m)	1.3234	0.1859	0.1027

After the calculation of the three iterations of the MSA, the results revealed fine alignment of the point clouds from the three scan positions (figure 4-5b). The spread of errors for matching surfaces as depicted by a number of matching planes in histogram revealed the normal distribution of overlapping planes with values close to zero, which was a desirable result. From the statistics of the number of polydata observations used in the calculation, it was observed that the standard deviation dropped from 1.30234m for the first iteration to 0.1027m for the third iteration. The final standard deviation was found to be less than 0.2m, and it is a desirable result according to Riegl (n.d.). The successful running of the MSA ended the scan registration processes.

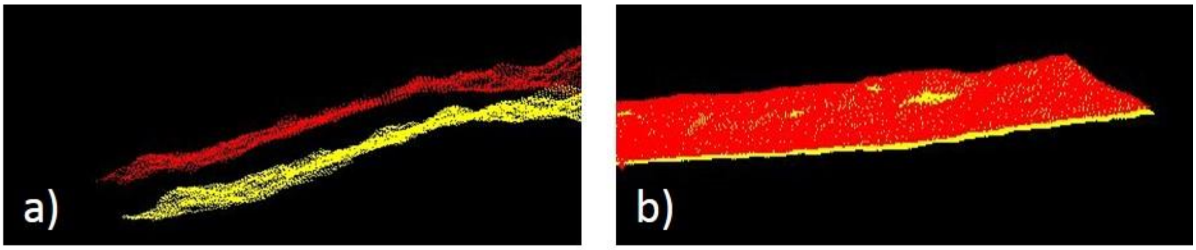

Figure 4-5: a) Sections of point clouds of scan 2 (yellow slice) and scan 3 (red slice) illustrating inaccurate alignment after coarse registration b) fine alignment after the third iteration of Multi-Station Adjustment (MSA).

4.7.4. Data filtering and importation in Riscan Pro

After fine registration of the raw point cloud data with MSA, data filtering and cleaning were executed. First, the study area of Romberg quarry rock face was manually selected and cropped out from the whole point cloud data set for filtering purpose since scanning with TLS were carried out with 360^0 field of view (figure 4-6). Filtering of the point cloud data was done to remove areas of dense data near the scanner positions, and areas covered with vegetation, snow, and other unwanted artifacts. Therefore, more evenly distributed manageable data are often created after filtering.

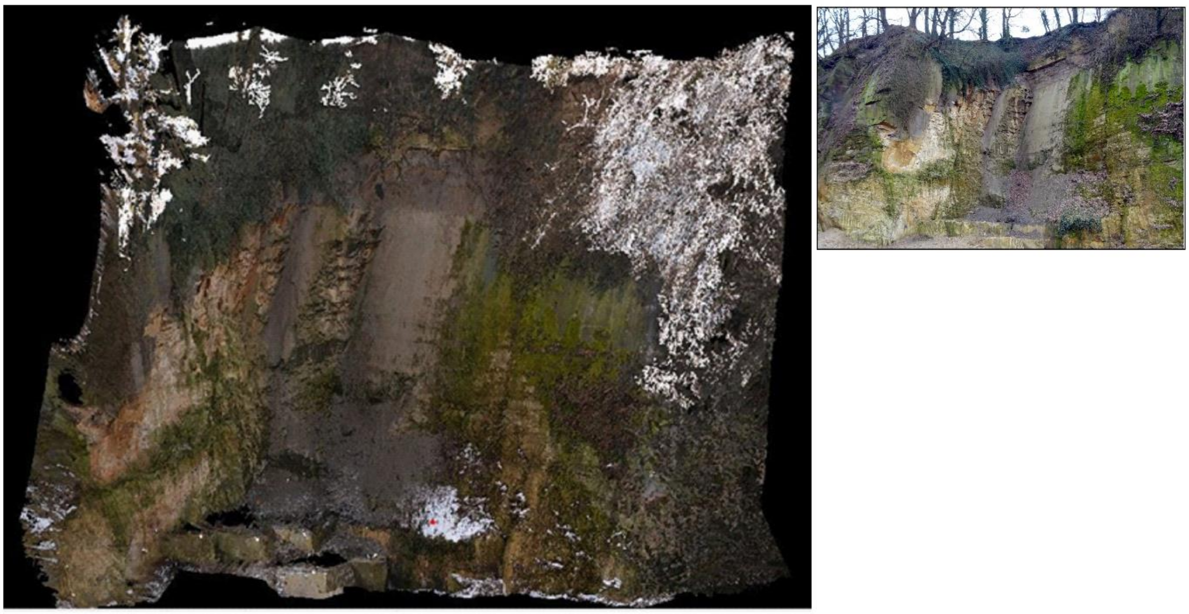

Figure 4-6: Visualization of dense and textured 3D TLS point clouds of the Romberg quarry. The cropped cloud contains 28 million points. The white colour on the trees and the slope represents thin snow cover as scanning was made during the winter season. The black areas at the base of the main figure is no data area due to occlusion. The inset photo shows an overview of the Romberg Quarry at the study location.

Rigel Riscan pro provides both automated and manual tools for filtering and cleaning point cloud data set. However, in this research, the manual filtering and cleaning methods were optimum tools because automated filtering of vegetation on the rock face resulted in the deletion of the whole data where vegetation was present. Thus, vegetation and other noises were manually removed without affecting the original data. After manually filtering and cleaning the point cloud data set from each scan position, the equivalent area of interest to the UAV-based point clouds was selected as a polydata in Riscan pro (figure 4-6). The polydata that contained clouds of 11.2 million points were then exported as ASCII delimited format. The exported poly data contained x, y, z coordinates with the global coordinate system, intensity, and colour information. Later the selected point clouds were imported and loaded to CloudCompare software for subsampling. After subsampling, a total of 440,831 point cloud data were exported as ASCII file for the segmentation process (figure 4-7).

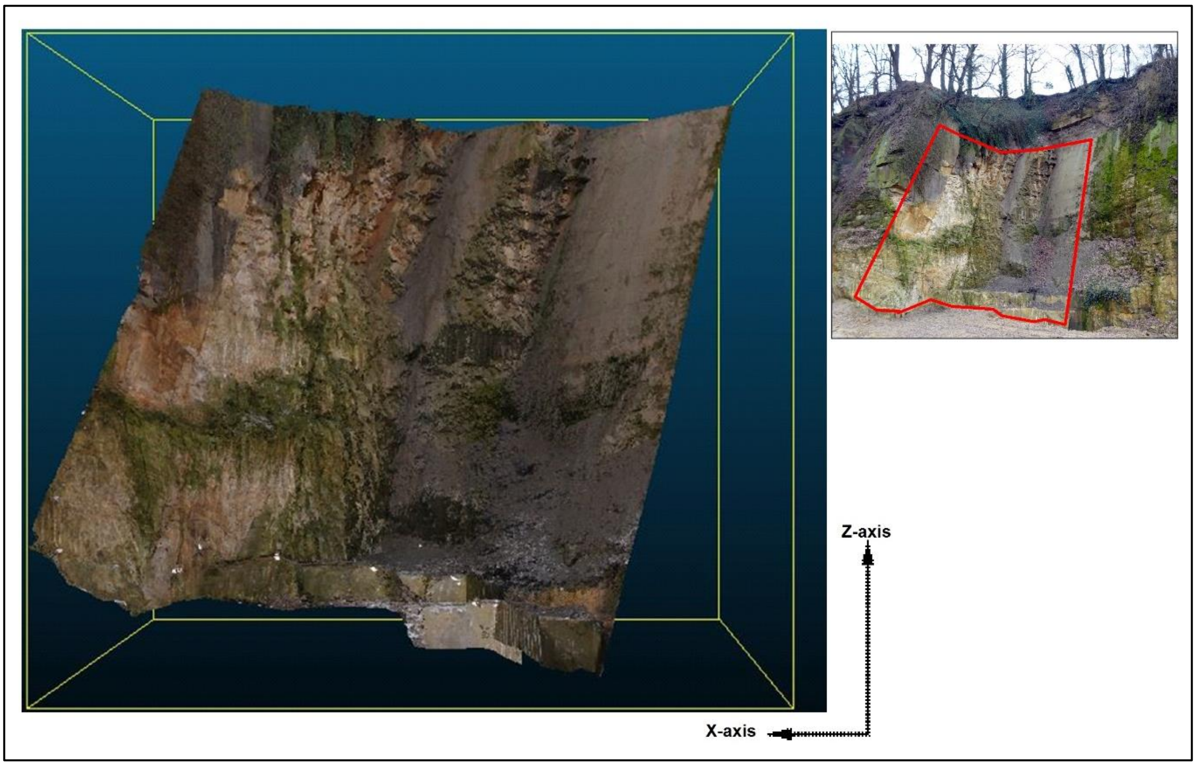

Figure 4-7: 3D view of subsampled and cropped TLS point cloud prepared for a segmentation process. The inset photo illustrates the overview of the Romberg Quarry. The red rectangle is an approximate area where the main figure (cropped point cloud) is positioned.

4.8. Point cloud segmentation based on Hough transformation and Least-Squares Analysis

In this segmentation process, the 3D Hough transformation is applied to identify and select an optimal number of seed points from the point cloud data to form a planar element, whereas least square regression is used to evaluate their planarity. If the selected points define a planar surface within a given tolerance, then a seed surface or plane is grown step by step based on spatial search ensued by optimization of the new plane by least square estimation. Vosselman et al. (2004) carried out segmentation based on Hough transformation and Least squares in the software Point Cloud Mapper (PCM), a software developed for research and educational purposes in ITC and TU Delft to process airborne laser scanner data. However, the software can also be implemented equally well on point clouds generated by terrestrial laser scanners and photogrammetry (Slob et al., 2010). The PCM software applies the principle of region or plane growing and the data can be structured using K-D tree structure. General processing procedures outlined by Vosselman et al. (2004) and Rabbani et al. (2006) are followed to implement the methodology in PCM software. However, it is required in PCM to specify optimal parameters and distance thresholds that control the process of segmentation. The input parameters and distance thresholds to control the segmentation processing steps are discussed in the following section.

Data importation and structuring: in order to start the segmentation process, registered and georeferenced point clouds derived from TLS survey and from UAV imageries were imported separately to PCM software as comma-delimited ASCII format that contains x, y, z values of each point cloud. The PCM also allows importing the RGB and intensity values of each point cloud if necessary.

The segmentation analysis entails sequential analysis of all the points within the point cloud, and their classification pursuant to which individual planar elements they belong to. In the classification process, each point is given a label, which is stored as a point attribute. At the beginning, all the points are given label 0.

After recursive segmentation and evaluation process, all points are given a label point ranging from 1 to the maximum number of planes that are created.

Since the segmentation process is recursive, it is important to accelerate the search for the nearest neighboring points by structuring the unorganized point cloud data prior to segmentation. The PCM software offers three options (as storage models) for structuring point cloud data. These include K-D tree, Delaunay TIN, and Octree. K-D tree partitioning was chosen for this research as it is the optimum structuring method for segmenting TLS or photogrammetry-derived point clouds. The Delaunay TIN is not recommended for noisy and unorganized point cloud data, and Octree method contains a cell with an unbalanced number of points. The parameters of K-D tree structuring applied in PCM is shown in table 4-4.

Definition of connected component parameters: two parameters are defined here to ensure the density of points during each seed selection process and after each plane-growing step. Areas that contain sparse points or noisy data are thus omitted from processing.

-Maximum distance between points: represents the neighborhood area around a given point, but not applied with segmentation into planar surfaces.

-Minimum number of points: determine a neighborhood area around a given point. It depends on the size of scanned rock outcrop and the resolution of the point cloud data. Defining an appropriate threshold value of this parameter determines the size of planes that are identified for use in the subsequent processing. Small planes that don't satisfy the threshold will be removed.

Seed selection parameters: this defines how the seed points are selected from all the candidate or potential points present in the Hough space. The important parameters of seed selection include:

-Minimum number of seed points: defines a minimum number of points that should be close to the plane found by Hough transform to ensure if the neighborhood is planar. If the number of seed points is few, they do not form a planar area and the process is abandoned. A minimum of ten seed points is found to be acceptable threshold value to allow proper plane growth.

-Maximum distance to plane: defines the selection of seed points that are only within a specified perpendicular distance from the found plane. This avoids the addition of noisy points to the seed points. The optimum distance depends on the precision of the data. All points within the precision are optimum seed points. The threshold value should be fewer than the bin size distance, but higher or equal to the precision. If the value of the maximum distance to the plane is too small, a large portion of the point cloud data will not be segmented.

Hough transform parameters: the following parameters determine the 3-D Hough transformation:

-Maximum slope angle: this parameter allows to ignore vertical planes. If all slope angles are to be included, the maximum angle should be set 90^0.

-Bin size slope angle: specifies the size in which the angle of parameters in Hough transform are discretized and determines if the seed points are coplanar or not.

-Bin size distance: It splits the distance parameter axis in Hough transform into equal bins.

Surface growing parameters: once a seed surface is obtained, the growing stage is searching for adjacent points in the same plane. These parameters determine the growing or expansion of those seed surfaces towards neighboring points that belong to the same planar region or surface. The following parameters are important:

-Surface growing neighborhood definition: two options are available: direct neighbors or all within the radius. The surface growing neighbourhood defines the formation of a new (potential) planes by choosing points around previously classified points based on a minimum number of direct neighbors or by defining a specific search radius.

-Surface growing radius: specifies the search radius around the seed points. It defines the size and kind of the neighborhood along with the parameter "surface growing neighborhood definition."
-Maximum distance to surface: specifies when a point is considered to belong to a plane at growing stage. If this value is set to a large threshold, it results in under segmentation; and if too small value is chosen, it will produce over segmented point clouds. Thus, the optimum value should be slightly larger than the value used in "maximum distance to plane" in the seed selection parameter.
-Competing surfaces: surface growing in segmentation process is a greedy procedure. The surface growing process assigns all points to a plane if the distance of the points to the plane is below a given threshold. When the next seed is grown, points that belong to a previously grown surface are examined if this parameter is enabled. This means that enabling/checking the competing surface parameter allows the points to be assigned to a plane where they fit best.
Therefore, the thresholds of the segmentation parameters used in this research for both UAV and TLS points clouds are shown in table 4-4.

Table 4-4: Threshold of segmentation parameters used for segmenting both UAV-based and TLS point clouds in PCM software.

Neighbourhood definition	
Storage model	K-D tree
Octree bin maximum number of points	100
Octree bin overlap	1
Distance metric	3D
Number of neighbors in K-D tree	100
Connected component parameter	
Maximum distance between points (m)	0.5
Minimum number of points	100
Seed selection parameters	
Seed neighborhood definition	Direct neighbours
Maximum slope angle (degrees)	90
Bin size slope angle (degrees)	3
Bin size distance (m)	0.1
Minimum number of seed points	10
Maximum distance to plane	0.1
Surface growing parameters	
Surface model	Planar
Surface growing neighborhood definition	Direct neighbours
Maximum distance to surface (m)	0.1
Maximum distance to recomputed local plane (m)	0.15
Competing surfaces	Enabled/yes

After repetitive processes, it was found that the optimum segmentation process with PCM software is very sensitive to a minimum number of seed points and maximum distance to plane in the seed selection stage, and maximum distance to surface and competing surfaces in the surface growing phase.

4.8.1. Results of segmentation process of TLS point clouds

The input point cloud data set consisted 441,085 points. After segmentation process, 440,831 points were segmented, while 1340 points remained unsegmented. The unsegmented points consisted of noise or low data density areas that didn't satisfy the segmentation parameters outlined in table 4-4. The result showed more than 99% of the points were segmented. The point clouds were segmented into 223 discontinuity planar surfaces. The segmentation results of TLS point clouds is shown in appendix E. Points that fall within a single segmented discontinuity plane received similar colour.

4.8.2. Results of segmentation process of UAV point clouds

The input point cloud data set consisted 438,630 points. After segmentation process, 437,290 points were segmented, while 154 points remained unsegmented. The unsegmented points consisted of noise or low data density areas that didn't satisfy the segmentation parameters outlined in table 4-4. The result showed more than 99% of the points were segmented. In total 337 discontinuity planes were identified from segmented point clouds. Figure 4-8 shows segmented UAV based point clouds. Points that fall in a single segmented discontinuity plane received similar colour.

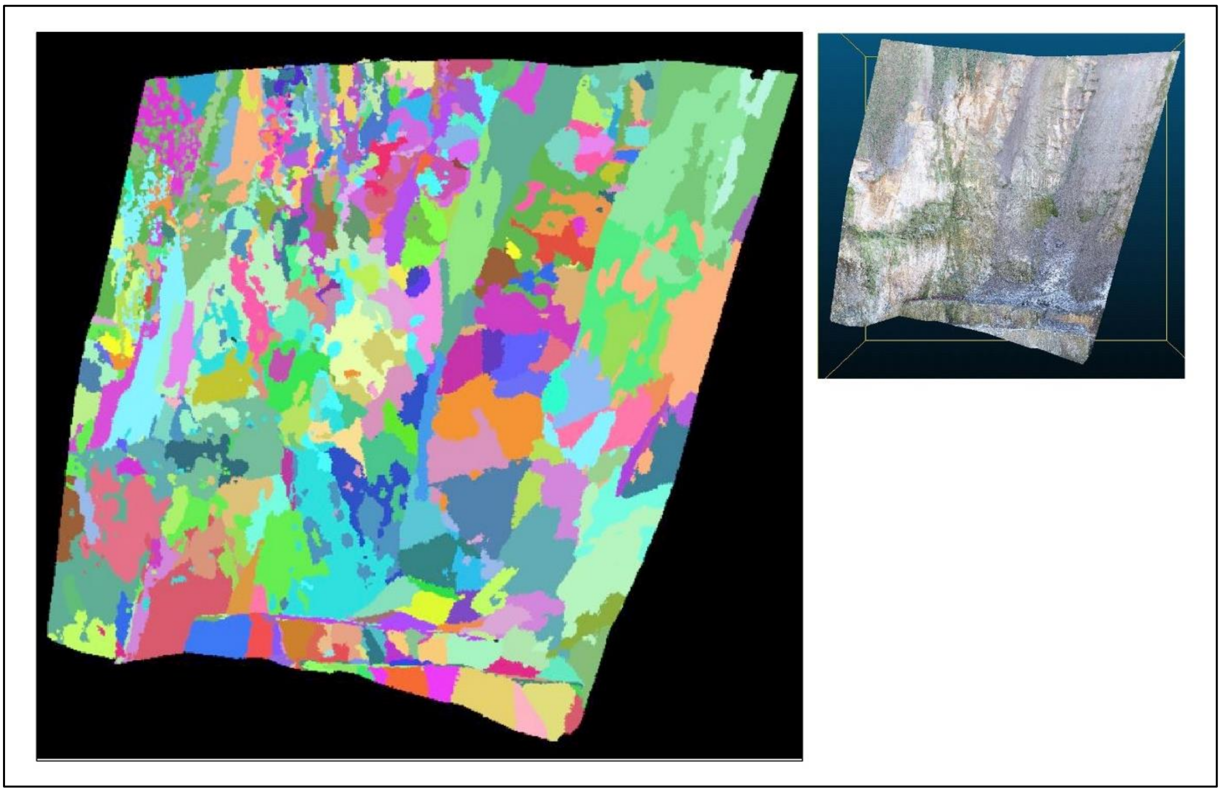

Figure 4-8: Direct segmentation results of UAV based point clouds into distinct discontinuity surfaces carried out via Hough transform and Least squares method in Point Cloud Mapper (PCM) software. The inset photo illustrates the input point cloud for the segmentation.

Visual assessment of figure 4-8 shows segmentation of rock faces partly covered with vegetation (top left corner) resulted in a smaller segments.

After segmentation of the point clouds, small segments that consisted of less than 200 points were removed from the data. Then, the data were exported as ASCII format for subsequent derivation of discontinuity information using Matlab environment. The exported data contained four coordinates x, y, z, and segmentation label, which shows the plane number the points belong. Deriving discontinuity information from segmented point clouds

Segmentation, which recognizes the point clouds that belong to the same planar face and hence assigns the same segment number, is the first step to derive discontinuity information from point clouds. Therefore, it is imperative to further analyze the segmented point clouds in order to extract discontinuity information such as orientation (dip direction and dip angle), plane equations, and the centroid coordinates for each individual discontinuity surfaces.

4.8.3. Fuzzy K-means clustering of discontinuity data

Fuzzy k-means clustering can be applied to cluster large amount of discontinuity data, which may be highly dispersed or noisy, into distinct sets (Harrison, 1992; Slob et al., 2005). Fuzzy K-means clustering technique (a.k.a. fuzzy c-means clustering) categorize each discontinuity orientation (or their poles) to a pre-determined number of clusters or sets (k). The number of clusters, k, can be determined in many ways. One way is to use trial and error, which involves guessing the initial k, and assessing and verifying the number of clusters visually. The process can be repeated with different k values until satisfactory results are obtained. Secondly, k can be determined in an automated way by using fuzzy validity indices. Therefore, fuzzy K-means clustering allows automated clustering of orientation data after the user has determined the number of sets. It is a fuzzy or soft partitional clustering technique as it divides the data sets into subsets pursuant to the degree of membership grade assigned to each set. The degree of membership range between values zero to one. The lesser the certainty that a pole belongs to a particular set, the closer its membership grade value to zero and vice versa.

The fuzzy k means algorithm assumes the pole dispersion is non-uniform and symmetrical about the mean orientation of each discontinuity cluster, thus exhibiting a Fisher's distribution (section 4.4). However, it can also be applied to classify non-circular clusters (e.g. Bingham, section 4.4) that are distinct and equally distributed to each other.

In this research Fuzzy k-means clustering is applied for clustering discontinuities generated from point clouds according to procedures outlined in Bezdek, (1981) and more institutively described in Slob et al., (2005; 2010).

4.8.4. Processing steps of derivation of discontinuity information from segmented point clouds

The derivation of discontinuity information from segmented point clouds was carried out in Matlab. Segmented point clouds in ASCII format containing coordinates x, y, z and segment number of each point data were imported to Matlab (Math works Inc, 2017). For this research Matlab scripts written by Knapen & Slob (2006) and Slob et al. (2007) were adopted and implemented to derive the necessary discontinuity information according to the following steps:

a. Identifying the normal vector (poles) of each discontinuity plane using principal component analysis. Thus, the orientation of the poles determines the orientation of the individual planes.
b. Plotting of the normal (poles) on a stereographic projection to assess their concentration. This step is followed by grouping of individual poles to determine the appropriate number of distinct discontinuity sets/clusters by using Fuzzy k-means clustering technique.
c. Computing plane parameters of each pole to the plane namely a, b, c, of the plane equation ($ax + by + cz + d = 0$) within the sets. This permits calculation of spatial statistics namely mean orientation, Fisher's K value, spherical variance, and the normalized resultant vector, R for each identified discontinuity cluster.

d. Defining the plane parameter d, which is the perpendicular distance from the plane to the origin of the point cloud coordinates, of each plane by replacing the mean coordinate into the plane equation. The parameter d is computed to determine the normal set spacing.

4.8.5. Computation of normal set spacing

The execution of the above processing steps results in the identification of individual discontinuity planes and their sets, plane parameters (a, b, c, and d; see section 4.3), and outputs of the spherical statistics. The plane parameter d is used to calculate normal set spacing and subsequent set spacing statistics for each cluster.

Two methods were developed by Knapen & Slob (2006) and Slob et al. (2007) for computing normal set spacing of discontinuities derived from point clouds. The first method uses virtual scanline, an imaginary line oriented parallel to the mean orientation of each discontinuity set as adapted from the conventional method of determining normal set spacing using scanline as defined by Priest (1993) (section 2.2.1 and section 4.2). However, this method is constrained by the choice of the position of the virtual scanline and, thus produce different spacing results for varied placement of the virtual scan line in the 3D space of point clouds. Furthermore, using this method incur problem when numerous small planes that belong to a single discontinuity plane are projected. This results in unrealistic multiple small spacing values.

The second method calculates the "equivalent" normal set spacing. It applies the plane distance parameter, d, in the plane equation (equation 1), of individual discontinuities within a discontinuity set obtained according to the steps outlined in section 4.9.2. Since the distance parameter d represents the perpendicular distance of a plane to the origin of the point cloud coordinates, if sorted in an ascending or descending order, the difference between adjacent values defines the spacing between discontinuities. However, the distance parameter, d, depends on the position of the origin, which is normally located in the center of the whole point cloud. The ideal position of the origin, in this case, is to relocate it to the center of all the discontinuity planes that belongs to the same set. This method derives discontinuity spacing values closest to the traditional scanline normal set spacing values computed according to Priest (1993). The second method shows more advantage than the first because its calculation is intuitive as it only requires calculating the plane parameter d based on a new position of the origin, i. e the center of all the discontinuity planes that belongs to the same set, and subtracting subsequent values to obtain the normal spacing of the discontinuities. In this research, the equivalent normal set spacing of discontinuities derived from the two point cloud sources (TLS and UAV-based) were computed using the second method described above.

Instruments, and processing and analysis software used in this research are listed in appendix D.

5. RESULTS AND DISCUSSION

5.1. Conventional rock mass characterization and discontinuity field data acquisition

The main aim of conventional discontinuity characterization was to generate data that can be utilized for comparison and validation of the two remote sensing techniques namely TLS and UAV photogrammetry. In accordance with this aim, field rock mass description of Romberg sandstone quarry exposure was carried out following internationally accepted and well-established standards such as British standard (BS 5930:, 1999), standards of the international standard organization (ISO 14689-1, 2003), and International Society for Rock Mechanics (ISRM, 1978). Furthermore, the rock masses were assessed and characterized in detail for classification into different geotechnical units using "A new Approach to Rock Slope Stability-a Probability Classification (SSPC)" method (Hack et al., 2003).

5.1.1. Geotechnical units

The principal criteria for systematic description and classification of the rock masses into different geotechnical units include the degree of weathering, strength properties, compositional variation, and discontinuity characteristics. Thus, based on the SSPC system, the rock mass of Romberg sandstone quarry of interest area was divided into five geotechnical units (figure 5-1). Variation of geotechnical units in the rock masses is noticeable vertically from top to down. The noticeable variations are the degree of weathering and discontinuity spacing. The detailed description of each geotechnical unit is given below. Note that the layers are dipping in a roughly Southern direction at the study location, but the whole series of layers plunges to the West. More to the West in the Romberg Quarry, the top layers come to the bottom of the quarry. Layers that are inaccessible at the location of the study area can be studied in the West of the quarry. Visually the layers do not seem to change in this direction.

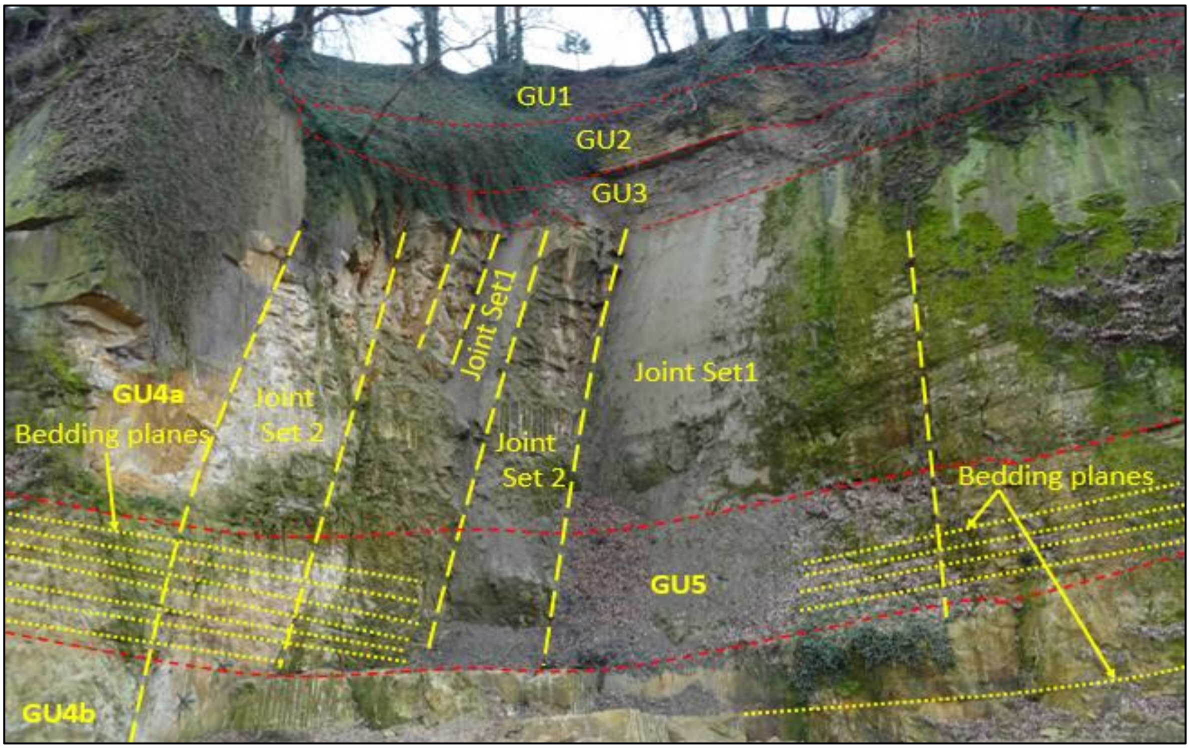

Figure 5-1: Romberg Sandstone quarry slope classified into different geotechnical units. 'GU' denotes the geotechnical units. The red broken lines separate the geotechnical units, yellow wide broken lines separate most prominent and easily recognizable joint sets, and yellow dotted lines represent the bedding planes.

1. Geotechnical unit 1 (GU1): this unit covers the topmost layer of the rock mass having a thickness of 1 to 1.5m. As being on the top of the exposure studied it is located in an inaccessible vertical slope. From remote visual assessment, and observation of the extension of the top layer further down to the west side to the active quarry area it consists of reddish, medium to coarse grained, completely weathered sandy residual topsoil. This unit is characterized by oxidation and supports bushes and trees.
2. Geotechnical unit 2(GU2): found lying directly below the GU1 layer. It seemingly comprises highly weathered and thinly bedded sandstone layer. Its thickness is about 1.5m. Visually, this layer extends to the West of the Quarry, but not described in detail due to ongoing excavation activity during the field work.
3. Geotechnical Unit 3 (GU3): This unit is compositionally different from overlying and underlying sandstone units. It is thinly bedded and has a thickness of about 2.5m. This unit is being eroded and accumulated down on the lower section of the slope due to weathering probably caused by percolation and surface run-off water. From the fallen debris, it was observed that this unit consists of grey to brownish, fine-grained, soft, and plastic clayey material. It is probably a local channel fill as the unit pinches out and doesn't continue to the west side of the quarry. Erosion of this fine-grained clay material and deposition of the particles on the underlying units has produced a staining effect on the geotechnical units underlying it. The surface staining effect of this unit has rendered the underlying unit brownish and smooth superficially.
4. Geotechnical unit 4 (GU4a): This unit is mainly characterized by reddish to greyish, fresh to slightly weathered, and thickly bedded to massive sandstone. The slightly weathered parts of the GU4 slope is superficially covered with green mosses and lichens. This biotic influences can induce physical as well as chemical weathering activities on or near the surface of the rock face (Hack & Price, 1996). The fresh parts are devoid of vegetation. From visual assessment, two dominant joint sets occur in this unit. The spacing of the joints can be estimated to range between 1 and 6m with high persistence along strike and dip. The thickness of this geotechnical unit can be estimated to be 8 to 10m. This unit is partly overlain by GU3 unit. In the areas or horizons that lie under the GU3 unit, the original surficial colour of the GU4 layer is changed to brownish to grey due to surface staining as a result of weathering and subsequent erosion of the overlying GU3 layer. This unit had been quarried for dimension stone that serves different purposes as noted from remnants of drilling activities carried out in the past. However, this unit also shows areas of closely spaced but more-or-less randomly fractured discontinuities that exhibits curved or chonchoidal fracturing, which is an indication of jack row hydraulic hammering. It is assumed that these fractures do not penetrate deep. This subunit is classified as a different geotechnical unit, GU6 as shown in figure 5-2. Another geotechnical unit GU7 is defined within the GU4a unit as this is a part of the unit with extensive local fracturing (figure 5-2). Fallen debris or spalling materials of leaves and clayey material from GU3 unit are deposited on the GU4b unit.
5. Geotechnical unit 4 (GU4b): This unit is similar to the GU4a unit, but comprises the accessible bottom part of the slope. The conventional geological slope characterization activities were conducted for this unit. It is characterized by widely spaced jointing and thick-spaced bedding planes. This unit has been mined for dimension stone.
6. Geotechnical unit 5 (GU5): This unit is sandwiched between the GU4a and GU4b layers. It is characterized by reddish to creamy colour, and coarse-grained sandstone. Its difference with the overlying and underlying GU4 units lies in the density of the spacing of the bedding planes and joint planes. The normal spacing of bedding planes in this geotechnical unit ranges from thin to very thin as measured by scanline method. The normal spacing of the bedding planes in this unit

ranges from 0.6cm to 0.6m. Seemingly, the small spacing of joints and bedding planes have rendered this unit unsuitable for dimension stone, as no signs of exploitation of this unit is found on the rock face. Fallen debris or spalling materials of leaves and clayey material from GU3 unit are also deposited on the GU5 unit.

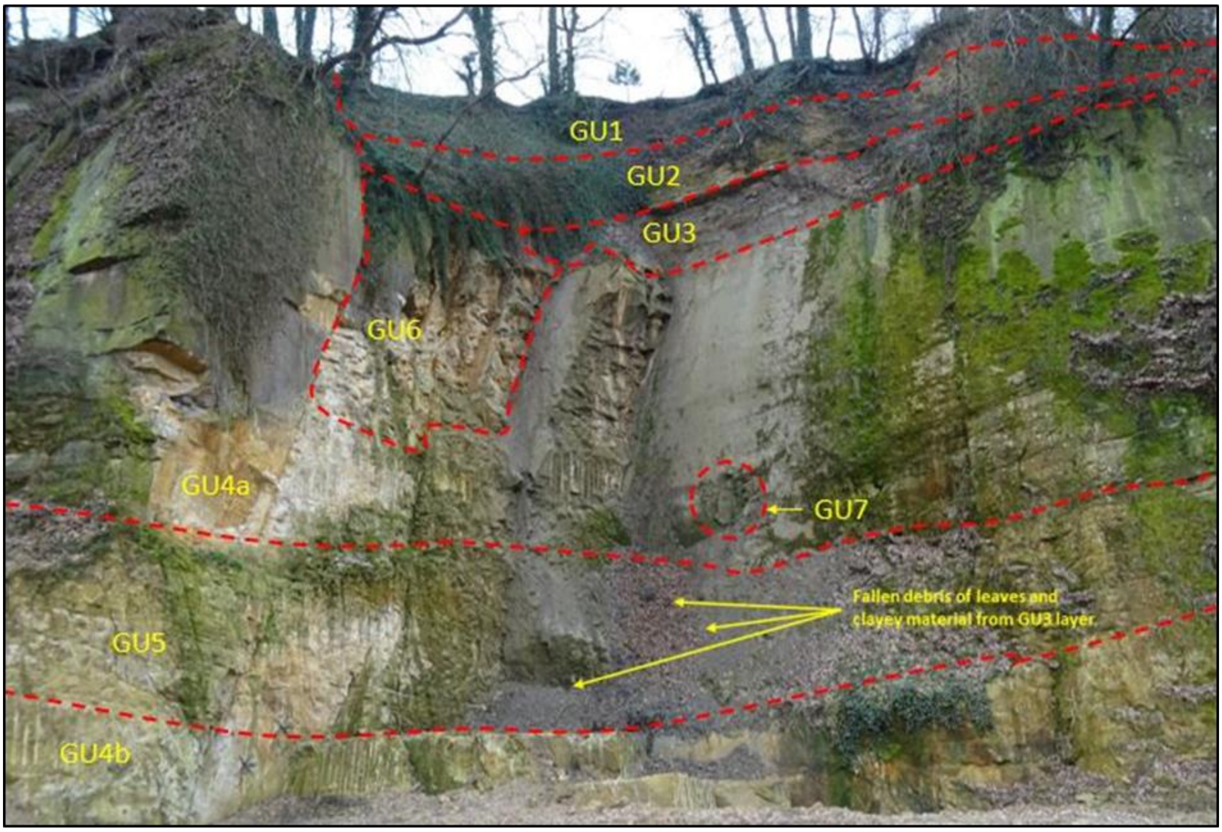

Figure 5-2: More detailed geotechnical units of Romberg Sandstone quarry outcrop considering surficial joint parameters.

5.1.2. Discontinuity characterization using Slope Stability Probability Classification (SSPC)

The SSPC characterization of Romberg Quarry in the GU4b unit resulted in the identification of four discontinuity sets in the field as shown in figure 5-3. In addition, extra discontinuity data measured from individual discontinuity planes were also added to the SSPC data for computing spherical statistics. Summary of statistics of SSPC surveys executed is presented in table 5-1.

Table 5-1: Summary of spherical statistics of identified and characterized discontinuity sets in the Romberg sandstone quarry outcrop using SSPC method. Remark: the value of Fisher's K is not included in the table since the number of observations, N, are less than 10 for all the sets.

	Set 1	**Set 2**	**Set 3**	**Set 4**
Geologic origin	Bedding plane	Joint	Joint	Joint
Mean dip direction (degrees)	211.57	29.47	312.68	289.2
Mean dip angle (degrees)	24.42	66.98	66.65	85
Number of Observation N	3	7	3	5
Resultant R	2.99	6.85	3	4.9
Spherical Variance	0.01	0.02	0.01	0.01
Mean normal set spacing (m)	1.433	1.6	1.367	2.2
Stand. Dev. NS. Spacing	0.513	0.9	0.38	1.41

Maximum Normal set spacing (m)	1.3	2.4	1.8	3.2

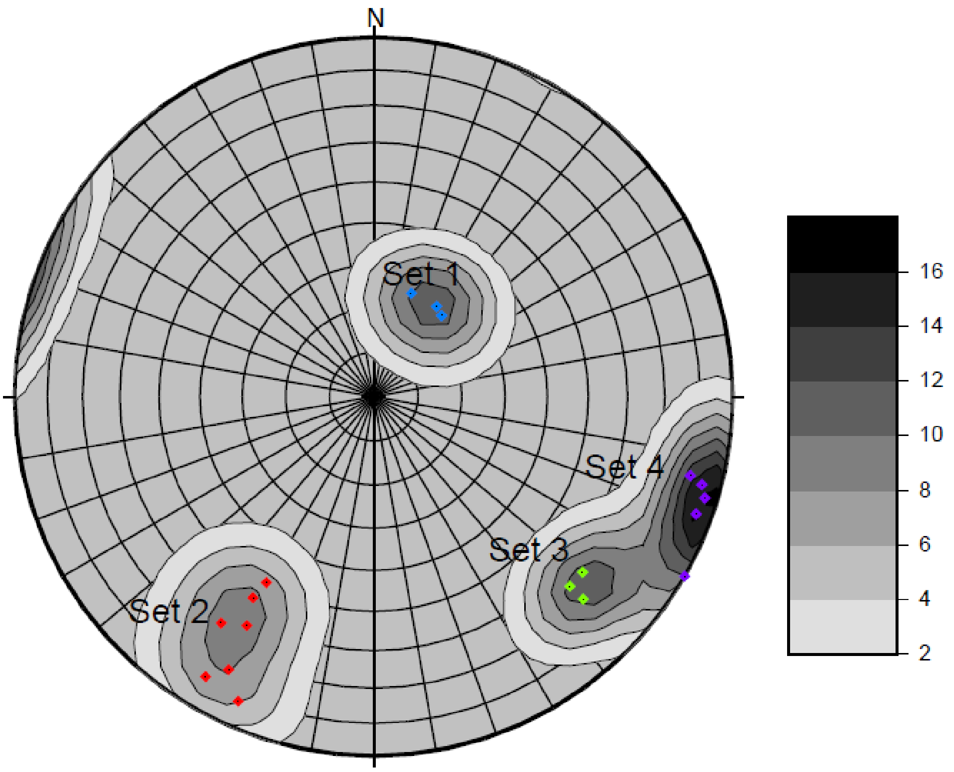

Figure 5-3: Equal area, lower hemisphere grey scale stereo density plot of poles of discontinuity sets mapped using SSPC method. Counting method applied: Fisher distribution. Software: OSXStreonet (Cardozo & Allmendinger, 2013).

5.1.3. Condition of discontinuities in Romberg Sandstone quarry

The condition of discontinuities in discontinuous rock mass principally include material friction, roughness (both large and small scales), discontinuity wall strength, and infill material. These parameters of a discontinuity determine the shear and tensile strength of a rock mass (Bieniawski, 1989). In the geotechnical unit GU4b, where the SSPC survey was conducted, visual assessment of the discontinuities dominantly shows straight to slightly curved large scale roughness (table 5-2). The infill material comprises medium to coarse soft sheared material such as clays.

Table 5-2: Summary of the condition of discontinuities of the GU4b geotechnical unit in Romberg Sandstone quarry using SSPC.

Set	persistence along strike (m)	persistence along dip (m)	Roughness large scale	Roughness Small scale	infill material
1	>2	>2	straight	rough undulating	coarse soft sheared materials such as clay
2	>1.5	>2	slightly curved	rough undulating	Non-softening and sheared material such as free of clay

3	>2	>1.4	slightly curved	rough planar	Non-softening and sheared material such as free of clay
4	>2	>1.6	straight	rough planar	medium soft sheared material such as clay and silt

In geotechnical unit GU5, where the scanline survey was conducted, the bedding planes and joint sets show slightly curved large scale roughness with infill material of non-softening sheared material such as clay, talk etc. (table 5-3).

Table 5-3: Summary of the condition of discontinuities of the GU5 geotechnical unit in the Romberg Sandstone quarry using SSPC.

Set	persistence along strike (m)	persistence along dip (m)	Roughness large scale	Roughness small scale	infill material
1	>2	>0.2	straight	rough undulating	coarse soft sheared materials such as clay
2	>2	>0.2	slightly curved	rough undulating	Non-softening and sheared material such as free of clay
3	>0.3	>0.2	slightly curved	rough planar	Non-softening and sheared material such as free of clay
4	>0.2	>0.2	straight	rough planar	medium soft sheared material such as clay and silt

Note that the origin of the small quantities of clay infill material in the bedding planes can be attributed to the change in sedimentary sequence often resulting in some clay richer beds. On the other hand, the infill material of the joints is sheared materials free of clay except for the infill material of joints in Set 4. The clay in those joints perhaps have originated from clays in bedding planes which may later have flushed into the joints or clays from bedding planes may have been transported by groundwater into the joints.

5.1.4. Discontinuity characterization using scanline survey method

Four scanline surveys were carried out on the lower section of the Geotechnical unit 5 in accordance with the method suggested by Hoek & Bray, (1981a) as explained in section 4.2 and shown in figure 5-3 below. A total length of 11.4m scanline survey was conducted and mapped 46 discontinuity planes.

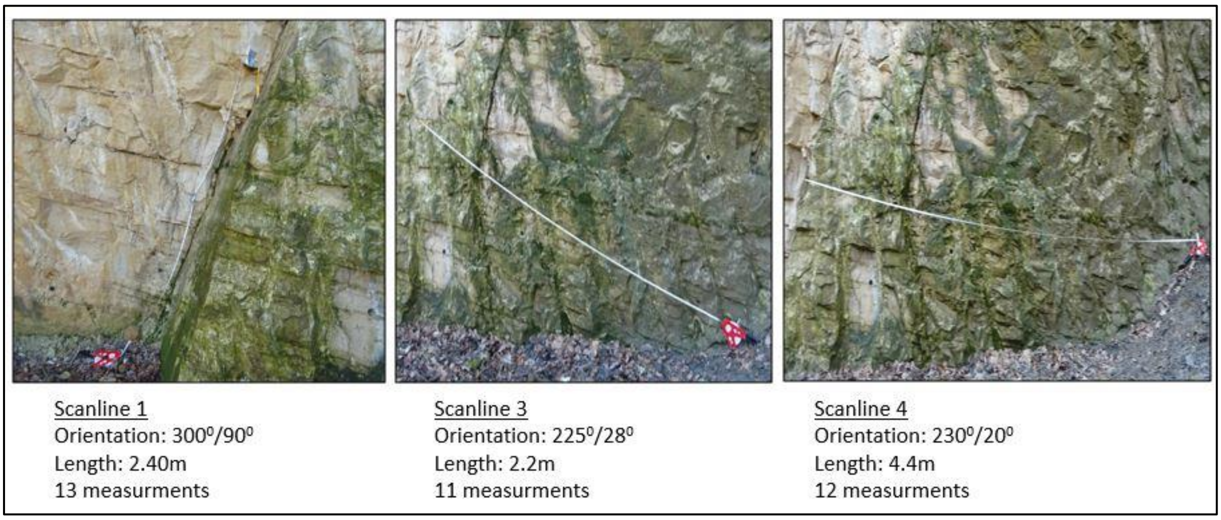

Figure 5-4: scanline surveys and their parameters

By plotting all the planes measured in the scanline survey in a stereographic plot (figure 5-5) four discrete sets were identified. The two sets are bedding planes, which are very closely clustered as expected for bedding planes, and the other two are joint sets.

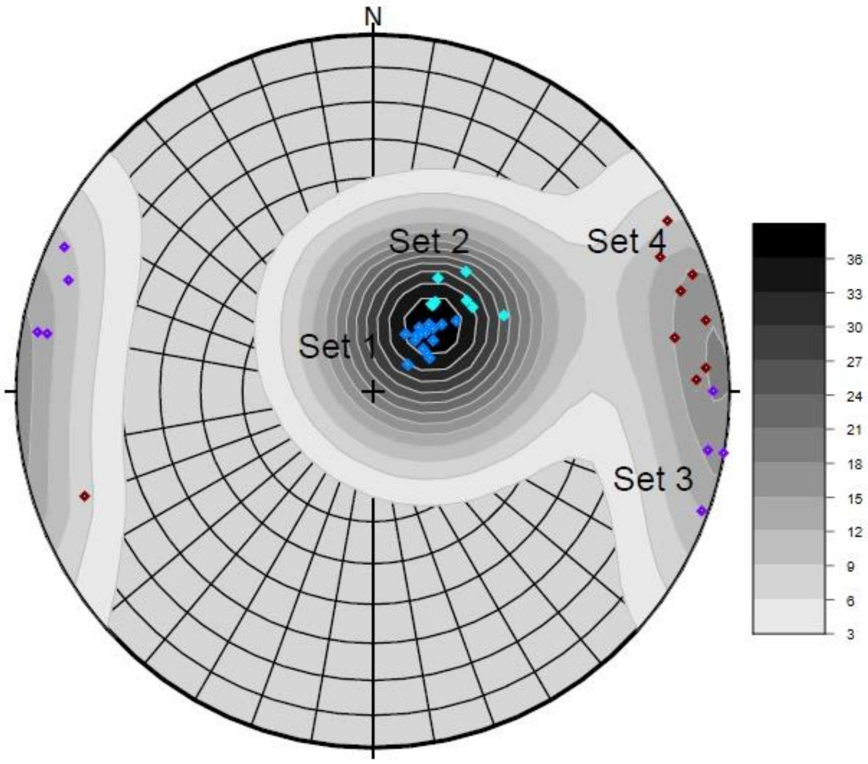

Figure 5-5: Equal area, lower hemisphere grey scale stereo density plot of poles of discontinuity sets mapped using Scanline method. Counting method applied: Fisher distribution.

Spherical statistics including the mean orientation and dip angle, the resultant vector, R, Fisher's K and spherical variance of each set were calculated based on the methodology described in section 4.2.1.4. Furthermore, discontinuity set spacing was computed via sorting of all the intersection distances of each discontinuity plane in each set in the scanline survey. A list of set spacing was computed by subtracting subsequent intersection distances of discontinuity planes that belong to the same set, thus generates only the set spacing or apparent discontinuity spacing. The apparent spacing must be corrected to obtain the normal set spacing. The normal spacing, which is the orthogonal distance between two parallel discontinuities in the same set, was obtained by multiplying the apparent spacing of each discontinuity plane in the same set by the average of the cosine of the acute angle between the normal corresponding to the mean orientation of the discontinuity plane and the bearing and plunge of specific scanline. The normal spacing was obtained as described in section 4.2.3. Table 5-4 below shows the summary of the results of spherical statistics of the scanline surveys conducted on the Romberg sandstone quarry.

*Table 5-4: Summary of the results of spherical statistics of Identified and characterized discontinuity sets using scanline survey. Remark: * denotes the value of Fisher's K is not valid since the number of observations, N is less than 10.*

	Set 1	**Set 2**	**Set 3**	**Set 4**
Geologic origin	Bedding plane	Bedding plane	Joint	Joint
Mean dip direction (degrees)	224	221.7	101.7	254
Mean dip angle (degrees)	17.2	28.77	89.3	83.4
Number of Observation N	20	8	9	10
Resultant R	19.92	7.95	1.46	7.98
Fisher's K	229.85	122.9*	0.92*	3.98
Spherical Variance	0.00392	0.0061	0.83	0.2
Mean normal spacing (m)	0.132	0.2275	0.376	0.434
Stand. Dev. NS. Spacing	0.124	0,364	0.402	0.236
Maximum Normal setting (m)	0.4608	0.9367	1.535	0.601

5.1.5. Evaluation of the results of traditional discontinuity Surveys

Open source software called OSXStereonet, which have been developed by (Cardozo & Allmendinger, 2013) was used to plot the collected discontinuity data on the stereonet. From stereo-plots of the SSPC survey, four distinct discontinuity sets were recognized. The first set (Set 1) is set of bedding planes, which comprises three discontinuity planes with mean dip direction and dip angle of 211.57^0 and 24.42^0 respectively. The mean normal spacing of this set is 1.43m indicating thick bedding planes. The persistence of the bedding planes runs for more than 3m both along dip and strike. The second set (Set 2) consists of a set of joint planes. Seven discontinuity planes belong to this set having mean dip direction and dip angle of 29.47^0 and 66.90^0 respectively. The mean normal spacing of this set is 1.6m. This means the joints show wide spacing (BS 5930, 1999). The third and fourth sets are also joint sets with wide to very wide spacing.

Similarly, stereo plotting of all the discontinuity data from scanline survey has resulted in the recognition of four main discontinuity sets (figure 5-5). The two sets of bedding planes identified in the field during the scanline survey (Set 1 and Set 2) show comparable dip direction, but the difference between the dip angles reach up to 10^0. The 'Set 2' bedding planes are more steeply bedded and terminate on the 'Set 1' bedding plane. This shows the 'Set 2' bedding planes were deposited by channel infill material. Both sets of bedding planes are thinly bedded having a normal set of spacing of 0.1 to 0.2m.

5.1.6. Discussion and comparison of traditional discontinuity Surveys

As can be seen from the above stereo-plots (figure 5-4 and 5-5), both the SSPC and scanline surveys were able to recognize distinct discontinuity sets. Both methods were able to identify one bedding plane set and one joint set commonly. Poles of comparable discontinuity sets recognized by both methods were given similar colours in the stereo-plots mentioned above. Joint 'Set 4' mapped by the SSPC method corresponds well with joint 'Set 3' mapped by the scanline. Both joints sets show comparable orientations. Joint 'Set 2' recognized by the SSPC method and Joint 'Set 4' identified by the scanline survey show the difference in dihedral angle of 600 (refer section 5.4.1 for more on dihedral angle). 'Set 1' in the SSPC and 'Set 1' and 'Set 2' in the scanline correspond well with each other except the dip angle of 'Set 2' of bedding planes mapped by the scanline show greater inclination. The more inclined bedding planes correspond to the infill channel deposits. However, the normal spacing of the bedding planes in the SSPC survey are much larger than the spacing of the bedding planes recognized by the scanline method. This is because the SSPC method provides generalized geometric information of discontinuities in the rocks mass exposure. As a result, the SSPC system can present human bias on the identification and determination of representative discontinuity sets in addition to errors involved during taking measurements. Though the SSPC method results in certain bias in identifying independent joint sets, it is regarded as an important first step in the entire rock mass characterization process. It is worth to note that weathering has no impact on the reduced spacing of the bedding planes recognized by the scanline method in the GU5 as incorrectly stated in Fakunle, (2016) because both the GU4b and GU5 geotechnical units exhibit the same degree of weathering, SW to fresh.

In conclusion, both the scanline and the SSPC surveys were able to recognize distinct discontinuity sets. The scanline identified four main discontinuity sets. The SSPC method also recognized four distinct discontinuity sets. The mean normal set spacing of discontinuities mapped by rapid face mapping, the SSPC survey, in most cases revealed several times larger than the normal set spacing computed by the scanline survey.

5.2. Results of computed discontinuity geometry derived from TLS point clouds

The geometries of discontinuities derived from TLS point clouds were computed according to the methodology outlined in section 4.6.2. After the discontinuity planes were generated from point cloud data, the normal vectors (poles) of each discontinuity plane were plotted on a stereographic projection to visually examine the possible number of discontinuity sets (figure 5-7). Accordingly, four discontinuity sets were determined as the appropriate number of distinct discontinuity clusters. Therefore, all the discontinuity planes were objectively clustered into four clusters by using Fuzzy k-means clustering technique (Figure 5:8). Once the discontinuity sets were determined it was appropriate to compute spherical statistics for each set. Thus, Mean set orientation (dip direction and dip angle), the normalized resultant vector (R), Fisher's K, spherical variance, the number of planes and normal set equivalent normal set spacing were computed for each set according to the methods explained in sections 4.2 to 4.4.

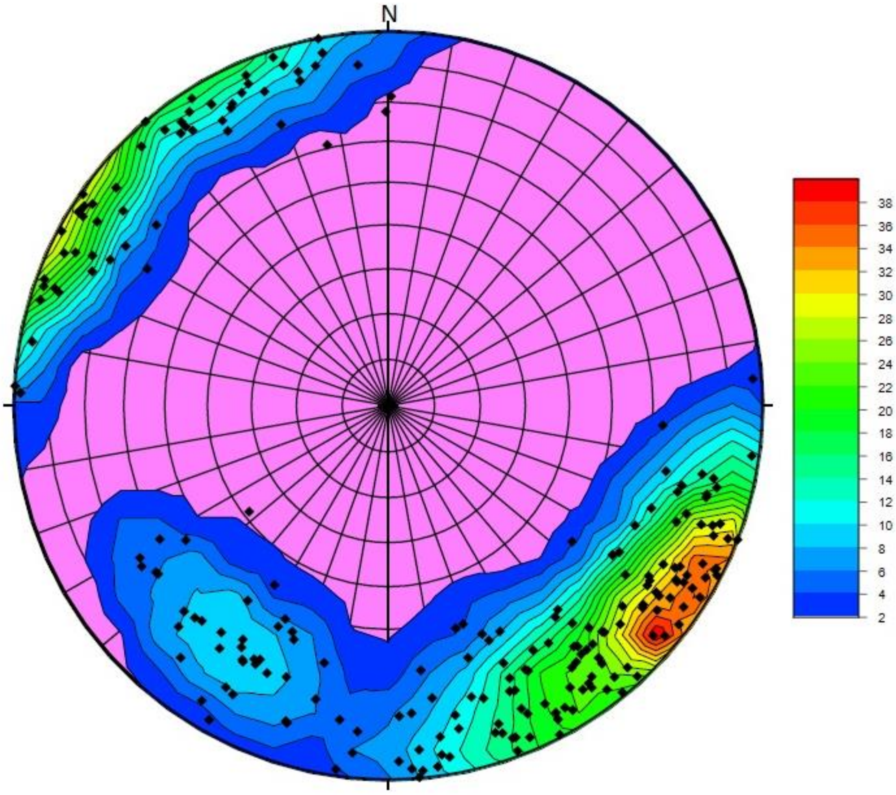

Figure 5-6: Equal area stereographic polar plot of all the discontinuity planes derived from UAV based point clouds. In total, 337 discontinuity planes were derived. The black diamonds represent individual poles and the coloured contours represent pole densities.

The results of computed spherical statistics of each discontinuity set geometry derived from TLS point clouds via point cloud segmentation and further analysis is summarized in table 5-5 below.

Table 5-5: Summary of the results of spherical statistics of discontinuity sets derived from TLS point clouds. The total number of discontinuity planes is 223.

	Set 1	**Set 2**	**Set 3**	**Set 4**
Mean dip direction (degrees)	33,02	297,21	329,58	353,90
Mean dip angle(degrees)	64,90	83,69	80,68	87,16
R(Normal resultant vector)	37,65	75,25	74,09	26,12
N (# of poles)	39	80	77	27
K (Fisher K)	27,51	16,43	25,79	28,25
S (standard deviation)	0,03	0,06	0,04	0,03
Mean equ. Normal spacing (m)	0,32	0,21	0,12	0,65
Std dev. equ. Normal spacing	0,46	0,42	0,21	1,36
Max equ. normal spacing (m)	2,38	2,75	1,37	1,96

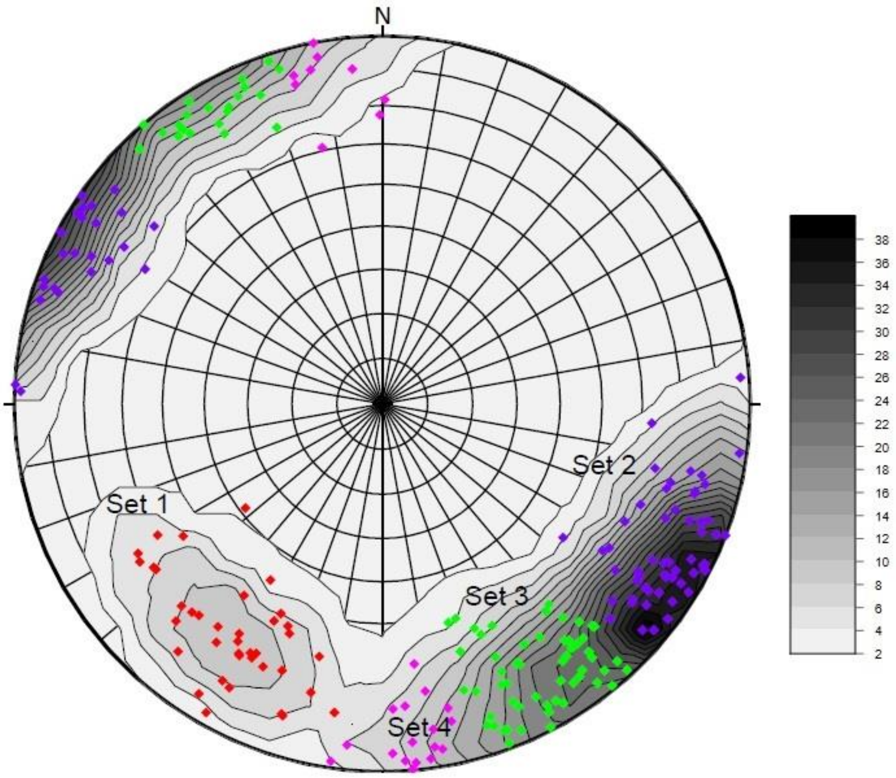

Figure 5-7: Lower hemisphere equal area stereographic polar plot of all the discontinuity planes derived from UAV based point clouds segmentation with program Stereonet (Cardozo & Allmendinger, 2013). In total, 337 discontinuity planes were derived. The poles are coloured according to their set membership and the grey contours show pole densities.

5.3. Results of computed discontinuity geometry derived from UAV based point clouds

The geometries of discontinuities derived from UAV based point clouds were computed according to the methodology outlined in section 4.6.2. After the discontinuity planes were generated from point cloud data, the normal vectors (poles) of each discontinuity plane were plotted on a stereographic projection to visually determine the number of potential discontinuity sets (Figure 5-9). Accordingly, five discontinuity sets were identified as the appropriate number of distinct discontinuity clusters. When the classification was set to be four clusters, the different sets are merged providing different statistical values. Therefore, all the poles of discontinuity planes were objectively clustered into five clusters by using Fuzzy k-means clustering technique (figure 5-10). The additional one discontinuity set identified from UAV based point clouds comprises the bedding planes. The TLS survey did not scan the bedding planes on the lower section of the slope due to occlusion. Once the discontinuity sets were defined it was appropriate to compute spherical statistics for each set. Thus, Mean set orientation (dip direction and dip angle), the normalized resultant vector (R), Fisher's K, spherical variance, the number of planes and equivalent normal set spacing were computed for each set.

The results of computed spherical statistics of each discontinuity set geometry derived from UAV based point clouds via point cloud segmentation and further analysis is summarized in table 5-6 below.

Table 5-6: Summary of the results of spherical statistics of discontinuity sets derived from UAV based point clouds. The total number of discontinuity planes is 337.

	Set 1	Set 2	Set 3	Set 4	Set 5
Mean dip direction(degrees)	220.32	34.24	301.61	327.73	174.65
Mean dip angle(degrees)	17.33	77.95	86.16	86.95	88.06
R(Normal resultant vector)	7.9	39.43	103.46	114.69	46.52
N (# of poles)	8	51	109	120	49
K (Fisher K)	95	4.23	19.31	22.24	18.99
S (standard deviation)	0.01	0.23	0.05	0.04	0.05
Mean equ. Normal spacing (m)	0,40	0,20	0,15	0,12	0,24
Std dev. equ. Normal spacing	0,50	0,25	0,31	0,57	0,28
Max equ. normal spacing (m)	1,20	1,09	2,15	1,06	1,10

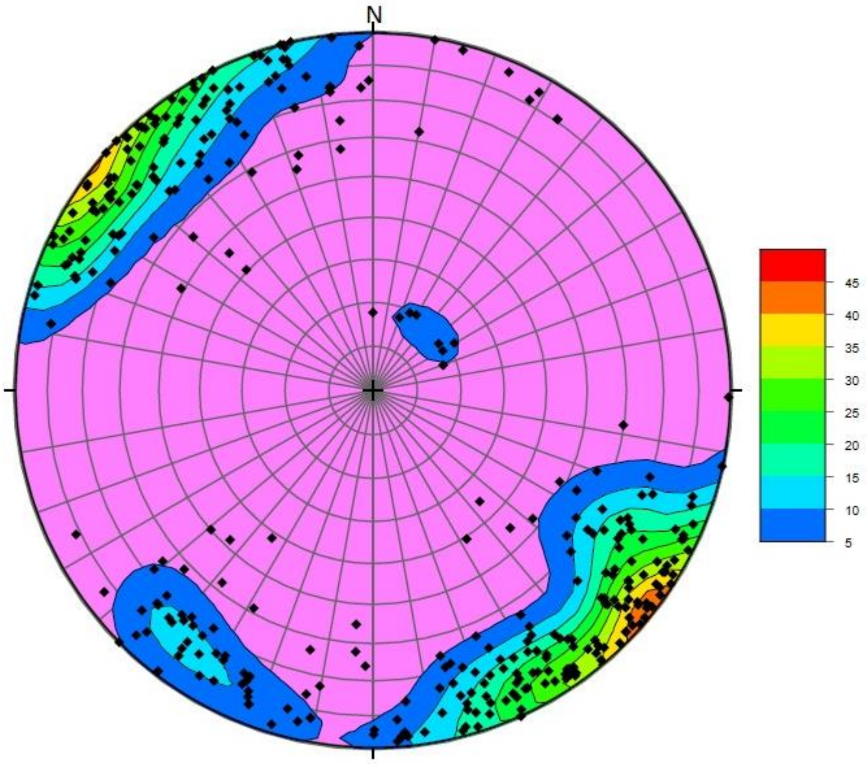

Figure 5-8: Lower hemisphere equal area stereographic polar plot of all the discontinuity planes derived from TLS point clouds with program Stereonet (Cardozo & Allmendinger, 2013). In total, 337 discontinuity planes were derived. The black diamonds represent individual poles and the coloured contours represent pole densities.

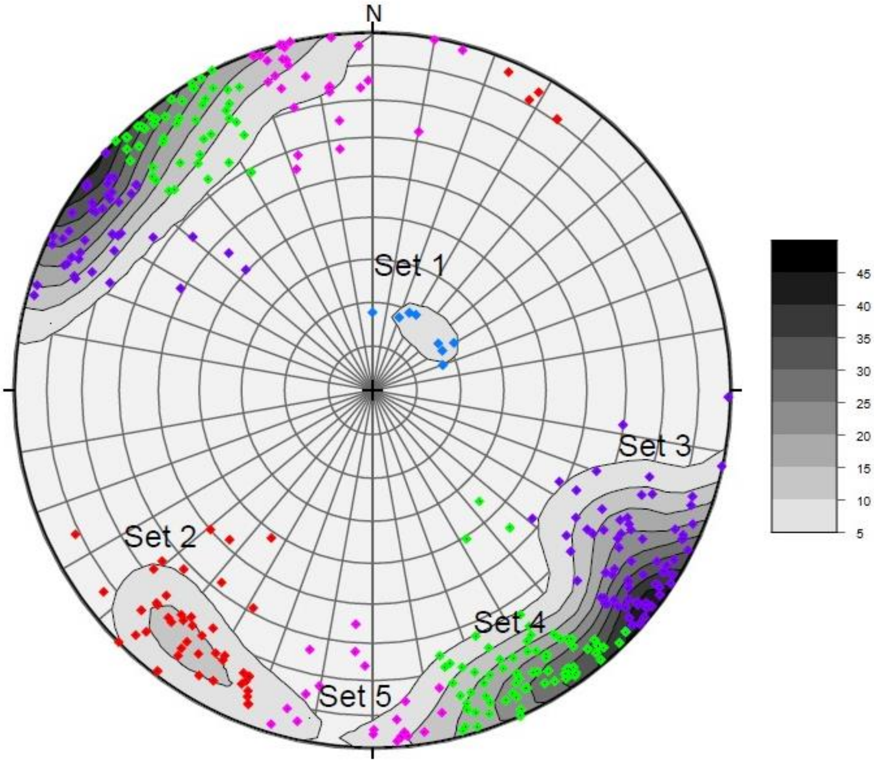

Figure 5-9: Equal area stereographic polar plot of all the discontinuity planes derived from TLS point clouds. In total, 337 discontinuity planes were derived. The poles are coloured according to their set membership and the grey contours show pole densities.

5.4. Evaluation of the results of computed discontinuity geometries derived from traditional methods versus point cloud segmentation approaches

The computed discontinuity geometries such as dip direction, dip angle and spacing are evaluated in three cases:

- A quantitative plane by plane comparison between point clouds segmentation based versus conventional field-based discontinuity orientations;
- A qualitative comparison between point cloud segmentation based versus field based discontinuity sets; and
- A comparison between the equivalent normal spacing of discontinuity sets derived from segmentation based versus field based discontinuity sets.

5.4.1. Quantitative plane by plane comparison

In order to validate the accuracy of the orientation of individual discontinuity planes derived from both TLS and UAV-based point clouds, seven discontinuity planes that showed a high degree of planarity were measured in the field using a geologic compass as illustrated in figure 5-11. Similarly, segmented point clouds that represent equivalent discontinuity planes at the base of the slope were selected, retrieved and computed from both TLS and UAV-based segmented point clouds. Thus, computed orientations derived from point cloud segmentation were compared with conventional orientation measurements to verify the accuracy of selected individual discontinuity planes. The comparison of computed and manually measured orientations of discontinuity planes was carried out in terms of pole-vector difference or dihedral angle, θ, between the normal vectors of two discontinuity planes. The dihedral angle between normal vectors of two discontinuity planes is computed by the formula:

$$\cos\theta_{AB} = \overline{n}_A \cdot \overline{n}_B$$

The dihedral angle is used as a measure of the angular difference between two poles of discontinuity planes since the angular difference between two planes cannot be computed by arithmetic subtraction of dip directions and dip angles.

Figure 5-10: Discontinuity planes measured manually and marked in the lower section of the Romberg quarry slope for plane to plane comparison with discontinuity planes derived from the two point cloud segmentation method. The measured values of the orientations are listed in table 5-6. Marked planes from 1 to 5 represent joint planes, whereas marked planes 6 and 7 are sub horizontal bedding planes.

The results of computation of the dihedral angle between the manually measured discontinuity planes versus discontinuity planes derived from TLS point cloud segmentation showed better much than orientations manually measured versus discontinuity planes derived from UAV based point cloud segmentation (tables 5-7 and 5-8). The comparison was made between five discontinuity planes derived from TLS data set, and seven discontinuity planes derived from UAV based point clouds against the manually measured orientations. The two extra discontinuity planes (marked planes 6 and 7) are bedding planes sampled by UAV-based point cloud segmentation.

Table 5-7: Dihedral angle difference between manually measured versus computed discontinuity planes derived from TLS point cloud segmentation.

	Manual readings		Computed from TLS points		Dihedral angle (deg)
Mark on the photo	Dip dir (deg)	Dip (deg)	Dip dir (deg)	Dip	
1	30	50	27	58	8.36
2	34	65	27.2	62	6.78
3	314	65	310	66	3.77
4	31	80	30.3	75	5.05
5	31	55	28.6	59.5	4.93
				Mean	5.77

	Stnd dev	1.80

Table 5-8: Dihedral angle difference between manually measured versus computed discontinuity planes derived from UAV based point cloud segmentation.

	Manual readings		Computed from UAV points		Dihedral angle (deg)
Mark on the photo	Dip dir (deg)	Dip (deg)	Dip dir (deg)	Dip	
1	30	50	28	60	10.13
2	34	65	32.2	63	2.57
3	314	65	313.9	68	3.00
4	31	80	35.7	82.4	5.23
5	31	55	24.8	60	7.23
6	200	25	200	17.6	7.40
7	215	25	234.5	18	9.92
				Mean	6.50
				Stnd dev	3.04

Tables 5-7 and 5-8 show comparable mean values of the difference in dihedral angle between manually measured and computed orientation of discontinuity planes derived from both TLS and UAV-based point cloud segmentation. However, the pole vector difference between manually measured versus computed TLS derived discontinuity planes have a lower standard deviation. The values of dihedral angle difference are generally larger for sub horizontal bedding planes than the vertical/sub-vertical joint planes. The result is similar as stated by Einstein & Baecher, (1983), which asserted that the dihedral angle difference between sub horizontal bedding planes are generally larger than the difference between vertical/sub-vertical discontinuity planes. The dihedral angle differences between the computed and manually measured orientations can be attributed to several error sources. Windsor & Robertson, (1994) stated that manual measurement of discontinuity planes by geologic compass may introduce a reading error of ± 5 degrees for dip angle and ± 10 degrees for dip direction. Besides, during field work orientation measurements were taken from one spot on the plane. This means the variation of orientations on a single plane is not included in the analysis unlike computed discontinuity orientations derived from point cloud segmentation, which measures the orientation of the entire plane, although the dimension of the plane may vary depending on segmentation parameters applied. Another source of error may come from less accurate registration of the two point clouds. Even though ground control points were measured at the base of the slope with accurate differential GPS for the purpose of georeferencing the point clouds, due to the effect of multipath from vertical rock face some of the accuracy of the measured GCP were low as mentioned in section 4.5. Noise in the point cloud data due to vegetation may also affect the accuracy of the computed discontinuity measurements although it is not that significant since the method of segmentation applied (Hough transform and Least squares) computes best fitting planes that are not significantly impacted by the noise in the point cloud data (Slob et al., 2010).

5.4.2. Qualitative comparison between computed discontinuity sets derived from point cloud segmentation versus discontinuity sets measured by conventional field-based methods

Each of the discontinuity sets computed from TLS and UAV-based point cloud segmentation is evaluated qualitatively against discontinuity sets measured from the field by scanline and SSPC methods. Discontinuities derived from TLS point cloud segmentation were classified into four sets, whereas those from UAV-based point cloud segmentation were classified into 5 different sets. On the other hand, using the SSPC approach four discontinuity sets were visually identified. The scanline method identified four discontinuity sets. The comparison among different sets of discontinuities identified by the aforementioned different methods is based on the mean orientation (dip direction and dip angle) and Fisher's K values computed for each set. Table 5-9 illustrates the summary of the above-mentioned discontinuity geometries computed for each set.

Table 5-9: Comparison of computed geometric properties of each discontinuity sets derived from different methods. The mark '' and N/A denote the value of the Fisher's K is not valid since the number of observations, N is less than 10. Discontinuity sets derived from different methods but that belong to the same generic set are given similar background colour. The bold values show higher values than the corresponding entries in other sets.*

		Set 1	Set 2	Set 3	Set 4	Set 5
Segmentation of TLS point clouds	Discontinuity type	Joints	Joints	Joints	joints	
	Mean dip dir (deg)	33.02	297.21	329.58	353.90	
	Mean Dip(deg)	64.90	83.69	80.68	87.16	
	Fisher's K	27.51	16.43	25.79	28.25	-
Segmentation of UAV-based point clouds	Discontinuity type	Bedding planes	Joints	joints	joints	joints
	Mean dip dir (deg)	220.32	34.24	301.61	327.73	174.65
	Mean Dip(deg)	17.33	**77.95**	86.16	86.95	88.06
	Fisher's K	95*	4.23	19.31	22.24	18.99
SSPC Method	Discontinuity type	Bedding planes	Joints	Joints	joints	
	Mean dip dir (deg)	211.57	29.47	312.68	289.2	-
	Mean Dip(deg)	24.42	66.98	66.65	85.0	
	Fisher's K	N/A	N/A	n/a	N/A	
Scan line survey	Discontinuity type	Bedding planes	bedding planes	joints	joints	
	Mean dip dir (deg)	224.00	221.7	101.7	254.0	
	Mean Dip(deg)	17.20	**28.77**	89.3	83.04	-
	Fisher's K	**229.85**	122.9*	N/A	3.96	

Table 5-9 shows that a high consistency occurs between mean orientations of the bedding planes derived from UAV based point cloud segmentation and the two traditional field methods except for the higher value of mean dip angle of cemented bedding planes sampled by scanline method (Set 2 on scanline survey as shown in figure 5-5). Likewise, high consistency of orientation results can be observed among joint orientation sets derived from segmentation of the two point clouds and the SSPC method except for the high value of dip angles of joints computed from UAV based point clouds. Similarly, the orientations of joints derived from the segmentation of the two point clouds have shown high consistency, but computed mean dip angles from UAV point cloud segmentation are slightly larger for all the sets.

With regard to Fisher's K value, the different discontinuity sets show values in the range of 3.96 to 28, except the 'Set 1' of the bedding planes sampled by scanline survey. Fisher's K values are utilized to show the dispersion or variability of the orientations of the distinct discontinuity planes within a discontinuity cluster. Therefore, the computed values shown in table 5-9 represent closely oriented and a strong co-planar discontinuity planes. This is because small Fisher's K value represent a uniform spherical distribution (Slob et al., 2010).

Furthermore, in order to assess and intuitively compare the different discontinuity sets derived from different methods, poles of the mean orientations of each discontinuity set were plotted on a single stereographic plot to distinguish identical discontinuity sets as illustrated in figure 5-12. The grey-scale density shows pseudo-density since the poles represent mean orientations of the discontinuity planes in each set, not the individual discontinuity planes. The density concentrations permit quick assessment of the differences and similarities between the computed discontinuity mean orientations obtained from the two point cloud segmentation based and the other two conventional field methods. Accordingly, all the 17 different discontinuity sets were "reclassified" into five generic discontinuity sets labelled from 'A' to 'E' and two separate discontinuity sets as illustrated in figure 5-12. These generic discontinuities sets serve as a basis for qualitative comparison among the different discontinuity sets derived from point cloud segmentation and traditional field survey. The comparisons, in turn, allow validation of the orientation of the discontinuity planes derived from point cloud segmentation with respect to discontinuity geometric information generated by traditional methods.

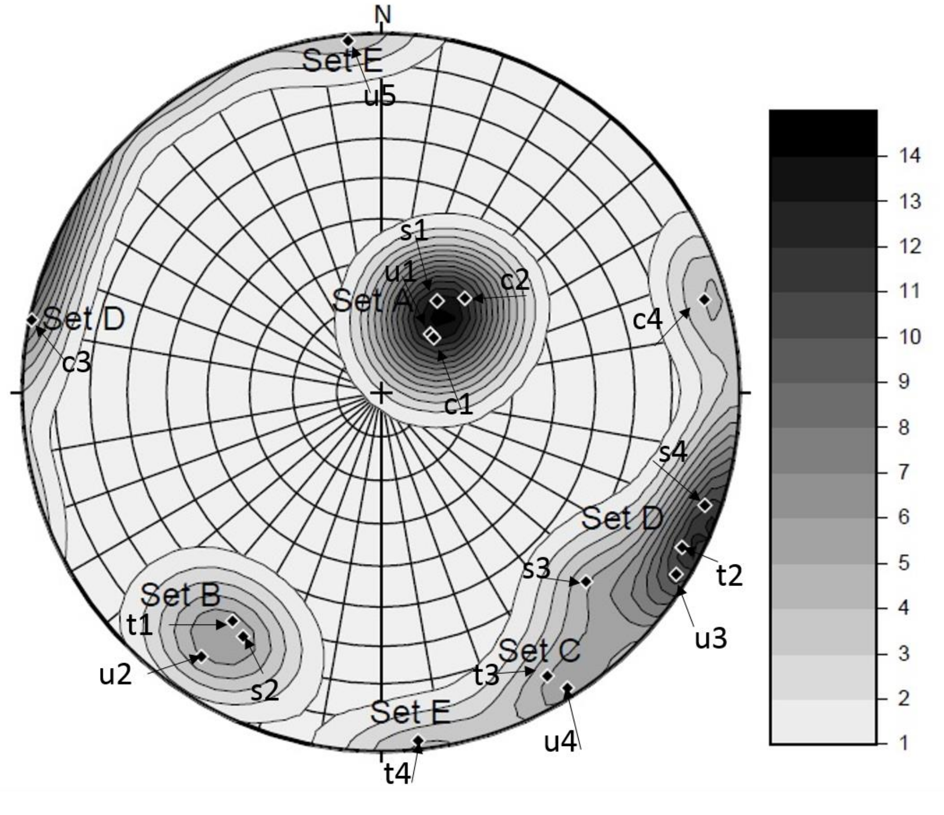

Figure 5-11: Grey-scale stereographic polar plot of mean orientation of each discontinuity sets computed for all methods. The letter labels indicate the method applied and the number refers to set number (e.g. label t1 refers to TLS based segmentation, set 1). The letters u, t, s, c represent UAV based, TLS, SSPC, and Scanline surveys respectively.

Figure 5 shows the five generic sets identified and labelled from 'Set A' to 'Set E' and the two separate discontinuity sets. The generic sets are briefly evaluated and discussed as follows.

-**Set A:** represents one of the most unambiguous sets of bedding planes recognized by UAV-based point cloud segmentation, the scanline, and the SSPC methods as shown by the green coloured discontinuity sets in table 5-9. The bedding planes dip toward SSE with a difference in orientations up to 10 degrees. Bedding planes derived from UAV based point clouds and 'Set 1' of bedding planes measured by the scan line method are very similar. Therefore, the orientations of the corresponding sets derived from the different methods that belong to generic 'Set A' showed high consistency. It is important here to observe that the TLS based segmentation missed the bedding planes due to the obvious reason-occlusion or shadow zones. This results when the discontinuity planes are oriented parallel/subparallel to the incoming laser beam. Thus, no point cloud data are available that meet the segmentation parameters outlined in table 4-4.

-<u>Set B</u>: represents the most prominent sub-vertical joint sets in the Romberg quarry. It is almost perpendicular to the bedding planes. It is labelled 'Joint set 1' on figure 5-1 and coloured magenta in table 5-9. The orientations of the joint sets are relatively consistent. The orientations of dip directions of the sets are comparable. However, the difference in dip angle reaches up to 13 degrees. Both sets were recognized by the two point cloud segmentation and the SSPC methods. The TLS based point cloud segmentation and the SSPC methods produced orientations that showed slightly higher consistency compared to joint sets derived from the UAV based point cloud segmentation and the SSPC methods. The scanline didn't intersect this joint set and thus missed it.

-<u>Set C</u>: This third generic vertical joint set is recognized by the two point cloud segmentation processes. 'Set 3' of the TLS and 'Set 4' of the UAV based joint sets labelled as t3 and u4 on figure 5-12 respectively belong to this generic set. The two sets show consistent orientations. The difference in orientation between the two sets is less than six degrees. Both the SSPC and the scanline methods didn't recognize these joint sets.

-<u>Set D</u>: The fourth generic set is the second most unambiguous set comprising vertically dipping joint sets. It is labelled 'Joint set 2' on figure 5-1 and coloured blue in table 5-9. This generic joint set also shows wide discontinuity spacing as explained in section 5.1.5. Both the conventional discontinuity mapping methods and the two segmentation based methods recognized this set. 'Set 3' in UAV based point cloud segmentation, 'Set 2' in TLS point cloud segmentation, 'Set 4' in the SSPC and 'Set 3' in the scanline survey all belong to this generic set. The dip direction of 'Set 3 or c3' in the scanline survey is oriented 180^0 opposite the other joint sets.

<u>Set E</u>: This third generic vertical joint set is recognized by the two point cloud segmentation processes. 'Set 4' of the TLS and 'Set 5' of the UAV based joint sets labeled as t4 and u5 on figure 5-12 respectively belong to this generic set. The two sets showed highly consistent orientations. The difference in dip angle between the two sets is less than one. The dip direction of 'Set 5 or u5' of the UAV based segmentation is oriented 180^0 opposite the joint set derived from the TLS point cloud segmentation. Both the SSPC and the scanline methods didn't recognize these joint sets.

<u>c4</u>: 'Set 4' of the scanline survey doesn't fall in any generic set. This single vertical joint set is not sampled by the other three methods.

<u>s3</u>: comprises the single joint set sampled by the SSPC method as 'Set 3'. It is oriented between the generic sets 'Set C' and 'Set D'. Only three joint planes belong to this set. Thus, the mean orientation calculated may not show statistically sound meaning.

5.4.3. Comparison of Equivalent normal spacing

For discontinuity planes derived from the two point cloud sources (TLS and UAV-based) equivalent normal set spacing statistics were computed according to the method described in section 4.6.3. On the other hand, for data generated from conventional field-based methods (the SSPC and Scanline) discontinuity normal set spacing statistics were calculated according to the method and the steps outlined in section 4.2.2. The summary of the computed results of equivalent set spacing and normal set spacing obtained for the four methods is presented in table 5-10. The results of the set spacing parameters were coloured according to the generic set they belong as described and shown in section 5.4.2. Based on the summary of the results presented in table 5-10, the following general observations can be made with regard to set spacing distributions within the generic sets.

- The calculated mean equivalent normal set spacing distances for the TLS and UAV-based point cloud segmentation methods are comparable, but the spacing distances computed from the UAV-based method are slightly smaller.
- The computed maximum equivalent normal spacing values of joint sets derived from the TLS based point cloud segmentation show higher values in comparison to the UAV-based point cloud segmentation for all the four joint sets commonly sampled by both methods. Furthermore, maximum spacing values computed from TLS method are roughly comparable to maximum spacing values measured by the SSPC method. Note that the comparison of computed discontinuity spacing derived from point cloud segmentation methods against the spacing measured by manual methods does not make much sense, because the method employed to segment the point clouds don not recognize traces or cemented bedding planes. In addition, the scanline and the SPPC surveys were conducted on different geotechnical units with different bedding spacing. Furthermore, the computed mean equivalent normal set spacing of discontinuity sets derived from the two point cloud segmentation represents the average spacing of all planes that belong to the same set from the whole cropped point cloud data. Therefore, this rough comparison cannot be used for validation. It is rather intended to roughly compare the spacing of discontinuity sets derived from different methods that belong to the same 'generic set' as discussed in section 5.4.2.
- Considering the aforementioned argument, the mean equivalent normal set spacing distances computed for discontinuity sets derived from point cloud segmentation process are generally smaller than the measured spacing values of non-cemented discontinuity sets obtained by the SSPC method. In addition to the reasons discussed above, this is partly due to the segmentation process. Many non-continuously exposed small discontinuity planes on the rock face that belong to a single plane are segmented into separate planes resulting in even unrealistic or non-existent small spacing values (Slob et al., 2010). These extra spacing values also largely impact the calculated mean equivalent normal set spacing of discontinuity planes derived from point cloud segmentation.

Table 5-10: Summary of the results of the equivalent normal set spacing computed for discontinuity data derived from the point cloud data and the normal set spacing computed for discontinuity data generated by traditional methods. Similarly, coloured sets belong to the same generic set (A to E) as shown in fig 5-12.

	Spacing parameters	Set 1	Set 2	Set 3	Set 4	Set 5
Segmentation of TLS PC	Type of discontinuity planes	Joint	Joint	Joint	Joint	
	Mean equ. Normal spacing (m)	0.32	0.21	0.12	0.65	
	Std dev. equ. Normal spacing	0.46	0.42	0.21	1.36	
	Max equ. normal spacing (m)	2.38	2.75	1.37	1.96	
Segmentation of UAV-based PC	Type of discontinuity planes	Bedding plane	Joint	Joint	Joint	Joint
	Mean equ. Normal spacing (m)	0,4	0,24	0.15	0.12	0.24
	Std dev. equ. Normal spacing	0,5	0,25	0.31	0.57	0.28
	Max equ. normal spacing (m)	1,2	1,09	2.15	1.06	1.1
SSPC Method	Type of discontinuity plane	Bedding planes	Joint	Joint	Joint	
	Mean normal set spacing	1.43	1.6	1.367	2.2	
	Stand. Dev. NS. Spacing	0.51	0.9	0.34	1.41	

	Maximum Normal set spacing	1.3	2.4	1.8	3.2
Scan line survey	Type of discontinuity planes	Bedding plane	Bedding plane	Joint	Joint
	Mean normal spacing	0.13	0.23	0.38	0.43
	Stand. Dev. NS. Spacing	0.12	0.364	0.40	0.24
	Maximum Normal setting	0.46	0.94	1.54	0.60

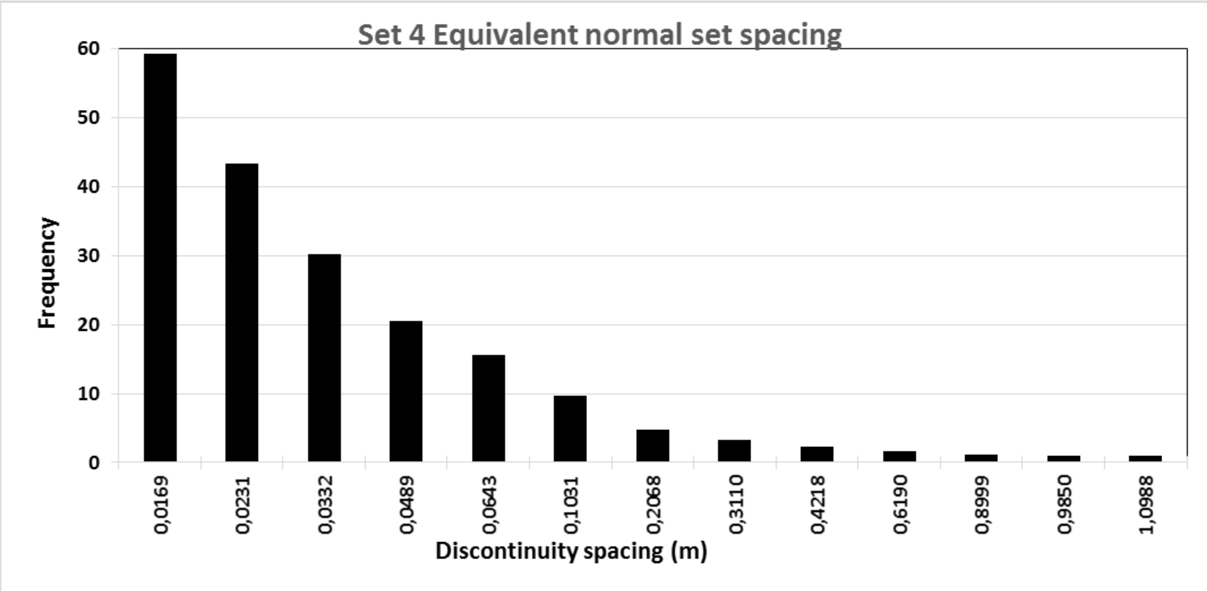

Figure 5-12: Histogram illustrating the normal frequency distribution of the equivalent normal set spacing values of discontinuity Set 4 (joint planes) for data derived from UAV based point cloud segmentation. The arithmetic mean value is 0.24m.

Furthermore, to assess the distribution of the computed equivalent normal set spacing within a particular set, the results were visualized in a histogram. As discussed above, the method used to compute the normal set spacing yields non-existent or unrealistically small spacing values. For many discontinuity sets the histogram showed a strong negative exponential distribution indicating a high occurrence of small spacing values in the data (figure 5-13). This means that the larger spacing values in the data are inadequately represented since their frequency of occurrence is low. However, the larger spacing values affect the overall behavior of a rock mass more than the small spacing do since they render the block size larger. Therefore, in order to adequately represent the larger discontinuity spacing values, a histogram in the form of logarithmic frequency distribution can be used.

From figure 5-13, it can be observed that the very small spacing values show high frequency and largely influence the mean equivalent normal set spacing values. The histogram of the equivalent normal spacing of the corresponding joint set (Set 3) derived from TLS data set also showed comparable frequency distribution as shown in figure 5-14.

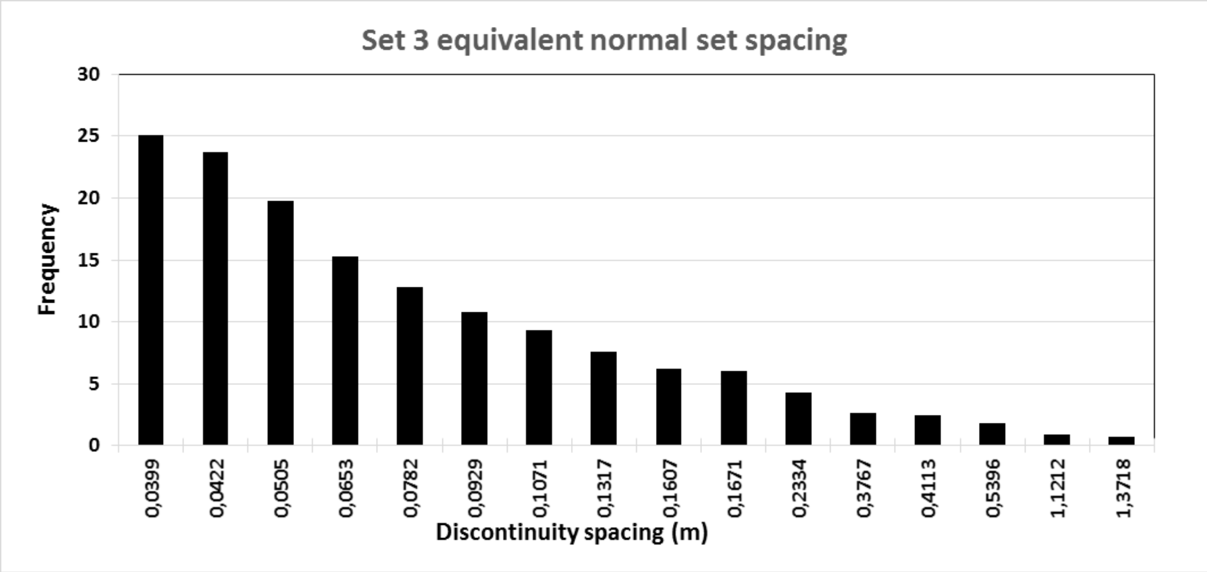

Figure 5-13: Histogram illustrating the normal frequency distribution of the equivalent normal set spacing values of discontinuity Set 3 (joint planes) for data derived from TLS point cloud segmentation. The arithmetic mean value is 0.12m.

6. CONCLUSION AND RECCOMENDATION

6.1. Conclusion

In this research discontinuity geometric properties mainly orientation, plane geometry, discontinuity set statistics and equivalent normal set spacing were derived from two point cloud data sets (UAV-based photogrammetry and Terrestrial Laser scanners) via segmentation method based on Hough transformation and Least Squares. The derived geometric properties of discontinuities were compared to discontinuity properties measured by field-based methods (scanline and the SSPC methods). For validation, the discontinuity data obtained from the two remote sensing methods were qualitatively and quantitatively compared with results generated by the two field methods.

The two conventional field-based discontinuity mapping methods (the scanline and the SSPC) were able to recognize distinct discontinuity sets. The scanline identified two bedding plane sets and two other joints sets. The SSPC method also recognized four distinct discontinuity sets, one bedding plane set and three other joint sets. From both methods, one bedding plane set and one joint set showed reasonable correlation. The mean normal set spacing of discontinuities mapped by the SSPC method, in most cases revealed several times larger than the normal set spacing computed from the scanline survey.

The setting of point cloud segmentation parameters and visually determining the number of discontinuity sets as input for fuzzy k means clustering are subjective and can result in undesirable result.

Segmentation of the UAV based point clouds generated the highest number individual discontinuity planes and sets (five sets) including the exposed bedding planes. This is because manual planning (operation) of the UAV during image acquisition process was able to highly reduce the shadow or occluded zones. However, the TLS did not scan the subhorizontal bedding planes even though scanning was carried out from three different positions.

A quantitative plane by plane comparison in terms of pole-vector difference or dihedral angle between the discontinuity planes derived from the two point cloud segmentation versus selected discontinuity planes showed a small angular differences (5 to 6 degrees), which verifies a reasonable correlation considering the numerous sources of errors involved during manual orientation measurements and point cloud generation from UAV images and limitations of TLS survey. Note that the difference in the dihedral angle between orientations of discontinuity planes measured manually versus discontinuity planes derived from TLS point cloud segmentation showed slightly more accurate orientation than the orientations of discontinuity planes measured manually and the ones derived from UAV based point cloud segmentation.

In order to qualitatively compare the mean orientations of discontinuity sets derived from all the four methods the poles of the mean orientations of each discontinuity sets were plotted on a single stereographic plot to distinguish identical discontinuity sets. Consequently, the 17 different discontinuity sets recognized by the four methods were "reclassified" into five generic discontinuity sets labeled from 'Set A' to 'Set E' and two other separate discontinuity sets. One of the most unambiguous generic set 'Set D' was distinguished by all the four applied traditional and remote sensing discontinuity mapping methods. Generic set 'Set A' was also identified by all methods except TLS based point cloud segmentation. The UAV-based and TLS point cloud segmentation methods recognized four common discontinuity sets that showed a reasonable correlation and equivalence. Discontinuity sets measured by the SSPC method coincide with two and three discontinuity sets derived from TLS and UAV-based point cloud segmentation respectively. Likewise, discontinuity sets measured by the scanline method coincide with one and two discontinuity sets derived from TLS and UAV-based point cloud segmentation respectively.

A comparison between the mean equivalent normal set spacing of corresponding discontinuity sets derived from both UAV-based and TLS point cloud segmentation shows comparable results indicating a good degree of correlation.
The comparison of computed discontinuity spacing derived from point cloud segmentation methods against the spacing measured by manual methods does not comparison cannot be used for validation. Because the method employed to segment the point clouds don not recognize traces or cemented bedding planes. Furthermore, the computed mean equivalent normal set spacing of discontinuity sets derived from the two point cloud segmentation represents the average spacing of all planes that belong to the same set from the whole cropped point cloud area.

Both the UAV based and TLS point cloud segmentation showed a limitation in recognizing cemented or unexposed discontinuities such as bedding planes on the geotechnical unit GU5 in figure 5-1. In addition,

The UAV-based point cloud segmentation can generate discontinuity orientations within a comparable accuracy to both the TLS point cloud segmentation and the SSPC methods. Therefore, the use of UAVs can offer a reasonable alternative to both the conventional and TLS methods for rock mass discontinuity characterization. Besides, the effect of occlusion is highly reduced in UAV-based photogrammetry thus allowing reconstruction of a more comprehensive 3D structure of the rock face as compared to the TLS.

6.2. Recommendation

In the light of gaps and conclusions drawn from the research the following recommendations are put forwarded:

- The employed method of point cloud segmentation recognizes only exposed discontinuity planes. In order to map traces or cemented discontinuity planes via an automated method and compare the result with measurements by manual methods, integration of point cloud segmentation and digital imagery is highly important.
- Characterization of discontinuity roughness from UAV based point clouds is recommended as a future study topic.
- The use of Theodolite is recommended to measure more accurate ground control points on the rock face wall since the measuring ground control points by Differential GPS is affected by multipath from the rock face. The former is more suited to measure ground control points placed even on the (sub-)vertical rock face.
- The employed method to compute the spacing distance of discontinuities derived from point cloud segmentation underestimates the mean equivalent normal set spacing. Therefore, developing a new method that incorporates or merge the non-continuous but potentially similar and small discontinuity planes into one single discontinuity plane is important.

LIST OF REFERENCES

Assali, P., Grussenmeyer, P., Villemin, T., Pollet, N., & Viguier, F. (2014). Surveying and modeling of rock discontinuities by terrestrial laser scanning and photogrammetry: Semi-automatic approaches for linear outcrop inspection. *Journal of Structural Geology*, *66*, 102–114. http://doi.org/10.1016/j.jsg.2014.05.014

Bemis, S. P., Micklethwaite, S., Turner, D., James, M. R., Akciz, S., Thiele, S. T., & Bangash, H. A. (2014). Ground-based and UAV-Based photogrammetry: A multi-scale, high-resolution mapping tool for structural geology and paleoseismology. *Journal of Structural Geology*, *69*, 163–178. http://doi.org/10.1016/j.jsg.2014.10.007

Besl, P. J., & Mckay, N. D. (1992). A method for Registration of 3-D Shapes. *IEEE TRANSACTIONS ON PATTERN ANALYSIS AND MACHINE INTELLIGENCE*, *14*. Retrieved from http://www-evasion.inrialpes.fr/people/Franck.Hetroy/Teaching/ProjetsImage/2007/Bib/besl_mckay-pami1992.pdf

Bezdek, J. C. (1981). *Pattern Recognition with Fuzzy Objective Function Algorithms*. Utah: Plenium Press, Newyork.

Bieniawski, Z. T. (1989). *Engineering Rock Mass Classifications*. Newyork, USA: Wiley.

Bingham, C. (1964). *Distributions on the Sphere and on the Projective Plane*. Yale university, New Haven, Connecticut. Retrieved from Bingham1964.pdf

Birch, J. (2006). Using 3DM Analyst Mine Mapping Suite for Rock Face Characterisation. *Laser and Photogrammetric Methods for Rock Face Characterization*, (ii).

Brady, B. H. G., & Brown, E. T. (2006). *Rock mechanics for underground mining* (Third edit). Dordrecht: Springer Netherlands.

BS 5930:1981. (1981). Code of practice for site investigations. LOndon: British Standards Institution.

BS 5930:1999. (1999). Code of practice for site investigations. *British Standard*. London: British Standards Institution. http://doi.org/10.1016/0148-9062(81)90248-5

Cardozo, N., & Allmendinger, R. W. (2013). Spherical projections with OSXStereonet. *Computers & Geosciences*, *51*, 193–205. http://doi.org/10.1016/j.cageo.2012.07.021

Chesley, J. T., Leier, A. L., White, S., & Torres, R. (2017). Using unmanned aerial vehicles and structure-from-motion photogrammetry to characterize sedimentary outcrops: An example from the Morrison Formation, Utah, USA. *Sedimentary Geology*, *354*, 1–8. http://doi.org/10.1016/j.sedgeo.2017.03.013

Clayton, C. R. ., Matthews, M. C., & Simons, N. E. (1995). *Site Investigation* (2nd ed). Oxford[England] Blackwell Science.

Colomina, I., & Molina, P. (2014). Unmanned aerial systems for photogrammetry and remote sensing: A review. *ISPRS Journal of Photogrammetry and Remote Sensing*, *92*, 79–97. http://doi.org/10.1016/j.isprsjprs.2014.02.013

Davis, J. (2002). *Statistics and data analysis in geology*. *STATISTICS AND DATA ANALYSIS IN GEOLOGY, 3rd ed* (Third ed). Newyork, USA: John and Wiley &Sons, inc. Retrieved from http://www.kgs.ku.edu/Mathgeo/Books/Stat/ClarifyEq4-81.pdf

DJI Phantom 4 – Specs, FAQ, Tutorials and Downloads. (n.d.). Retrieved April 7, 2017, from http://www.dji.com/phantom-4/info#faq

Dubelaar, C. W., & Nijland, T. G. (2015). *The Bentheim Sandstone: Geology, petrophysics, varieties and its use as Dimention Stone*. (G. Lollino, D. Giordan, C. Marunteanu, B. Christaras, I. Yoshinori, & C. Margottini, Eds.). Cham: Springer International Publishing. http://doi.org/10.1007/978-3-319-09408-3

Dubelaar, C. W., & Nijland, T. G. (2016). Early Cretaceous Obernkirchen and Bentheim Sandstones from Germany used as dimension stone in the Netherlands: geology, physical properties, architectural use and comparative weathering. In *Geological Society, London, Special Publications* (Vol. 416, pp. 163–181). http://doi.org/10.1144/SP416.13

Einstein, H. H., & Baecher, G. B. (1983). Probablistic and statistical methods in engineering geology. Specific methods and examples. Part I: Exploration. *Rock Mechanics and Rock Engineering*, *16*, 73–79.

Fakunle, A. A. (2016). *Detection of Weathering Signatures using UAV Photogrammetry in Comparison with Ground-Based Sensors*. Msc Thesis, University of Twente, Faculty of Geo-Information and Earth Observation (ITC). Retrieved from http://www.itc.nl/library/papers_2016/msc/aes/fakunle.pdf

Feng, Q., Sjögren, P., Stephansson, O., & Jing, L. (2001). Measuring fracture orientation at exposed rock

faces by using a non-reflector total station. *Engineering Geology*, *59*(1–2), 133–146. http://doi.org/10.1016/S0013-7952(00)00070-3
Ferrero, A. M., Forlani, G., Roncella, R., & Voyat, H. I. (2009). Advanced Geostructural Survey Methods Applied to Rock Mass Characterization. *Rock Mechanics and Rock Engineering*, *42*(4), 631–665. http://doi.org/10.1007/s00603-008-0010-4
Fisher, R. (1953). Dispersion on a Sphere. *Proceedings of the Royal Society A: Mathematical, Physical and Engineering Sciences*, *217*(1130), 295–305. http://doi.org/10.1098/rspa.1953.0064
fstoplounge. (n.d.). Retrieved October 26, 2016, from https://fstoplounge.com/2015/05/the-ultimate-guide-youll-ever-need-for-drones-quadcopters-uav-suas-and-rpas/
Furukawa, Y., & Ponce, J. (2010). Accurate, dense, and robust multiview stereopsis. In *IEEE Transactions on Pattern Analysis and Machine Intelligence* (pp. 1362–1376).
Gerke, M. (2014). Modern image calibration, orientation, and matching[Lecture notes]. Retrieved from https://blackboard.utwente.nl/bbcswebdav/pid-958606-dt-content-rid-2136819_2/courses/M16-EOS-103/01_SfMvsPhotogrammety.pdf
Gigli, G., & Casagli, N. (2011). Semi-automatic extraction of rock mass structural data from high resolution LIDAR point clouds. *International Journal of Rock Mechanics and Mining Sciences*, *48*(2), 187–198. http://doi.org/10.1016/j.ijrmms.2010.11.009
Gigli, G., Frodella, W., Garfagnoli, F., Morelli, S., Mugnai, F., Menna, F., & Casagli, N. (2014). 3-D geomechanical rock mass characterization for the evaluation of rockslide susceptibility scenarios. *Landslides*, *11*(1), 131–140. http://doi.org/10.1007/s10346-013-0424-2
Gigli, G., Morelli, S., Fornera, S., & Casagli, N. (2014). Terrestrial laser scanner and geomechanical surveys for the rapid evaluation of rock fall susceptibility scenarios. *Landslides*, *11*(1), 1–14. http://doi.org/10.1007/s10346-012-0374-0
Girardeau-Montaut, D. (2017). CloudCompare [GPL software]. Retrieved from http://www.cloudcompare.org/
Goodman, R. E. (1976). *Geological engineering in discontinuous rocks*. Newyork, USA: West Publishing Company.
Hack, H. R. G. K. (2016). Soil and rock mechanics [lecture notes]. Retrieved from https://blackboard.utwente.nl/webapps/blackboard/content/listContent.jsp?course_id=_20854_1&content_id=_908334_1
Hack, H. R. G. K., & Price, D. G. (1996). *evaluation of stability classification.pdf s.pdf*. Delft University of Technology. Retrieved from http://repository.tudelft.nl/islandora/object/uuid%3A09681ff2-f4e3-49bc-bd0d-25009f5ac6bf?collection=research
Hack, H. R. G. K., Price, D., & Rengers, N. (2003). A new approach to rock slope stability – a probability classification (SSPC). *Bulletin of Engineering Geology and the Environment*, *62*, 167–184. http://doi.org/10.1007/s10064-002-0155-4
Haneberg, W. C. (2008). Using close range terrestrial digital photogrammetry for 3-D rock slope modeling and discontinuity mapping in the United States. *Bulletin of Engineering Geology and the Environment*, *67*(4), 457–469. http://doi.org/10.1007/s10064-008-0157-y
Harrison, J. P. (1992). Fuzzy objective functions applied to the analysis of discontinuity orientation data. In *Rock Characterization: ISRM Symposium, Eurock '92, Chester, UK, 14?17 September 1992*. Chester, UK: Thomas Telford Publishing. http://doi.org/10.1680/rc.35621.0005
Hoek, E., & Bray, J. (1981a). *Rock Slope Engineering* (Third edit). London: Inst of Mining and Metallurgy.
Hoek, E., & Bray, J. W. (1981b). *Rock Slope Engineering Revised thrid edition*. London: Taylor & Francis.
Https://pix4d.com/. (n.d.). Pix4D - Drone Mapping Software. Retrieved February 25, 2017, from https://pix4d.com/
ISO 14689-1. (2003). Geotechinal investigation and testing. Part 1: Identification and classification of rock. Retrieved from https://www.iso.org/obp/ui/#iso:std:iso:14689:-1:ed-1:v1:en
ISRM. (1978). Suggested methods for the quantitative description of discontinuities in rock masses. *Int. J. Rock Mech. Min. Sci. Geomech. Abstr.,*. http://doi.org/10.1016/0148-9062(79)91476-1
ISRM. (1981). *Rock characterization, testing and monitoring, ISRM suggested methods*. (E. . Brown, Ed.). Oxford: Pergamon Press.
Jordan, B. R. (2015). A bird's-eye view of geology: The use of micro drones / UAVs in geologic fieldwork and education. *GSA Today*, *25*(7), 50–52. http://doi.org/10.1130/GSATG232GW.1.Figure
Kennedy, C. R. (2013). *Riegl RiScan Pro - Multi Station Adjustment Using the Plane Patch Filter*. Retrieved from https://www.youtube.com/watch?v=MDnqP5KV5eA
Kisztner, J., Jelínek, J., Daněk, T., & Růžička, J. (2016). 3D documentation of outcrop by laser scanner –

Filtration of vegetation. *Perspectives in Science*, *7*, 161–165. http://doi.org/10.1016/j.pisc.2015.11.026
Klein, E., Baud, P., Reuschlé, T., & Wong, T. (2001). Mechanical behaviour and failure mode of bentheim sandstone under triaxial compression. *Physics and Chemistry of the Earth, Part A: Solid Earth and Geodesy*, *26*(1–2), 21–25. http://doi.org/10.1016/S1464-1895(01)00017-5
Knapen, B. Van, & Slob, S. (2006). Identification and characterization of rock mass discontinuity sets using 3D laser scanning. In *IAEG, the geological society of London*. Retrieved from http://iaeg2006.geolsoc.org.uk/cd/papers/iaeg_438.pdf
Kulatilake, P. H. S. W., Wathugala, D. N., & Stephansson, O. (1993). Joint network modelling with a validation exercise in Stripa mine, Sweden. *International Journal of Rock Mechanics and Mining Sciences & Geomechanics Abstracts*, *30*(5), 503–526. http://doi.org/10.1016/0148-9062(93)92217-E
Kung, O. (2014). *Pix4D webinar 2: Ground control points [Video file]*. Retrieved from https://www.youtube.com/watch?v=Ylc_HSev3a4
Lemmens, M. (2011). *Geo-information*. Dordrecht: Springer Netherlands. http://doi.org/10.1007/978-94-007-1667-4
Liu, Q. (2013). Remote sensing technologies in rock mass characterization. In F. Tan (Ed.), *Rock Characterisation, Modelling and Engineering Design Methods* (pp. 205–210). CRC Press. http://doi.org/10.1201/b14917-36
Malmborg, P. (2002). *Correlation between diagenesis and sedimentary facies of the Bentheim Sandstone, the Schoonebeek field, The Netherlands, Msc thesis*. University of Lund.
Mancini, F., Dubbini, M., Gattelli, M., Stecchi, F., Fabbri, S., & Gabbianelli, G. (2013). Using Unmanned Aerial Vehicles (UAV) for High-Resolution Reconstruction of Topography: The Structure from Motion Approach on Coastal Environments. *Remote Sensing*, *5*(12), 6880–6898. http://doi.org/10.3390/rs5126880
Mathworks-Inc. (2017). Matlab, The language of Technical Computing [computer software]. Retrieved from http://www.mathworks.com.
McEvoy, J. F., Hall, G. P., & McDonald, P. G. (2016). Evaluation of unmanned aerial vehicle shape, flight path and camera type for waterfowl surveys: disturbance effects and species recognition. *PeerJ*, *4*, e1831. http://doi.org/10.7717/peerj.1831
Nex, F., & Remondino, F. (2014). UAV for 3D mapping applications: A review. *Applied Geomatics*, *6*(1), 1–15. http://doi.org/10.1007/s12518-013-0120-x
Pantelidis, L. (2009). Rock slope stability assessment through rock mass classification systems. *International Journal of Rock Mechanics and Mining Sciences*, *46*(2), 315–325. http://doi.org/10.1016/j.ijrmms.2008.06.003
Pix4D. (2017). Pix4Dmapper [computer software]. EPFL Innovation Park, Lausanne, Switzerland. Retrieved from https://pix4d.com/product/pix4dmapper-pro/
Priest, S. . (1993). *Discontinuity Analysis for Rock Engineering*. London: Springer Netherlands. http://doi.org/10.1007/978-94-011-1498-1
Priest, S. D. (1985). *Hemispherical Projection Methods in Rock Mechanics*. Boston: Allen and Unwin.
Priest, S. D., & Hudson, J. A. (1981). Estimation of discontinuity spacing and trace length using scanline surveys. *International Journal of Rock Mechanics and Mining Sciences & Geomechanics Abstracts*, *18*(3), 183–197. http://doi.org/10.1016/0148-9062(81)90973-6
Rabbani, T., Van der Hueuvel, F. A., & Vosselman, G. (2006). SEGMENTATION OF POINT CLOUDS USING SMOOTHNESS CONSTRAINT. In *International Archives of Photogrammetry, Remote Sensing and Spatial Information Sciences,* (pp. 248–253). Dreseden, Germany.
rapidlasso. (n.d.). Retrieved October 25, 2016, from https://rapidlasso.com/
Riegl. (n.d.). Retrieved October 12, 2016, from http://www.riegl.com/nc/products/terrestrial-scanning/produktdetail/product/scanner/33/
Riquelme, A. J., Abellán, A., & Tomás, R. (2015). Discontinuity spacing analysis in rock masses using 3D point clouds. *Engineering Geology*, *195*, 185–195. http://doi.org/10.1016/j.enggeo.2015.06.009
Salvini, R., Riccucci, S., Gulli, D., Giovannini, R., Vanneschi, C., & Francioni, M. (2015). Geological Application of UAV Photogrammetry and Terrestrial Laser Scanning in Marble Quarrying (Apuan Alps, Italy). In *Engineering Geology for Society and Territory - Volume 5* (pp. 979–983). Cham: Springer International Publishing. http://doi.org/10.1007/978-3-319-09048-1_188
Slob, S., & Hack, H. R. G. K. (2004). 3D Terrestrial Laser Scanning as a New Field Measurement and Monitoring Technique (pp. 179–189). http://doi.org/10.1007/978-3-540-39918-6_22
Slob, S., Hack, H. R. G. K., Feng, Q., Roshoff, K., & Turner, A. K. (2007). Fracture mapping using 3D laser scanning techniques. In O. & G. Ribeiro e Sousa (Ed.), *11th Congress of the International Society for*

Rock Mechanics (p. 299–302.). London: 2007 Taylor & Francis Group, London.
Slob, S., Knapen, B. Van, Hack, H. R. G. K., Turner, K., & Kemeny, J. (2005). Method for Automated Discontinuity Analysis of Rock Slopes with Three-Dimensional Laser Scanning. *Transportation Research Record: Journal of the Transportation Research Board*, *1913*, 187–194. http://doi.org/10.3141/1913-18
Slob, S., Turner, A. k., Bruining, J., & Hack, H. R. G. K. (2010). *Automated rock mass characterisation using 3-D terrestrial laser scanning*. University of Twente, Faculty of Geo-Information and Earth Observation (ITC). Retrieved from http://www.narcis.nl/publication/RecordID/oai:tudelft.nl:uuid:c1481b1d-9b33-42e4-885a-53a6677843f6
Spreafico, M. C. (2015). Terrestrial Remote Sensing techniques to complement conventional geomechanical surveys for the assessment of landslide hazard: The San Leo case study (Italy). *European Journal of Remote Sensing*, 639. http://doi.org/10.5721/EuJRS20154835
Sturzenegger, M., & Stead, D. (2009). Close-range terrestrial digital photogrammetry and terrestrial laser scanning for discontinuity characterization on rock cuts. *Engineering Geology*, *106*(3–4), 163–182. http://doi.org/10.1016/j.enggeo.2009.03.004
Tannant, D. (2015). Review of Photogrammetry-Based Techniques for Characterization and Hazard Assessment of Rock Faces. *International Journal of Geohazards and Environment*, *1*, 76–87. http://doi.org/10.15273/ijge.2015.02.009
Terzaghi, R. D. (1965). Sources of Error in Joint Surveys. *Géotechnique*, *15*(3), 287–304. http://doi.org/10.1680/geot.1965.15.3.287
Traska, M. (2014). *Water transport properties in building materials: traditional methods versus CT - based pore , MSc thesis network analysis*. University of Gent. Retrieved from http://lib.ugent.be/fulltxt/RUG01/002/163/661/RUG01-002163661_2014_0001_AC.pdf
Turner, K., Kemeny, J., Slob, S., & Hack, R. G. K. (2006). evaluation, and management of unstable rock slopes by 3-D laser scanning. In *IAEG, the geological society of London*.
Vasuki, Y., Holden, E.-J., Kovesi, P., & Micklethwaite, S. (2014). Semi-automatic mapping of geological Structures using UAV-based photogrammetric data: An image analysis approach. *Computers & Geosciences*, *69*, 22–32. http://doi.org/10.1016/j.cageo.2014.04.012
Vosselman, G., Gorte, B. G. H., Sithole, G., & Rabbani, T. (2004). RECOGNISING STRUCTURE IN LASER SCANNER POINT CLOUDS. *International Archives of Photogrammetry, Remote Sensing and Spatial Information Sciences, 46*, *part 8*, 33–38.
Vosselman, G., & Mass, H.-G. (2010). *Airborne and terrestrial laser scanning*. Dunbeath, Scotland: Whittles Publishing.
Watts, A. C., Ambrosia, V. G., & Hinkley, E. A. (2012). Unmanned Aircraft Systems in Remote Sensing and Scientific Research: Classification and Considerations of Use. *Remote Sensing*, *4*(12), 1671–1692. http://doi.org/10.3390/rs4061671
Westoby, M. J., Brasington, J., Glasser, N. F., Hambrey, M. J., & Reynolds, J. M. (2012). "Structure-from-Motion" photogrammetry: A low-cost, effective tool for geoscience applications. *Geomorphology*, *179*, 300–314. http://doi.org/10.1016/j.geomorph.2012.08.021
Windsor, C. R., & Robertson, W. V. (1994). Rock Reinforcement Practice. *Rock Mass Formulation*, *1*.
Wong, L. (2013). Determination of normal joint spacing from apparent joint spacing measurements. In *Global View of Engineering Geology and the Environment* (pp. 615–622). Beijing,China: CRC Press. http://doi.org/10.1201/b15794-99
Wonham, J. P., Johnson, H. D., Mutterlose, J., Stadtler, A., & Ruffell, A. H. (1997). Characterization of a shallow marine sandstone reservoir in a syn-rift setting: the Bentheim Sandstone Formation (Valanginian) of the Rühlermoor field, Lower Saxony Basin, NW Germany. In *GCSEPM foundation 18th annual research conference shallow marine and nonmarine reservoirs* (pp. 427–448).

7. APPENDICES

Appendix A:

Table 7-1: Rock mass weathering characterization and description grades. The super fix 'a' denotes classification and weighting according to Hack, et al. (2003), 'b' denotes classification based on BS 5930 (1981); 'c' denotes ISO 14689-1 (2003).

Grade[a,b]	Grade[c]	Term	Description[b]	WE[a]
I	0	Fresh	No visible sign of rock material weathering; perhaps slight discoloration on major discontinuity surfaces	1.0
II	1	Slightly weathered	Discoloration indicates weathering of rock material and discontinuity surfaces	0.95
III	2	Moderately weathered	Less than half of the rock material is decomposed or disintegrated	0.90
IV	3	Highly weathered	More than half of the rock is present either as a discontinuous framework or as core stones	0.62
V	4	Completely weathered	All rock material is decomposed and/or disintegrated to soil. The original mass structure is still largely intact.	0.35
VI	5	Residual soil	All rock material is converted to soil. The mass structure and material fabric are destroyed. There is a large change in volume, but the soil has not been significantly transported	-

Table 7-2: determination of intact rock strength in the field as outlined in the SSPC format, Hack, et al., (2003) following BS 5930:1999.

IRS (Mpa)	Field identification	Term
<1.25	Gravel size lumps can be crushed between finger and thumb	Very weak
1.25 to 5	Gravel size lumps can be broken half by heavy hand pressure or thin slabs break easily in hand	Weak
5 to 12.5	Only thin slabs, corners or edges can be broken off with heavy hand pressure	Moderately weak
12.5 to 50	When held in hand, lumps can be broken by light hammer blow	Moderately strong
50 to 100	When resting on a solid surface, lumps can be broken by heavy hammer blows	Strong
100 to 200	Lumps only chipped by heavy hammer blows	Very strong
>200	Rocks ring on hammer blows. Sparks fly.	Extremely strong

Appendix B

Representation of discontinuity orientation

Discontinuity orientations and sets are more accurately recognized and subsequently represented in a graphical method known as hemispherical projection. Hemispherical projection, or a stereographic projection, is a technique of graphically presenting and analyzing three-dimensional orientation of planar and linear features in two dimensions using a reference sphere (Priest, 1985). In a stereographic system, the orientation and inclination of discontinuities are either represented as great circles or poles (of discontinuity planes) (figure 7-1c). Great circles define the intersection of a plane and a reference sphere, whereas poles define the normal vector to that plane. In other words, the intersection of the normal vector and the reference sphere can be projected as the pole to the plane. Poles are advantageous and intuitive for dealing with large volume of discontinuity data. Poles to discontinuity planes that show more or less similar orientation are plotted as distinct sets or clusters on the stereograph, although it is difficult to accurately find the boundary between clusters when clustering of poles becomes fuzzy.

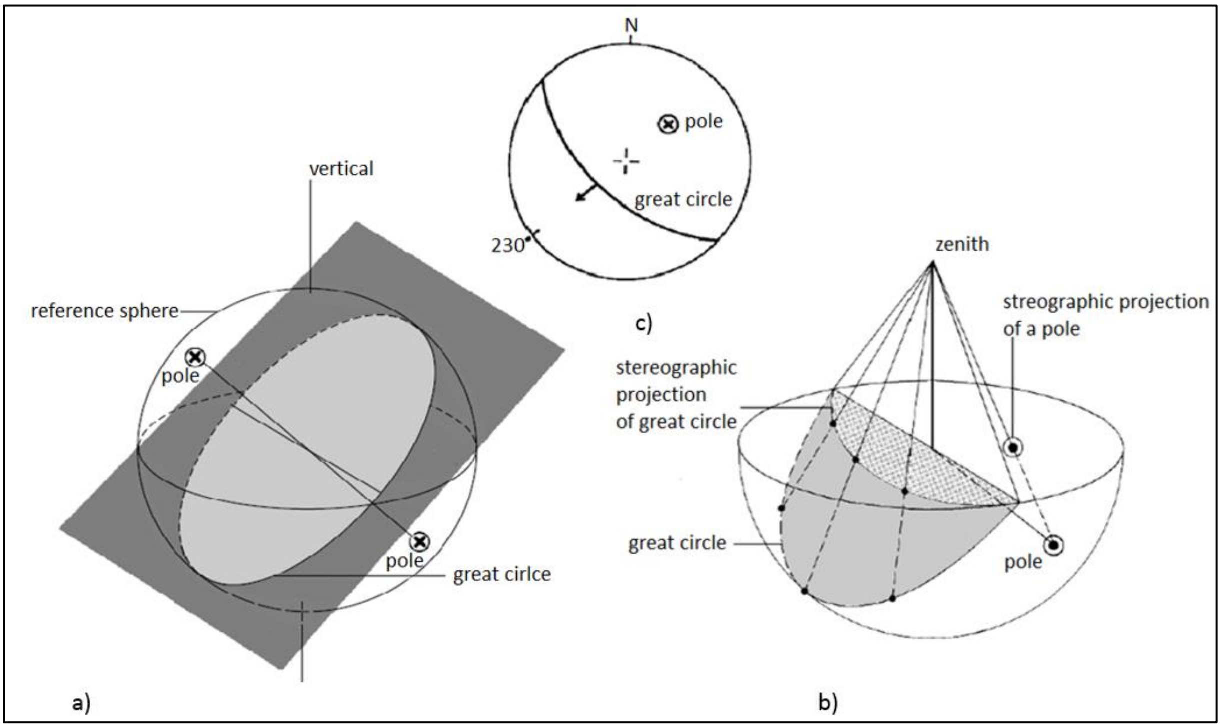

Figure 7-1: graphical or stereographic projection a) The great circle and its poles; b) lower stereographic projection of a great circle and its pole; c) great circle and pole of the plane 2300/500 after Brady & Brown (2006)

The great circle and the pole that represent discontinuity plane are found on both the upper and lower parts of the reference sphere (figure 4-1a). However, only one hemisphere is us used for plotting and manipulating structural data (Brady & Brown, 2006). In most engineering geological applications, the lower hemisphere projections are often used.

The two most common types of spherical projections are equal-area (also known as Lambert or Schmidt net) and equal angel projections (also referred to as Wulff net). Both types of projections provide the same mean plane calculation result for each set or cluster. Equal area projection preserves area from the center of the stereonet to the perimeter (figure 7-1b). It is more suited to determine the extent of sets and their relative importance. On the other hand, the equal angle projection preserves angular relationships and shapes. It is more suited to use when performing kinematic analysis.

Appendix C

Coordinate Systems

Image Coordinate System	WGS84 (egm96)
Ground Control Point (GCP) Coordinate System	Amersfoort / RD New
Output Coordinate System	Amersfoort / RD New

Processing Options

Detected Template	**3D Model**
Keypoints Image Scale	Full, Image Scale: 1
Advanced: Matching Image Pairs	Free Flight or Terrestrial
Advanced: Matching Strategy	Use Geometrically Verified Matching: no
Advanced: Keypoint Extraction	Targeted Number of Keypoints: Automatic
Advanced: Calibration	Calibration Method: Standard Internal Parameters Optimization: All External Parameters Optimization: All Rematch: Auto, yes Bundle Adjustment: Classic

Point Cloud Densification details

Processing Options

Image Scale	multiscale, 1/2 (Half image size, Default)
Point Density	Optimal
Minimum Number of Matches	3
3D Textured Mesh Generation	yes
3D Textured Mesh Settings:	Resolution: Medium Resolution (default) Color Balancing: no
Advanced: 3D Textured Mesh Settings	Sample Density Divider: 1
Advanced: Matching Window Size	7x7 pixels
Advanced: Image Groups	group1
Advanced: Use Processing Area	yes
Advanced: Use Annotations	yes
Advanced: Limit Camera Depth Automatically	yes

Figure 7-2: Initial Processing and Point cloud densification

Ground Control Points

GCP Name	Accuracy XY/Z [m]	Error X [m]	Error Y [m]	Error Z [m]	Projection Error [pixel]	Verified/Marked
GCP 3 (3D)	0.020/ 0.020	-0.089	0.043	0.737	0.868	87 / 87
GCP 4 (3D)	0.020/ 0.020	0.364	-0.243	-1.018	1.309	59 / 59
GCP 5 (3D)	0.020/ 0.020	-0.288	-0.403	1.221	1.560	35 / 36
GCP 12 (3D)	0.020/ 0.020	0.026	0.077	-0.556	1.218	66 / 66
GCP 13 (3D)	0.020/ 0.020	-0.016	0.519	-0.385	0.537	12 / 12
Mean [m]		-0.000497	-0.001228	-0.000149		
Sigma [m]		0.211770	0.315854	0.839907		
RMS Error [m]		0.211771	0.315856	0.839907		

0 out of 3 check points have been labeled as inaccurate.

Check Point Name	Accuracy XY/Z [m]	Error X [m]	Error Y [m]	Error Z [m]	Projection Error [pixel]	Verified/Marked
GCP 2	0.0200/0.0200	0.1213	-0.2660	-0.9106	1.1662	80 / 81
GCP 6	0.0200/0.0200	-0.9557	7.1231	4.2349	1.0069	171 / 172
GCP 10	0.0200/0.0200	-0.7641	-0.7261	0.0267	1.2838	18 / 19
Mean [m]		-0.532835	2.043671	1.116983		
Sigma [m]		0.469080	3.596637	2.237631		
RMS Error [m]		0.709893	4.136713	2.500929		

Figure 7-3: Quality report of ground control points

Appendix D
Processing software used

The following instruments and software were used at different stages of the research for purposes ranging from pre-processing to data analysis and visualization (table 7-3).

Table 7-3: Instruments, and processing and analysis software used and their purpose in the research. The asterisk mark denotes open software and can be downloaded free.

Instruments	purpose
Field Geological equipment (compass, hammer, measuring tape, etc.)	Measuring discontinuity data manually
DJI Phantom 4 quadra-copter UAV system	RGB image acquisition
RIEGL VZ-400 Terrestrial Laser Scanner	TLS point cloud generation
Leica RTK differential GPS	Measuring ground control points (GCP)
Software	
ArcGIS, version 10.3	Production of location Map
Pix4DMapperPro (Pix4D, 2017)	UAV image processing and point cloud generation
Riegl RiSCAN PRO (Riegl, n.d.)	Pre-processing of TLS point clouds
Point Cloud Mapper (PCM) (Vosselman et al., 2004)*	Point cloud segmentation
CloudCompare (Girardeau-Montaut, 2017)*	Point cloud filtering and subsampling
Matlab R2017a (Mathworks Inc, 2017)	Deriving, analyzing and visualizing discontinuity data
OSXStreonet (Cardozo & Allmendinger, 2013)	Stereonet plotting
Microsoft Excel 2013	Statistical analysis
Microsoft Word 2013	Thesis writing

Appendix E

Direct segmentation results of TLS point clouds into distinct discontinuity planes carried out via Hough transform and Least squares method in Point Cloud Mapper (PCM) software.

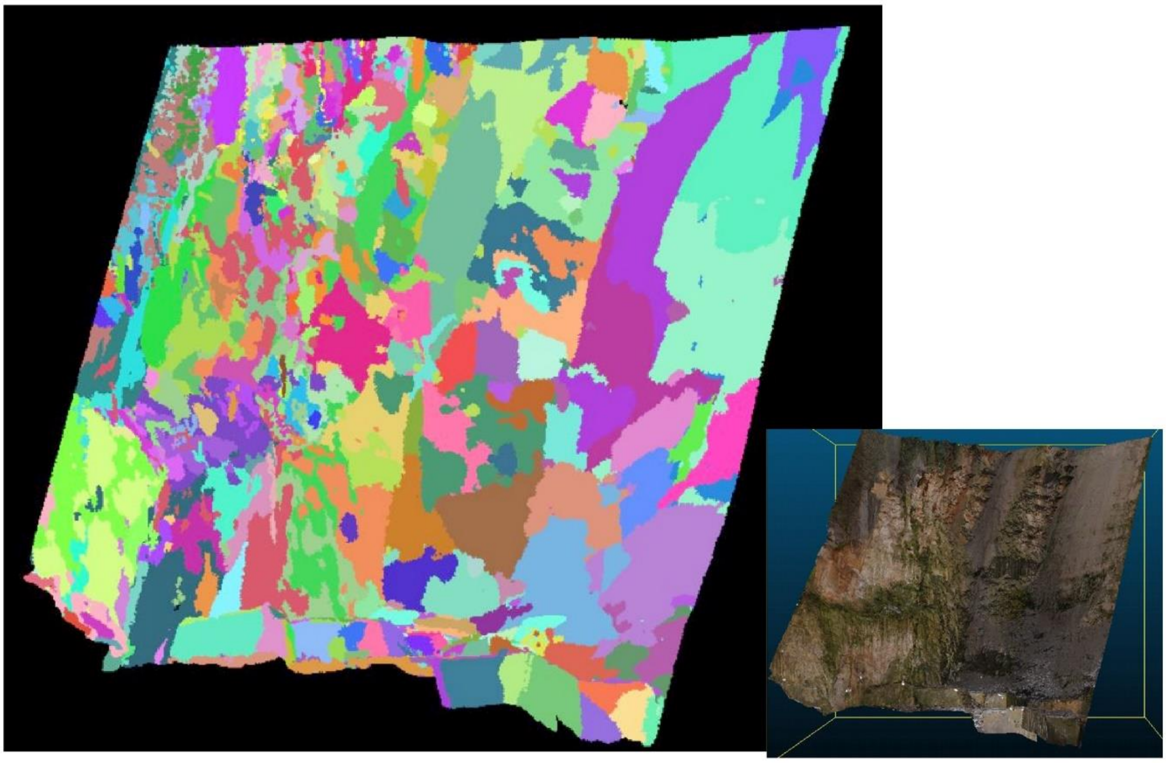

Table 7-4: Direct segmentation results of UAV based point clouds into distinct discontinuity planes carried out via Hough transform and Least squares method in Point Cloud Mapper (PCM) software. The inset photo illustrates the input point cloud for the segment.